

Installation and Characterization of a pulsed-neutron
generator at the University of Sheffield Neutron
Facility for use in a Feasibility Study into Pulsed
Fast-Thermal Neutron Activation Analysis for Cargo
Screening

Andrew Cole

31/08/2014

Contents

1	Background to the Study	10
1.1	Introduction	10
1.2	System Requirements for Bulk Cargo Screening	11
1.2.1	Explosives	12
1.3	The Ideal Scanner	14
1.4	X-ray Screening Methods	14
2	General Theory	15
2.1	Neutron Interactions With Matter	15
2.1.1	Neutron Energy Regimes	17
2.2	The Cross-Section	17
2.2.1	The Microscopic Cross-Section	17
2.2.2	The Macroscopic Cross-Section	19
2.2.3	Mean Free Path	21
2.3	The Reaction Q-Value	21
2.3.1	Elastic scattering	26
2.3.2	Inelastic Scattering	27
2.3.3	The Radiative Capture (n, γ) Reaction	28
2.3.4	Transmutation, Neutral Reactions & Fission	30
2.4	Gamma-Ray Interactions With Matter	30
2.4.1	Photoelectric absorption	31
2.4.2	Compton Scattering	32
2.4.3	Pair Production	34
2.4.4	Detector Response	35
3	Neutron-Based Interrogation Methods	37
3.1	Neutron Sources	38
3.2	Interrogation Techniques	38
3.2.1	TNA: Thermal Neutron Analysis	38
3.2.2	FNA: Fast Neutron Analysis	39
3.2.3	PFNA: Pulsed Fast Neutron Analysis	40
3.2.4	PFTNAA: Pulsed Fast-Thermal Neutron Activation Analysis	41
4	The University of Sheffield Pulsed-Neutron Facility	43
4.1	Introduction and Background	43
4.2	The NSD-Gradel Portable Pulsed Neutron Generator (NG)	44

4.3	Neutron Production from the NG	44
4.3.1	The Deuterium - Tritium (DT) Reaction	45
4.3.2	The Deuterium - Deuterium (DD) Reaction	45
4.3.3	Neutron generator operation	46
4.3.4	Output Monitoring During Operation	48
4.3.5	Experimental Method	49
5	Proton Recoil Detectors for Fast Neutrons	51
5.1	Introduction	51
5.2	The Hornyak button	52
5.3	The Theory of Hornyak Button Design	53
5.3.1	Recoil Proton Energy Loss	53
5.3.2	Mass ratio	55
5.3.3	Detector Materials	56
5.3.4	Calculating the Range, R	57
5.3.5	Detector Configuration and Signal Processing	64
5.4	Longer Exposure to Neutrons	68
5.4.1	^{252}Cf	68
5.4.2	AmBe	70
5.5	Detector Efficiency	71
5.6	Conclusions	72
6	Shielding and Collimation of the Neutron Source	73
6.1	Shielding Requirements	73
6.2	Shielding Geometry and Materials	73
6.3	Tests of Shielding Materials	75
6.3.1	Conclusion	81
6.4	Determining a suitable aperture width	81
6.4.1	Experimental setup	82
6.5	Collimator Construction	84
6.5.1	Collimator Measurement	85
6.6	Conclusion	87
7	Estimating the Neutron Yield Using Fast Neutron Activation Analysis (FNA)	90
7.1	Introduction	90
7.2	Activation Materials	91
7.2.1	The $^{27}\text{Al}(n, p)^{27}\text{Mg}$ Reaction	92
7.2.2	The $^{63}\text{Cu}(n, 2n)^{62}\text{Cu}$ Reaction	92
7.3	The Yield Equation	94
7.3.1	Derivation of the Yield Equation	94
7.3.2	Corrections to the Yield Equation	98
7.4	Experimental Method	101
7.4.1	The Copper and Aluminium Samples	103
7.4.2	Sample Irradiation Geometry	103
7.4.3	Experimental Method: The decay curve	104

7.4.4	The Yield Template	106
7.5	Results: Aluminium Samples	106
7.6	Results: Copper Samples	108
7.7	Systematic Errors	110
7.7.1	Timing	110
7.7.2	Element-Dependent Systematic Errors	110
7.7.3	Geometry	111
7.8	Conclusions	112
8	Thermal Neutron Activation Analysis of Hydrogen and Nitrogen	114
8.1	Introduction: (n, γ) reactions on ^1H and ^{14}N	114
8.1.1	The H(n, γ)D reaction	114
8.1.2	The $^{14}\text{N}(\text{n}, \gamma)^{15}\text{N}$ reaction	115
8.2	Experimental Setup	115
8.2.1	Data acquisition	117
8.3	Calibration of the Kromek K102 USB-MCA	122
8.4	Background Contributions to the Spectra	124
8.4.1	Natural Background	124
8.4.2	Generator Induced Background	127
8.5	Identification of the 2.2 MeV Gamma from the (n, γ) Reaction on Hydrogen	128
8.6	Identification of the 10.8 MeV Gamma from the (n, γ) Reaction on Nitrogen	130
8.7	Background Reduction	134
8.7.1	Low-Energy Gamma Filter	134
8.7.2	Addition of a Cadmium Foil	137
8.8	Conclusions	140
9	Scope for Future Work at the University of Sheffield Pulsed-Neutron Facility	142
9.1	Prompt Signals - Inelastic Scattering	142
10	Conclusions	144
11	Appendix	145
11.0.1	Lateral Projection	146
11.0.2	Low-energy gamma filter	150
11.0.3	The $^{56}\text{Fe}(\text{n}, \text{p})^{56}\text{Mn}$ Reaction	150
11.0.4	The $^{115}\text{In}(\text{n}, \text{n}\gamma)^{115\text{m}}\text{In}$ Reaction	150

List of Figures

1.1	<i>CHON ratio of stuff [1]</i>	13
2.1	<i>Neutron reaction channels. The X represents any charged particle emission and Y being an integer number of emitted neutrons - Taken from citerinard</i>	16
2.2	<i>Schematic diagram of a parallel beam of monoenergetic neutrons incident on a thin layer of material. Here, v_n and ρ_n are the velocity and number density of the neutrons; A, x and N are the cross-sectional area, thickness and number density of the target material.</i>	18
2.3	<i>Elastic scattering of a neutron off a nucleus at rest.</i>	26
2.4	<i>Diagram showing the inelastic scattering processes.</i>	28
2.5	<i>Diagram showing the radiative capture processes.</i>	29
2.6	<i>The photoelectric effect (diagram adapted from [28])</i>	31
2.7	<i>Diagram showing the principle of Compton scattering</i>	33
2.8	<i>Dominance in cross section for photoelectrin absorption, Compton scattering and pair production as a function of atomic number of the absorber and gamma ray energy [22]</i>	34
2.9	<i>Mass attenuation coefficients for sodium iodide [30]</i>	36
3.1	<i>Regions of signal generation after an initial burst of fast neutrons (red box).</i>	42
4.1	<i>Drawing of the facility</i>	44
4.2	<i>Principle of DT Fusion. Taken from XXXX</i>	45
4.3	<i>Principle of DD Fusion. Taken from XXXX</i>	46
4.4	<i>Fusion reaction cross-sections for neutron production. [REF]</i>	47
4.5	<i>Plot of absorbed dose against getter temperature for NG operation at 500V/30Hz/6.5μs</i>	49
5.1	<i>Principle of proton recoil in scintillator-doped plastics</i>	53
5.2	<i>Rectangular shape of hydrogen proton recoil energy distribution</i>	54
5.3	<i>Diagram showing a cube of casting resin with embedded scintillator grains</i>	56
5.4	<i>(left) TRIM output of average proton recoil range into polyester casting resin for 14 MeV incident neutrons. (right) ionization as a function of depth.</i>	58
5.5	<i>Plot showing the proton recoil range into our polyester casting resin when subjected to incident neutrons between 1 MeV and 14 MeV. The fit is a polynomial used to calculate the range R in this energy regime, to be used in equation 5.7.</i>	59
5.6	<i>Diagram</i>	60

5.7	<i>Aluminium mould template for casting the fast neutron buttons</i>	62
5.8	<i>Cast and polished Hornyak style buttons of varying thicknesses.</i>	62
5.9	<i>IBH NanoLED [18] system with a Hornyak style button coupled to a 5 inch diameter EMI 9791 KB photomultiplier tube</i>	63
5.10	<i>Pulse height as a function of button thickness for several detectors. The half-value thickness is highlighted.</i>	64
5.11	<i>Signal processing chain used for pulse shape discrimination</i>	65
5.12	<i>Pulse shape comparison between random photomultiplier tube noise and a recoil proton ionizing the ZnS(Ag) scintillator. Note, the neutron induced pulse also shows a superimposed noise pulse approximately 2 μs into the event.</i>	66
5.13	<i>Count comparison between Hornyak button exposure to gamma and neutron source relative to background.</i>	67
5.14	<i>Pulse height spectrum from ^{252}Cf neutrons on a 5.08 cm diameter by 1 cm thick Hornyak button at the University of Sheffield (main). Also, the ^{252}Cf fission spectrum produced by AEA Technology at Harwell, Oxfordshire, UK (inset) [16]</i>	69
5.15	<i>Comparison between pulse height spectra from the University of Sheffield americium-beryllium neutron source (main) and the ISO recommended spectrum (inset)</i>	70
6.1	<i>Cut-away drawing of the neutron collimator showing the generator in situ</i>	74
6.2	<i>Diagram showing the experimental setup for determining the quality of the collimator materials.</i>	75
6.3	<i>Plot showing the effects of the generator collimator on fast neutrons. The fits to the data are described in the text.</i>	76
6.4	<i>Comparison between unshielded neutron flux and relative stopping power of shielding materials</i>	79
6.5	<i>Plot showing the effects of the generator collimator on thermal neutrons.</i>	80
6.6	<i>Experimental setup for determination of the collimator aperture width . .</i>	82
6.7	<i>Plot showing the number of counts as a function of aperture width. The detector was positioned directly above the centre of the neutron generator</i>	83
6.8	<i>Construction of the collimator support (1) & (2). Finished collimator with sample in situ (3).</i>	84
6.9	<i>Experimental setup to determine collimator effectiveness.</i>	85
6.10	<i>Plot showing the effectiveness of a vertical 5cm aperture collimator against generator fast neutrons.</i>	86
6.11	<i>Magnetite concrete block bulk shield.</i>	87
6.12	<i>Generator in situ.</i>	88
6.13	<i>Final collimator construction with sample in situ</i>	88
7.1	<i>Cross-section as a function of neutron energy for isotopes of aluminium and copper</i>	93
7.2	<i>Buildup and decay of the induced activity of a sample. Exposure to a neutron flux begins at $t = 0$, the sample is removed from the neutron flux at time t_0 and counting takes place between t_1 and t_2. [22]</i>	96
7.3	<i>Activation spectrum from Cu sample 2.</i>	99

7.4	<i>Decay scheme of ^{22}Na and ^{54}Mn</i>	101
7.5	<i>^{22}Na spectrum highlighting the 511 keV annihilation peak and other key spectral features</i>	102
7.6	<i>Schematic of the reaction chamber</i>	103
7.7	<i>Schematic of the reaction chamber</i>	104
7.8	<i>Overlay of spectra produced over time from a neutron activated copper sample</i>	105
7.9	<i>Activation spectrum acquired from aluminium sample 190713Al2</i>	106
7.10	<i>Exponential decay of activated ^{28}Al</i>	107
7.11	<i>Activation spectrum from copper sample 240714Cu1</i>	108
7.12	<i>Exponential decay of activated ^{63}Cu</i>	109
8.1	<i>Figure showing the collimated neutron generator, shielded scintillation detector and sample location.</i>	116
8.2	<i>4" × 4" Sodium-Iodide scintillation detector in situ shielded with lead</i>	117
8.3	<i>Signal processing chain for thermal neutron induced events</i>	119
8.4	<i>Elastic scattering cross section between thermal energies and 15 MeV. Taken from [REF ENDFPLOT]</i>	121
8.5	<i>Cobalt-60 spectrum acquired on the Kromek USB-MCA</i>	123
8.6	<i>Taken from [?]</i>	125
8.7	<i>Spectrum acquired over 10800 seconds to assess the natural background contribution to the spectra. The main peaks have been labelled</i>	125
8.8	<i>Data from our background spectrum over 4 MeV (red) compared to that taken by Stenberg.</i>	126
8.9	<i>Spectrum acquired over 10800 seconds with the generator running at 500V - 30 Hz - 6.5μs</i>	127
8.10	<i>Polypropylene sample</i>	129
8.11	<i>Spectra showing identical features at different magnitudes to highlight the effect of increased hydrogen content in the sample.</i>	130
8.12	<i>Comparison of polypropylene sample and urea sample spectra</i>	131
8.13	<i>Urea sample spectrum rebinned over 256 channels</i>	132
8.14	<i>Comparison of polypropylene and urea spectra rebinned over 256 channels</i>	133
8.15	<i>10.8 MeV nitrogen region of interest in the urea spectrum after polypropylene spectrum subtraction</i>	134
8.16	<i>Comparison between the generator induced background with and without the lead filter over the face of the NaI(Tl) detector</i>	135
8.17	<i>Spectra comparison of polypropylene and urea samples with lead filter introduced</i>	136
8.18	<i>Cadmium foil wrapped around the NaI(Tl) crystal. The geometry of the lead shield and copper collar is unaltered.</i>	137
8.19	<i>Comparison between the generator induced background with and without the cadmium foil over the NaI(Tl) detector</i>	138
8.20	<i>Spectra comparison of polypropylene and urea samples with cadmium foil around the detector crystal</i>	139
8.21	<i>10.8 MeV nitrogen region of interest in the urea spectrum after polypropylene spectrum subtraction</i>	140

11.1	<i>Reduction in energy of incident gamma rays and energy transfer to atomic electrons for gamma energies of 2 MeV</i>	145
11.2	<i>Diagram</i>	146
11.3	<i>IMAGE OF LN2 DEWAR NEXT TO DETECTOR OVER APERTURE</i>	147
11.4	<i>IMAGE OF the two spectra of LN2 and NO LN2</i>	148
11.5	<i>ADD CAPTION</i>	151
11.6	<i>CAPTION</i>	152
11.7	<i>CAPTION</i>	152

Foreword

Introduction to the project

Personal statement??

Acknowledgements

NaI(Tl) provided by Dr. Sean Hughes and his group at the National Physical Laboratory (NPL)



Chapter 1



Background to the Study

The purpose of this thesis was to install and characterize a portable pulsed neutron generator to create a facility at the University of Sheffield, capable of **undertaking a feasibility study into** the use of pulsed fast-thermal neutron activation analysis (PFTNAA). The primary goal was to assess the PFTNAA technique for the direct detection of explosives and other illicit substances in the presence of benign materials contained in commercial and passenger air freight.


1.1 Introduction

With the ongoing threat of terror attacks and the daily transport of illegal narcotics and contraband, there is a growing need for robust, practical, non-intrusive and efficient screening of air cargo [7]. There are a number of factors that need to be considered in the design of a screening system **relating to both the nature of the threat and the environment** in which the screening is to be undertaken. This chapter aims to address these factors by providing a brief overview of these requirements and the techniques currently employed. The main focus of the project at this early stage was the identification of explosive compounds, and explosives will be referred to as “the threat” for the remainder of this

chapter, unless ated.

Screening for explosives, drugs and contraband is a complex task. We need to know what the target is, where to look for it, and perhaps most importantly, *how* to identify it. In the context of a busy international airport this is naturally challenging. In terms of explosives, there have been several incidences of attackers attempting to detonate a device concealed on their person, for example the “Shoe Bomber”  Richard Reid in 2001 [10].  While in the illegal drugs trade and contraband smuggling, small (as opposed to bulk) shipments are regularly transported on the body of the carrier [45]. This renders several interrogation technologies unsuitable for passenger screening, and as a result passenger screening will not be discussed further here.

1.2 System Requirements for Bulk Cargo Screening

For the majority of countries, the primary method of interception for threat objects is intelligence [42]. While successful terrorist attacks attain global coverage, there have been several recent bombing attempts that have been prevented through intelligence which have gained the same level of worldwide notoriety. One such attempt was the “Cargo Planes Bomb Plot” uncovered on the 29th October 2010  which two cargo airliners bound for the United States were targeted. The first device was discovered after a scheduled stop-over of UPS flight 232 at East Midlands International Airport, UK, en-route to Detroit, Michigan, and the second on an aircraft located at the FedEx depot in Dubai International Airport en-route to Newark, New Jersey. The devices consisted of the explosive Pentaerythritol tetranitrate (PETN) loaded into the toner cartridge of a typical office printer which would have been triggered via a lead azide detonator wired to a mobile phone battery [25][24].

Before their discovery, the packages had previously travelled through several other destinations on both freight and passenger aircraft where they had not been identified by

standard security screening techniques at the **respective airport**, and were only discovered after intelligence was shared with the United States Department of Homeland Security by Saudi Arabia's Deputy Interior Minister, Prince Mohammed bin Nayef. It is widely believed that without the intervention of the Saudi interior minister the 2010 bomb plot would have been successful, despite the cargo going through security checks during transit [26].

1.2.1 Explosives

There are many non-explosive industrial chemicals such as organic peroxides and ammonium nitrate (AN) that when combined can form explosive mixtures [47]. Peroxides are widely used in both the medical and industrial sectors and are readily **available** at little cost to the consumer, as is ammonium nitrate which is most commonly used as an agricultural fertilizer. However, these are seldom used in aircraft bomb attacks due to their high vapour pressure [3]. Threats of this nature are more commonly used in ground attacks such as the **Oaklahoma** City bomb in 1999, in which ammonium nitrate was mixed with fuel oil creating a powerful industrial explosive known as ANFO [46].

Materials such as propellants and pyrotechnics are categorized as explosives, but it is primarily the “high explosives” (HE) group of materials, specifically, devices based on TNT, RDX (commonly referred to as Hexogen), PETN (Nitropenta) and HMX (Octogen), that are of interest in **aviation** security [3]. While there are many types of HE, the fine detail will not be discussed here. **However**, for more specific information on HE and other common explosive compounds see references [47] (specifically Appendix 2) and [46], where the latter also highlights **usage** trends and key historical bombing events.

All of the HE mentioned above consist of four primary elements **carbon**, hydrogen, oxygen and nitrogen (CHON). Oxygen is the key element required for the explosive reaction, and, because the most important oxygen-rich carriers are organic nitro compounds and nitrates [20][19][3], HE form a group of materials that are naturally high in oxygen and

nitrogen, at the expense of reduced concentrations of hydrogen and carbon [19][1] relative to other CHON materials. A common image used to highlight this difference is shown in figure 1.1 taken from [1]. This shows the relative abundance by number for CHON elements for several explosive, narcotic and benign materials.

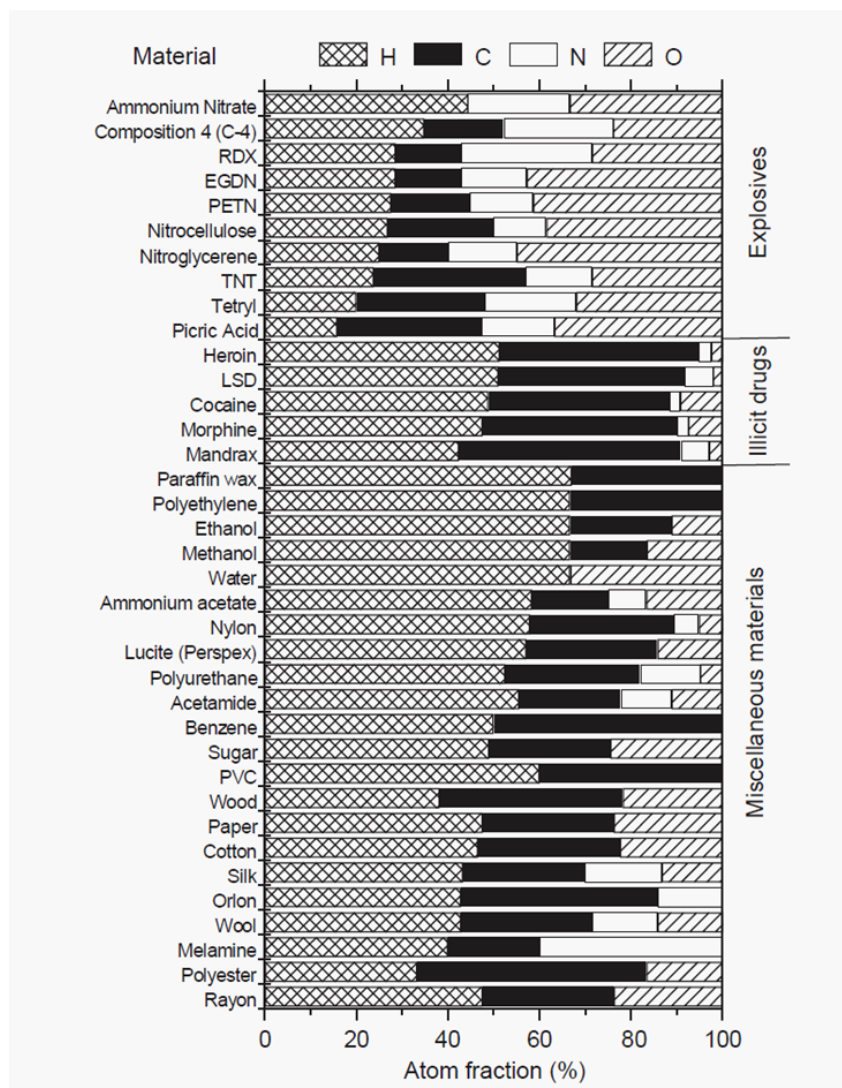


Figure 1.1: *CHON ratio of stuff [1]*

EXPAND

Link to failed 2010 bomb plot. Hard to detect...

1.3 The Ideal Scanner

requirements - airport location

1.4 X-ray Screening Methods

Brief - refer to papers

lead in —¿ The need for Nuclear

Chapter 2

General Theory

This chapter is based upon neutron and gamma ray interactions with matter. The theory relates to all aspects of this feasibility study, and while not intended to give a rigorous mathematical treatment of the theory, a basic understanding of the concepts that are important for the relevant neutron and gamma measurements are discussed.

2.1 Neutron Interactions With Matter

Neutrons are zero charge subatomic particles with a mass of approximately 939.565 MeV/ c^2 , 1.675×10^{-27} kg, or 1.008 u (atomic mass unit), slightly larger than the proton mass (1.007 u). Protons and neutrons make up the atomic nucleus and are referred to as “nucleons”. While the neutron is stable in the nucleus, a free neutron will undergo beta decay to a proton, electron, and an electron antineutrino with a half-life of approximately 15 minutes [31].

Being uncharged, the neutron is not affected by the Coulomb force when passing through a medium and will therefore only interact with the atomic nucleus via the strong force. Because the range of this force is very small (within $\approx 10^{-13}$ cm of the nucleus), this makes the neutron an extremely penetrating form of radiation [34].

There are two ways that a neutron can interact with a nucleus, both of which depend on the incident energy of the neutron, and the species of atom it encounters. These are

1. Scattering - the neutron collides with the atomic nucleus and survives, at the expense of having reduced energy and different direction of travel. The magnitude of the energy loss and the significance of the change in direction depend on the scattering angle θ , as well as the neutron energy and target nucleus.
2. Absorption - the neutron is fully absorbed by the target nucleus, after which the product nucleus decays by a number of possible decay modes.

Figure 2.1 shows how scattering and absorption reactions are broken down

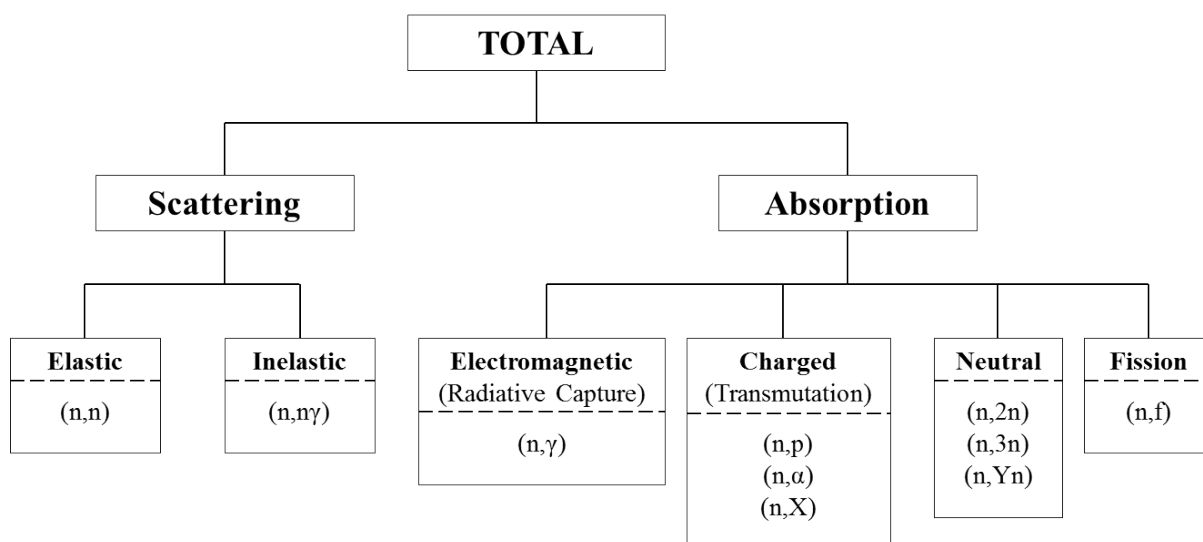


Figure 2.1: *Neutron reaction channels. The X represents any charged particle emission and Y being an integer number of emitted neutrons - Taken from ceterinard*

These interaction mechanisms, with the exception of the (n, f) reaction, will be exploited while undertaking this feasibility study and therefore a brief explanation of each will be given here. Where more detail is required, the discussion will be found in the relevant chapter.

2.1.1 Neutron Energy Regimes

Like the electromagnetic spectrum, the neutron energy spectrum covers a very large range, from a tiny fraction of an electronvolt right up to GeV energies. Therefore, neutrons are generally classified in energy bands of which there are many, depending on the particular field of neutron physics. Neutrons are commonly referred to as [34]

- thermal - $E = k_B T = 0.025$ eV
- slow - $E = 0.1$ eV to 100 keV
- fast - $E = 100$ keV = 20 MeV

Although there are many different interpretations of these boundaries, for the purpose of this thesis, neutrons energies may be referred to as the above.

2.2 The Cross-Section

2.2.1 The Microscopic Cross-Section

Consider a parallel beam of monoenergetic neutrons, incident on a thin layer of material, as sketched in figure 2.2.

Some of the incident neutrons will travel through the sample without interaction, some will disappear and fail to emerge at all, and some will emerge with reduced energy and direction [38]. The rate at which reactions occur in the material R , is directly proportional to all of the terms in figure 2.2, therefore

$$R \propto v_n \rho_n A x N. \tag{2.1}$$

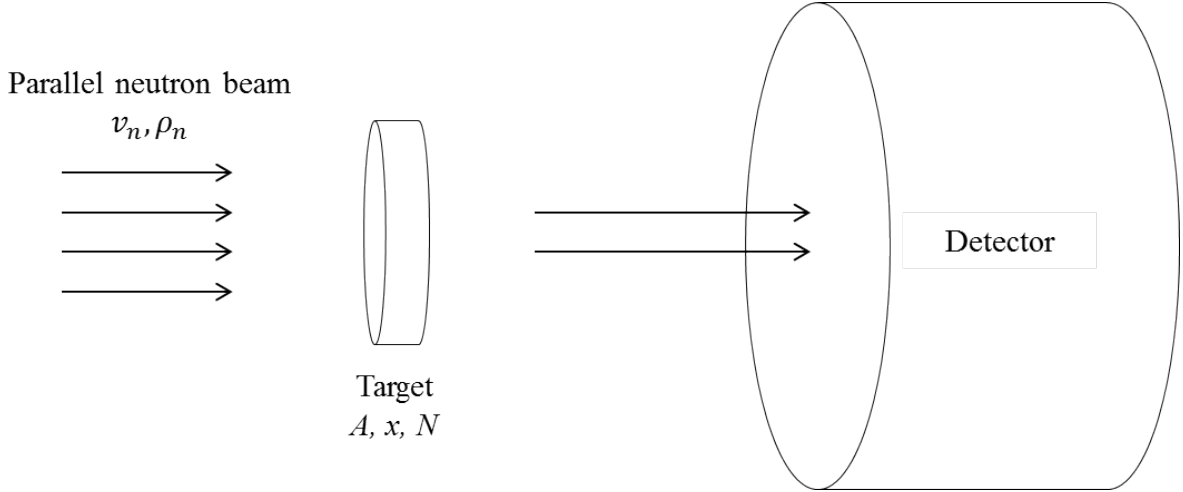


Figure 2.2: Schematic diagram of a parallel beam of monoenergetic neutrons incident on a thin layer of material. Here, v_n and ρ_n are the velocity and number density of the neutrons; A , x and N are the cross-sectional area, thickness and number density of the target material.

By defining a constant of proportionality σ , we can re-write equation 2.1 as

$$R = \sigma v_n \rho_n A x N, \quad (2.2)$$

and if we divide the reaction rate by the volume of the target V , where $V = Ax$, we can define what is known as the reaction rate density R' , which is the number of neutron reactions occurring per unit volume per second:

$$R' = \frac{R}{V} = \frac{R}{Ax} = \sigma v_n \rho_n N. \quad (2.3)$$

Rearranging equation 2.3 for the constant of proportionality σ , we get

$$\sigma = \frac{R'}{\rho_n v_n N}, \quad (2.4)$$

and if we define the neutron flux ϕ , as $\rho_n v_n$, we obtain the *microscopic cross-section*,

which has units of area.

$$\sigma = \frac{R'}{\phi N} \left[\frac{\text{reactions cm}^{-3} \text{ s}^{-1}}{\text{neutrons cm}^{-2} \text{ s}^{-1} \text{ nuclei cm}^{-3}} \right] \quad (2.5)$$

The microscopic cross-section is therefore “the reaction rate density per unit beam intensity per nucleus” [36], which can be thought of as the effective cross-sectional area that a nucleus presents to an incident neutron for a given reaction [2][38].

The cross-section is typically measured in barns, where 1 barn = 10^{-24} cm². For certain reactions such as radiative capture interactions (described in the next section), the microscopic cross section can often be orders of magnitude larger than the true geometrical cross-sectional area of the nucleus, a_n [36],

$$a_n(\text{cm}^2) = \pi r_n^2 \quad (2.6)$$

where $r_n = r_0 A^{1/3}$, A is the mass number and $r_0 \approx 1.2 \times 10^{-13}$ cm [15].

Absorption cross-sections, σ_{abs} , include all cases in which the neutron is not re-emitted by the nucleus such as (n, γ), (n, p), (n, α) and (n, fission) reactions, while scattering cross sections, $\sigma_{scatter}$, include elastic and inelastic collisions.

Depending on the species of target material and the energy of the neutron, each specific interaction mechanism will have its own cross-section, i.e. σ_{el} (elastic), σ_{in} (inelastic), σ_r (radiative capture) etc. The total cross section is therefore the sum of all the individual cross sections,

$$\sigma_{tot} = \sigma_{scatter} + \sigma_{abs} = \sigma_{el} + \sigma_{in} + \sigma_r + \dots \quad (2.7)$$

2.2.2 The Macroscopic Cross-Section

If we again consider figure 2.2, the neutron detector may observe a reduction in the initial intensity of the neutron beam, I_0 , when the material is in place.

At a distance x into the material, the intensity I_x of the neutron beam at the detector can be calculated from

$$I_x = I_0 e^{-N\sigma_{tot}x}, \quad (2.8)$$

where N is the number density for the target material and σ_{tot} is the total microscopic cross-section [34].

Equation 2.8 shows that the neutron flux is attenuated exponentially, analogous to photon attenuation [34]. The product $N\sigma_{tot}$ in equation 2.8 (referred to as Σ) is the macroscopic cross-section.

Where the *microscopic* cross-section estimates the probability of an interaction occurring for an individual nucleus, the *macroscopic* cross-section represents the probability per unit path length for a given reaction to occur [38]. Measurements are usually carried out using thick samples rather than the very thin samples described above, also, the samples are rarely monoisotopic.

The macroscopic cross-section for a compound can be calculated using

$$\Sigma = \frac{\rho_c A_v}{M} ((n_1\sigma_1) + (n_2\sigma_2) + (n_3\sigma_3) + \dots) \quad (2.9)$$

where M is the molecular weight and ρ is the density of the compound respectively. A_v is Avogadro's constant, $N_{1,2,3\dots}$ is the number density of atoms of isotope 1, 2 & 3 in the target, and finally, $\sigma_{1,2,3}$ are the microscopic cross sections for a given reaction for the corresponding isotope.

2.2.3 Mean Free Path

The determination of the mean free path λ , of a neutron in a material, is also analogous to the photon mean free path [22], such that

$$\lambda = \frac{1}{\Sigma_{tot}}. \quad (2.10)$$

By substituting 2.10 into equation 2.8 and we obtain

$$I_x = I_0 e^{-x/\lambda} \quad (2.11)$$

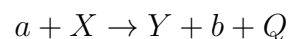
where x is the sample thickness.

In bulk material, the mean free path can range from about a centimetre for slow neutrons, while for fast neutrons, the mean free path can be several tens of centimetres [22] making neutron detection and shielding difficult (discussed in chapters 5 & 6 respectively).

While equation 2.11 is useful in the case of a parallel neutron beam, for an uncollimated neutron source a more rigorous mathematical approach is usually necessary [34]. This generally comes in the form of complex particle transport simulations such as MCNP or GEANT and will not be discussed further here.

2.3 The Reaction Q-Value

When an energetic nuclear particle impinges on a target nucleus there is a certain probability that a nuclear transformation will occur. The reaction is characterized by the species of target nucleus and the identities of the incident particle and the reaction product(s). A typical nuclear reaction is written as



or in shorthand notation [6]

$$X(a, b)Y + Q \quad (2.12)$$

where a is the incident particle, X is the target nucleus and Y and b are the product nucleus and emitted particle/photon respectively.

The Q term corresponds to the energy liberated or consumed as a result of the specific nuclear reaction, and is defined as “*the energy associated with the difference between the mass of the products and reactants*” [ref: Nargolwalla] or simply, the reaction Q-value.

If a reaction $X(a, b)Y + Q$ is to occur, then according to the law of the conservation of energy, the total energy before the reaction, E_i and the total energy after the reaction, E_f , must be equal:

$$E_i = E_f, \quad (2.13)$$

where

$$E_i = m_a c^2 + T_a + m_X c^2 + T_X \quad (2.14)$$

and

$$E_f = m_Y c^2 + T_Y + m_b c^2 + T_b \quad (2.15)$$

where $m_a c^2$ and $m_X c^2$ are the rest energies of the incident particle and the target nucleus, $m_b c^2$ and $m_Y c^2$ are the rest energies of the emitted particle and the product nucleus, T_a and T_X are the kinetic energies of the reactants, and T_b and T_Y the kinetic energies of the products. By equating E_i and E_f we get

$$m_a c^2 + T_a + m_X c^2 + T_X = m_Y c^2 + T_Y + m_b c^2 + T_b \quad (2.16)$$

Rearranging equation 2.16 gives

$$(m_a + m_X - m_Y - m_b) c^2 = T_Y + T_b - T_a - T_X \quad (2.17)$$

Both the left-hand and the right-hand side of equation 2.17 correspond to the reaction Q-value for a nuclear transformation (analogous to radioactive decay Q-values) [40].

Given the accessibility of isotopic mass tables, it is much simpler to calculate the reaction Q-value by solving the left hand side of equation 2.17 than by determining the kinetic energies of the products experimentally. Thus

$$Q = ((m_a + m_X) - (m_Y + m_b))c^2 \quad (2.18)$$

or

$$Q = \Delta mc^2. \quad (2.19)$$

Atomic masses are typically quoted in atomic mass units and Q-values in MeV; the conversion factor is

$$1\text{u} = 931 \frac{\text{MeV}}{c^2} \quad (2.20)$$

If the reaction Q-value is positive ($Q > 0$) it is termed an exothermic reaction, i.e. there will be a nett energy *release* as a result of that particular interaction which will be shared between the final products in kinetic energy. If the Q-value is negative ($Q < 0$) the reaction is endothermic, i.e. energy must be *absorbed* in order to allow the reaction to take place; in this case some initial kinetic energy is converted to nuclear mass or binding energy.

If the incident particle is charged (p, d, t, α) then it must carry sufficient kinetic energy in order for it to overcome the Coulomb barrier E_b , calculated from

$$E_b = \frac{Z_a Z_X e^2}{4\pi\epsilon_0 r}, \quad (2.21)$$

where $Z_{a,X}$ is the proton number of the projectile and target nucleus, e is the electronic charge (1.6×10^{-19} J), ϵ_0 is the permittivity of free space (8.85×10^{-12} F m⁻¹) and r is the

sum of the radii of the projectile and nucleus

$$r = 1.2 \times 10^{-15} \left((A_a)^{1/3} + (A_X)^{1/3} \right) \text{ m}$$

where A is the mass number.

Because neutrons are uncharged particles ($Z_a = 0$), $E_b = 0$, meaning that the neutron can approach the target nucleus without being affected by electrostatic repulsion.

In cases where the total mass of final state is larger than the total mass of the initial state, the reaction Q-value is negative. In order for this type of reaction to take place, the projectile must have a minimum amount of kinetic energy, known as the *threshold* energy E_t . The magnitude of this threshold energy is not simply the calculated Q-value, which would in theory make the process energetically possible: it is in fact slightly larger than Q given that a small part of the projectile energy is always transferred to the recoiling compound nucleus without contributing to the increase in the total mass of the final state, to conserve momentum [6].

The threshold energy is

$$E_t(\text{MeV}) = -Q \left(\frac{m_a + m_X}{m_X} \right) \quad (2.22)$$

where the bracketed term is the *mass ratio*.

It must also be noted that any charged product(s) in the final state must also have enough energy to overcome the potential barrier. This means that for many reactions the threshold energy is not sufficient to initiate the reaction, given that if the projectile carried *only* this threshold energy there would be zero kinetic energy for the charged products to overcome the potential barrier. It is therefore necessary to use equation 2.21 again to calculate the [relative] threshold energy required to allow the transformation.

Now that we know the Q-value it is possible to estimate the kinetic energies of the final

products contained in equation 2.17 by stating that

$$Q = T_Y + T_b \quad (2.23)$$

where the right hand side of the equation is simply the excess kinetic energy carried by the final products. Applying the law of conservation of linear momentum we can state that, in the centre of mass frame

$$m_Y v_Y = m_b v_b \quad (2.24)$$

where Y is the product nucleus and b is the emitted particle.

Using

$$v = \sqrt{\frac{2T}{m}} \quad (2.25)$$

from $T = \frac{1}{2}mv^2$, and substituting into both sides of equation 2.24, we can obtain the relationship

$$m_Y T_Y = m_b T_b. \quad (2.26)$$

If we rearrange equation 2.23 for T_Y and T_b , and substitute into 2.26 we can calculate the kinetic energy of the emitted particle as

$$T_b = \frac{Q m_Y}{m_b + m_Y} \quad (2.27)$$

and therefore, the product nucleus has kinetic energy

$$T_Y = \frac{Q m_b}{m_b + m_Y} \quad (2.28)$$

Note: It is assumed that in all cases $v \ll c$. This is a safe assumption in nuclear physics for all particles except e^\pm and neutrinos.

2.3.1 Elastic scattering

This process is generally referred to as the classic “billiard ball collision”, in which the energy lost by the incident neutron is transferred directly to the kinetic energy of a recoiling nucleus.

In an elastic scattering interaction the total *kinetic* energy is conserved, and therefore no incident neutron energy goes into the creation of reaction products, meaning that the neutron and the target nucleus are the only bodies involved in the system either before or after the scatter. Figure 2.3 shows an elastic scattering interaction.

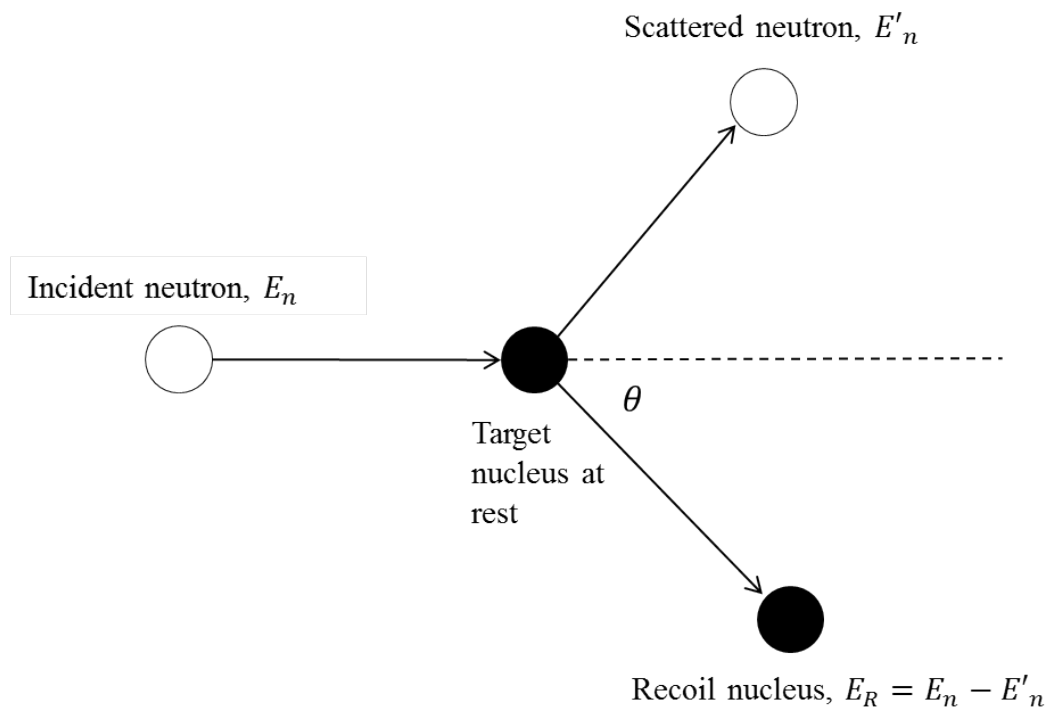


Figure 2.3: *Elastic scattering of a neutron off a nucleus at rest.*

From the conservation laws of energy and linear momentum, for non-relativistic neutron energies the amount of energy transferred to the nucleus, E_R , as a function of the scattering angle θ can be written as [43]

$$E_R = \left(\frac{4mM}{(m+M)^2} \cos^2\theta \right) E_n \quad (2.29)$$

where m is the mass of the neutron and M is the mass of the target nucleus

In neutron mass units, where $\frac{M}{m} = A$, we can re-write equation 2.29 as

$$E_R = \frac{4A}{(1+A)^2} (\cos^2 \theta) E_n, \quad (2.30)$$

where A is the mass number of the target.

Thus, the amount of energy transfer from the neutron to the nucleus is a simple function of the scattering angle θ and the mass number A of the target.

For maximum energy transfer, the scattering angle of the nucleus is zero, (i.e. a head-on collision), which simplifies equation 2.30 to

$$E_R = \frac{4A}{(1+A)^2} E_n. \quad (2.31)$$

Equation 2.31 explains why low A materials are preferred in neutron shielding and collimation applications (see chapter 6). For the hydrogen atom where $A = 1$, the fraction in equation 2.31 is also 1 and the entire incident neutron energy can be transferred to a recoiling proton in a single collision (i.e. $E_R = E_n$). In contrast for heavy elements like lead, where $A = 208$, E_R only equals $0.013E_n$ and therefore the neutron only transfers a fraction of its energy to the recoil. For a table of maximum energy transfer as a function of atomic number for selected elements, see [22].

2.3.2 Inelastic Scattering

In an inelastic scattering event the incident neutron is briefly absorbed by a nucleus of mass number A before being re-emitted with a reduced energy [43]. This energy transfer to the target nucleus creates an excited nuclear state of A which is referred to as a “compound nucleus” [40][22]. Subsequent internal re-arrangement of the target nucleons de-excites the compound nucleus through the emission of gamma radiation [43]. The

species of the target is therefore unaltered by an inelastic scattering event. Figure 2.4 shows the process.

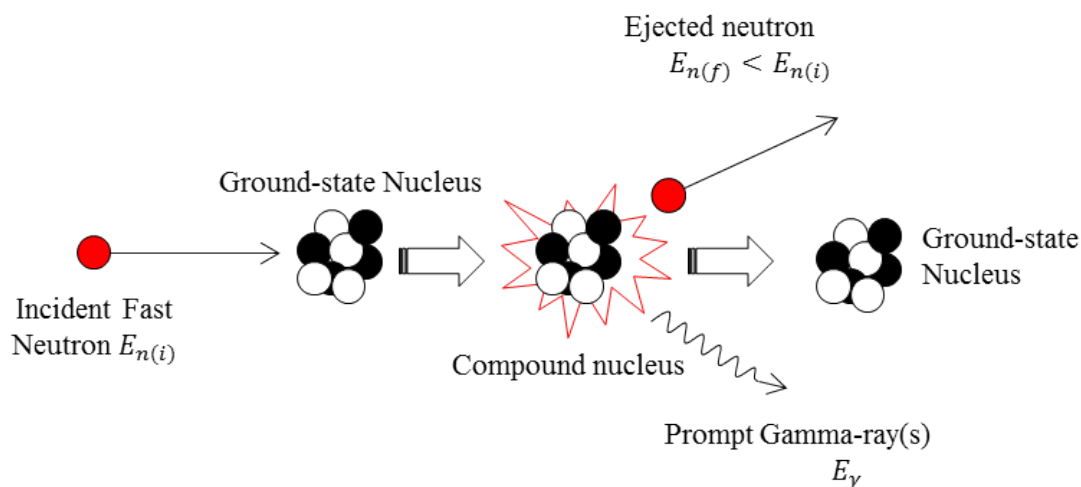


Figure 2.4: *Diagram showing the inelastic scattering processes.*

Inelastic scattering is a threshold reaction, as the incident neutron energy must be high enough to place the nucleus into an excited state. For neutrons of energy lower than the first excited state, inelastic scattering becomes impossible and only elastic collisions can take place. This is always the case for hydrogen, which does not have any excited nuclear states as it only has a single nucleon [38].

Because there is some energy transfer between the neutron and the nucleus, the kinetic energy of the final state is lower than the kinetic energy of the incident neutron, and it is this difference in energy which dictates the energy of the outgoing gamma ray(s) [40]. This makes predicting an average energy loss difficult as it depends on the number of energy levels for a particular nuclear species, which can vary greatly by element [38].

2.3.3 The Radiative Capture (n, γ) Reaction

Figure 2.5 shows a diagram of this process. In this reaction a thermal neutron of energy kT (0.025 eV at 293 K) is captured by a nucleus of mass number A and proton number

Z , forming a highly excited compound nuclear state of $(A + 1, Z)$.

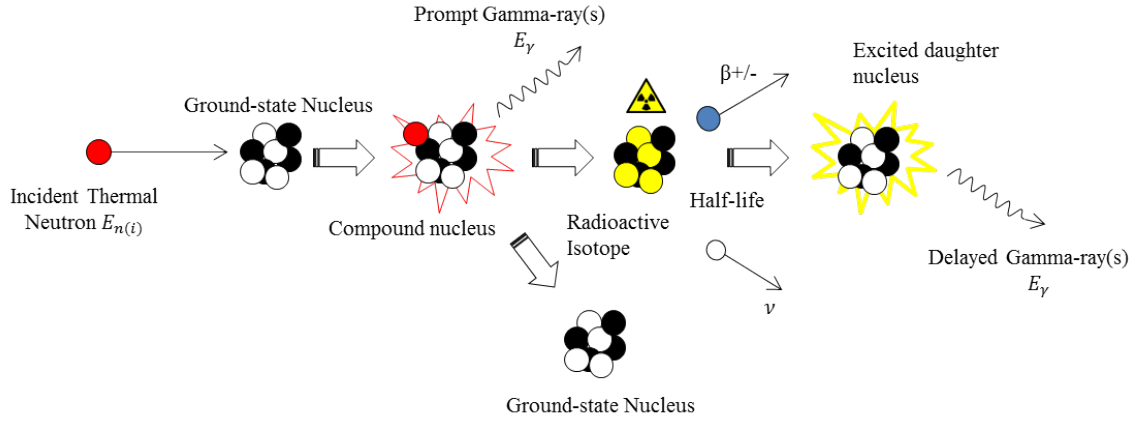


Figure 2.5: *Diagram showing the radiative capture processes.*

The magnitude of the excitation energy is characterized by the sum of the kinetic energy of the incident neutron plus the neutron separation energy, S_n , which can be calculated using

$$S_n = [(m(A - 1, Z) + m_n) - m(A, Z)] c^2 \quad (2.32)$$

where $m(A - 1, Z)$ is the mass of the target nucleus, m_n is the neutron mass and $m(A, Z)$ is the mass of the product nucleus.

The excited nucleus decays to its ground state by emission of one, or several, prompt¹ gamma-ray photon(s). If the product decays directly to the ground state it will emit a single gamma ray of energy $S_n + E_n$, but in many isotopes several gamma-rays are emitted with a wide spectrum of energies as a result of de-excitation of levels populated by the primary decay.

Finally, if the nucleus $(A + 1)$ is stable, nothing further occurs, but if the product nucleus is a radioactive isotope then it will then decay further, in a timescale corresponding to the half-life of the isotope.

¹Usually in a timescale of approximately 10^{-12} seconds

2.3.4 Transmutation, Neutral Reactions & Fission

Transmutation, neutron and fission reactions are also initiated via absorption of the incident neutron. Unlike inelastic scattering where gamma rays are emitted after nuclear de-excitation, in a transmutation process the outgoing radiation is in the form of heavy charged particles such as protons, alpha particles or deuterons.

Neutron reactions result in the emission of one or more neutrons, but if only one neutron is emitted the reaction cannot be distinguished from an inelastic scattering event. In a fission reaction, the outgoing products are referred to as “fission fragments” and can be emitted as two nuclei of relatively large A , or a series of smaller nuclei.

2.4 Gamma-Ray Interactions With Matter

A photon is a quantum of light with energy

$$E = h\nu \tag{2.33}$$

where h is Planck’s constant and ν is the frequency of the light

Gamma rays have the shortest wavelength in the electromagnetic spectrum, and therefore have the largest amount of energy per photon. Like the neutron, the gamma ray carries no intrinsic charge which also makes it a highly penetrating form of radiation.

A gamma-ray interaction is classified according to the kind of target the photon encounters (electron, atomic nucleus etc.), and the type of event which takes place (i.e. absorption, scattering). A comprehensive explanation of photon interactions can be found in [17].

Although there are many possible interaction mechanisms, only three major types have a significant role in photon attenuation for radiation measurement: photoelectric absorp-

tion, Compton scattering, and pair production [22]. All three mechanisms culminate in either all or part of the gamma photon energy being converted into electron energy.

2.4.1 Photoelectric absorption

In a photoelectric interaction the incident gamma ray is completely absorbed by an atomic electron, which is subsequently ejected by the absorber atom from one of its bound shells (primarily the K-shell, provided the photon has energy greater than the K-shell binding energy [5]). Because the photon is completely absorbed, the energy transferred to the photoelectron is simply the energy of the incident gamma ray minus the binding energy of the electron in its original shell, E_b :

$$E_{e^-} = h\nu - E_b. \quad (2.34)$$

The photoelectric absorption process is sketched in figure 2.6.

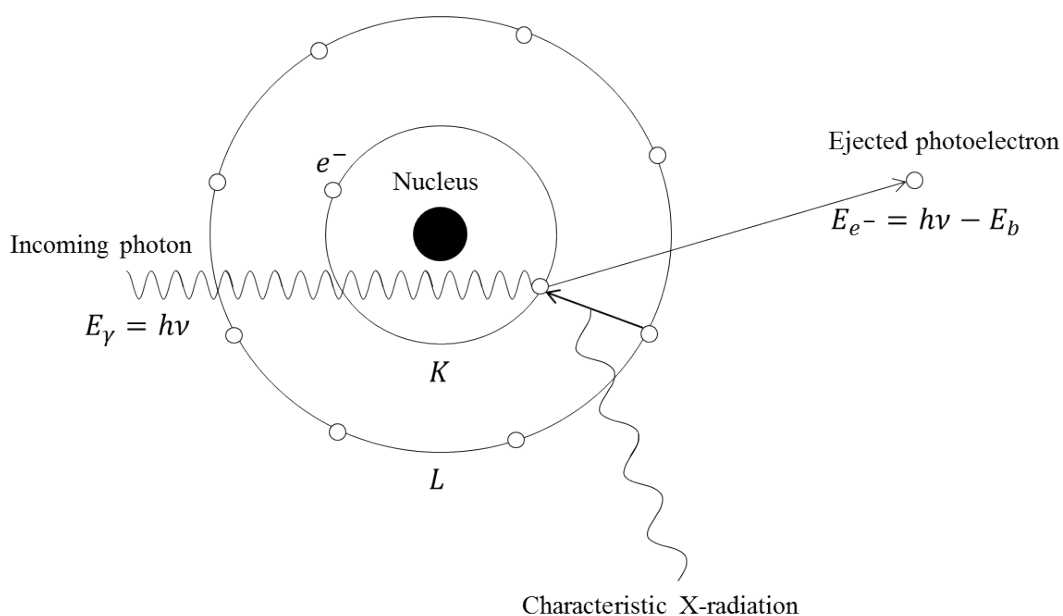


Figure 2.6: *The photoelectric effect (diagram adapted from [28])*

Once the photoelectron is ejected, the atom becomes ionized and the corresponding shell

vacancy is filled by either a free electron in the medium, or an electron from internal rearrangement of the atomic shell structure (de-excitation) [22]. This means that photoelectrons are almost always accompanied by one or more characteristic fluorescence X-rays, with energy equal to the difference of the two levels, or in some cases, Auger electrons [28][17].

The probability of photoelectric absorption occurring σ_{PE} , is calculated using a relationship between the energy of the incident photon E_γ , and the atomic number of the absorber Z , and is at its largest for relatively low energy gamma rays (below 200 keV) [41]: Although subtle variations can be found in standard reference texts [13], this relationship is generally approximated by

$$\sigma_{PE} \propto \frac{Z^n}{E_\gamma^{3.5}}, \quad (2.35)$$

where n varies between 4 and 5 over the energy region of interest [22][5].

From equation 2.35 it is clear that a material with a high atomic number is favourable for increasing the probability of photoelectric absorption, which is the primary reason behind using high Z materials for both gamma ray detectors and detector shielding [13].

2.4.2 Compton Scattering

As the incident gamma ray energy increases, the cross-section for photoelectric absorption decreases significantly, and the primary interaction mechanism for the gamma ray becomes Compton scattering. Compton scattering is the dominant interaction mechanism between gamma energies of 200 keV and several MeV [22].

In a Compton scattering interaction an incident gamma ray of energy E_γ again interacts with an atomic electron, but, unlike the photoelectric effect where the gamma ray disappears completely, in a Compton scattering interaction the gamma ray is scattered at an angle θ from its initial trajectory and continues in a new direction with reduced energy E'_γ . The difference in the gamma ray energy is transferred to the kinetic energy of the

ejected electron. This is shown in figure 2.7.

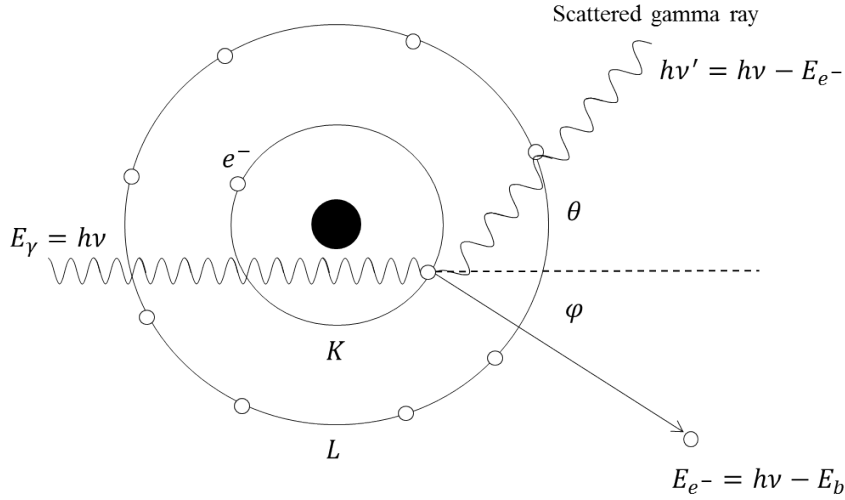


Figure 2.7: *Diagram showing the principle of Compton scattering*

The amount of energy transferred to the electron varies as a function of the scattering angle θ , and can be calculated using the relationship

$$h\nu' = \frac{h\nu}{1 + \frac{h\nu}{m_0c^2} (1 - \cos\theta)} \quad (2.36)$$

where m_0c^2 is the rest mass energy of the electron (511 keV) and $h\nu$ is the initial gamma ray energy [28].

Because all angles of scattering are possible, the energy transferred to the electron can vary from zero (when $\theta = 0$), to a large fraction of the gamma-ray energy (when $\theta = 180^\circ$). See Appendix A.

The angular distribution of the scattered gammas, $d\sigma/d\Omega$, is predicted by the Klein-Nishina formula [17], and although this will not be discussed in detail here, it is worth noting the the probability of scattering in the forward direction increases with incident gamma ray energy [22][28]. A full explanation of the Klein-Nishina formula and an image of the distribution can be found in [17].

2.4.3 Pair Production

Pair production occurs when a gamma ray interacts with the electric field surrounding the atomic nucleus, converting the gamma ray into an electron-positron pair. In order to make this conversion, the gamma ray must have at least $2m_0c^2$ (1.022 MeV) which is the sum of the rest mass energies of the electron and positron. Pair production is therefore a threshold reaction.

The cross-section for pair production increases with gamma energy and becomes the primary interaction mechanism in an absorber medium beyond around 5 MeV.

Figure 2.8 shows the relative importance of all three described interaction mechanisms as a function of the atomic number of the absorber Z and the incident energy of the gamma ray E_γ . The lines on the plot indicate the values of Z and E_γ at which the two neighbouring effects have equal probability [22].

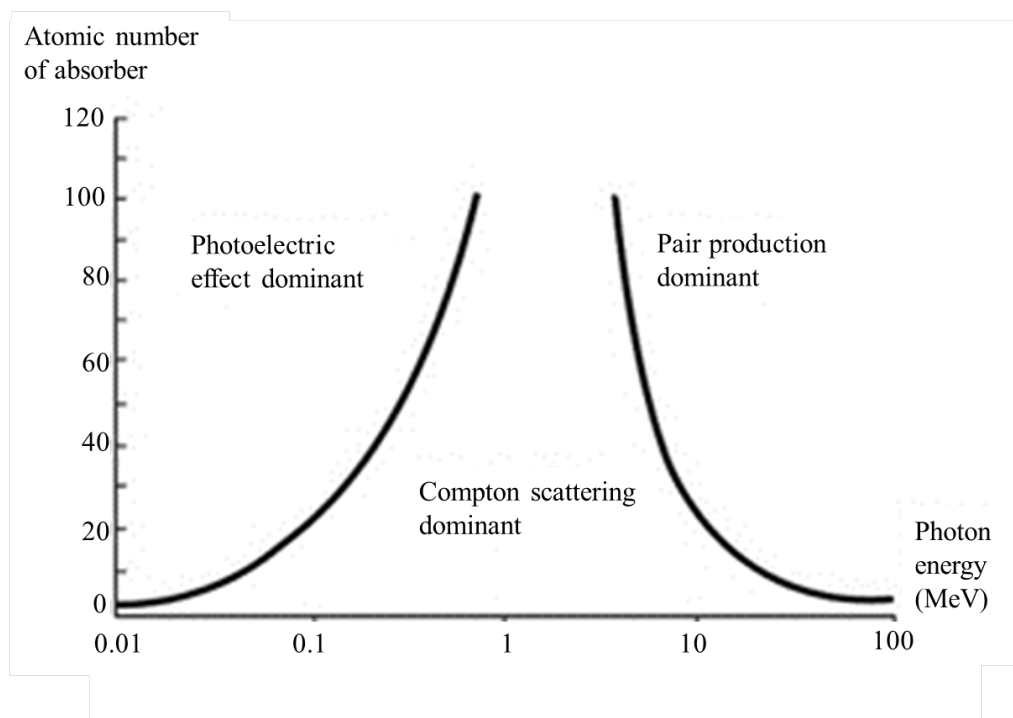


Figure 2.8: *Dominance in cross section for photoelectric absorption, Compton scattering and pair production as a function of atomic number of the absorber and gamma ray energy [22]*

2.4.4 Detector Response

Being able to absorb the full gamma ray energy is vital for accurate identification of the element from which it originated, which is why detectors are generally fabricated from high Z crystals in which even very high energy gamma rays can be fully absorbed.

For typical laboratory radioactive sources which have gamma ray energies of between a few keV and 1.5 MeV, the photon energy to electron energy conversion comes primarily via a series of Compton scattering interactions followed by photoelectric absorption, at which point the gamma ray has been fully absorbed by the detector. When higher energy gamma rays (several MeV) are the focus, achieving full energy deposition will often come from a combination of all three of the above processes, making the choice of a suitable detector material critical. In this feasibility study, a 4×4 inch thallium-doped sodium-iodide scintillation detector was chosen due to its availability, and therefore the remainder of this thesis will consider sodium-iodide only².

Figure 2.9 shows the mass attenuation coefficients for sodium iodide as a function of gamma ray energy. The shaded region representing the energy regime of interest for this feasibility study which is between around 2 MeV and 10.8 MeV (see chapter 3). At 2 MeV the probability for photoelectric absorption and pair production is negligible and therefore Compton scattering is the dominant interaction mechanism. By the time we reach 11 MeV the likelihood of pair production is comparable to that of Compton scattering.

For a detector of limited dimensions such as ours, the desirable “full-energy” peak can only be observed after multiple interactions in the detector crystal, and the probability of the gamma ray being fully absorbed without escaping the detector crystal is low at such high energies. This will be discussed further in chapter 3. The result is that a high energy gamma ray spectrum often has many other visible features other than the

²While there are other suitable detector materials on the open market which could have been purchased for this application, these will not be discussed in this chapter: instead a summary of possible alternatives can be found in “Future Work”.

Sodium-Iodide

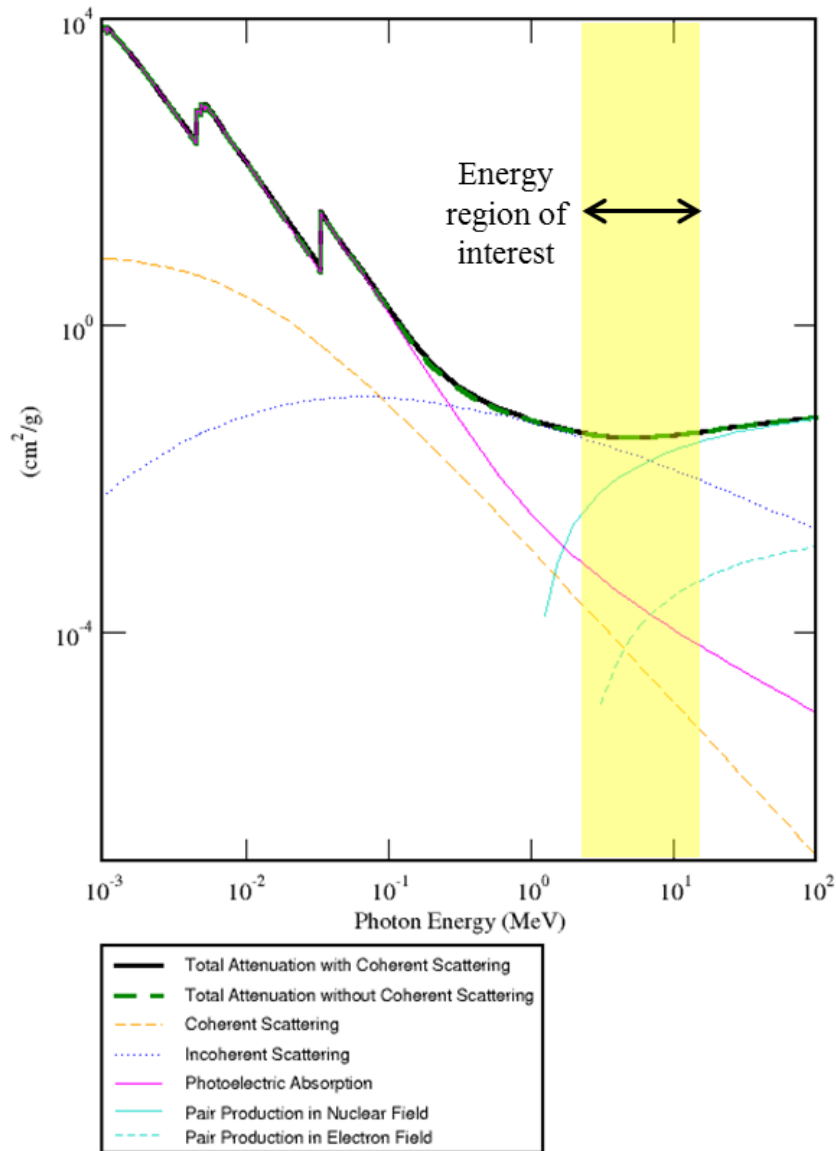


Figure 2.9: *Mass attenuation coefficients for sodium iodide [30]*

full-energy peak, some of which can aid in the identification of the incident gamma ray such as the location of the Compton edge, backscatter peak, or single & double escape peaks (as is the case in pair production), or can hinder the identification by introducing a large Compton background. Although a full explanation as to the origin of these spectral features is not necessary here, an excellent discussion can be found in chapter 2 of reference [13].

Chapter 3

Neutron-Based Interrogation

Methods

The first part of this chapter provides an overview of selected neutron based interrogation techniques with respect to cargo screening applications. The final part of the chapter focuses specifically on pulsed fast-thermal neutron activation analysis which is the purpose of the feasibility study.

As stated in chapter 1, conventional X-ray scanners are generally used for the detection of high- Z materials, such as concealed weapons, through shape recognition. In terms of an explosive device, these scanners are limited to the identification of high- Z components of the device as a whole, such as detonation wires and switches etc [3].

Nuclear interrogation methods, however, are very well suited to the detection of explosives due to their penetrability and the non-destructive nature of the interaction mechanisms. Nuclear techniques also have the advantage of specificity, making identification of explosive compounds possible at an elemental level through the identification of characteristic gamma radiation. Also, because the majority of these characteristic gamma rays are high energy (MeV), they too are highly penetrating and can escape even a large sample and reach a detector array located several metres away.

3.1 Neutron Sources

All nuclear scanning techniques rely on a source of neutrons, which can either be a radioactive material such as ^{252}Cf or americium-beryllium (AmBe), or an accelerator based device such as a neutron generator. The likelihood of a particular neutron interaction depends on the species of the target and the incident energy of the neutron, and nuclear screening systems often exploit many different interaction mechanisms. This means neutrons of several different energies may be required. Details of the interaction mechanisms can be found in chapter 2, while a more detailed summary of neutron sources can be found in chapter 4.

3.2 Interrogation Techniques

3.2.1 TNA: Thermal Neutron Analysis

TNA is carried out in two ways. Either the threat object is exposed to fast neutrons, some of which are moderated to thermal energies by the sample, or fast neutrons are moderated before reaching the sample which is then exposed to a thermal flux [14][35]. Once incident on the sample, a radiative capture interaction (n, γ) may take place resulting in the production of characteristic prompt gamma radiation [1] which can then be analysed using a suitable detector.

TNA is used for the detection of hydrogen and nitrogen in explosive compounds, specifically the 2.22 MeV gamma ray from ^1H and the 10.8 MeV gamma ray from ^{14}N respectively (see chapter 8). Because many innocuous materials are also hydrogen rich (see figure 1.1), it is primarily detection of the characteristically high energy nitrogen line that is the focus for explosives identification. TNA can also be employed in the detection of unexploded ordnance (UXO) which also contains nitrogen, as well as many metallic elements contained in shell casings that have appreciable radiative capture cross-sections

[4]. It has also been successfully implemented in the detection of chemical warfare agents [3], many of which are characteristically high in chlorine [32] that also has a relatively high (n, γ) cross section of 35.5 barns [23].

Because the signals result from radiative capture, the reliance on neutron moderation is the major drawback of this technique. Having to thermalize fast neutrons from the source¹ can significantly reduce the magnitude of the incident flux, sometimes by orders of magnitude [3]. Relying on sample moderation alone reduces the probability of a reaction even further due to the large neutron mean free path in low- Z materials associated with air cargo. This can be overcome by employing longer counting times, but in an airport-based cargo screening system this is not a viable option due to the short turnaround time of aircraft.

Given the relatively low (n, γ) cross-section of ^{14}N (10^{-2} barns [23]), a significant reduction in neutron flux can make TNA challenging even when using radioactive and accelerator based sources with a large neutron yield. Finally, the other major constituents of explosives, oxygen and carbon have unfeasibly small (n, γ) cross-sections of 1.9×10^{-4} barns and 3.5×10^{-3} barns respectively.

3.2.2 FNA: Fast Neutron Analysis

The FNA technique subjects the threat object to a collimated beam of fast neutrons, some of which undergo inelastic scattering collisions $(n, n\gamma)$ with the sample nuclei [3][1]. The de-excitation gamma rays are also prompt and are emitted isotropically from the sample. These are then detected by an array of detectors positioned around the target, where spectroscopic information is used to determine the gamma ray energy and therefore elemental identification [14].

FNA is used to detect the carbon, oxygen and nitrogen concentrations of explosives, and

¹It is much easier to moderate a radioactive source which emits (on average) lower energy neutrons and are often the preferred source for TNA [27]

the primary gamma ray energies of interest are 4.43 MeV for carbon, 6.13 MeV & 3.84 MeV for oxygen, and 1.64 MeV, 2.31 MeV & 5.1 MeV for nitrogen respectively [23]. It is not possible to detect hydrogen using FNA as inelastic scattering on hydrogen is not possible (section 2.3.2). Because inelastic scattering is a threshold reaction, the incident neutrons must have energies exceeding the above values to generate the gamma rays of interest.

While ^{252}Cf and AmBe sources do emit neutrons of high energy, the neutron emission spectra covers a wide energy range with the most probable emission energies between 1 MeV and 2 MeV (neutron emission spectra for ^{252}Cf and AmBe can be viewed in section 5.4). This makes their use as FNA sources unfeasible and it is therefore commonplace to use accelerator based neutron sources which emit 14 MeV neutrons via the deuterium-tritium (DT) fusion reaction (see chapter 4).

3.2.3 PFNA: Pulsed Fast Neutron Analysis

A derivative of FNA is the pulsed fast neutron analysis (PFNA) technique, which uses nanosecond bursts of fast neutrons to initiate the $(n, n\gamma)$ reactions in the target. Pulsing such narrow bursts has the advantage of background reduction, a common hinderance in continuous irradiation procedures, and also improvements in the imaging capability of the system through neutron time-of-flight measurements [39]. Until recently, the main limitation with PFNA has been the ability to produce relatively small, cost-effective, safe and practical neutron generators capable of generating nanosecond wide pulses [42]. However, recent developments in vacuum accelerator tubes have led to PFNA becoming potentially viable for cargo screening applications over the coming years [29].

3.2.4 PFTNAA: Pulsed Fast-Thermal Neutron Activation Analysis

As the name implies, pulsed fast-thermal neutron activation analysis is a combination of the above techniques. Combining both FNA and TNA provides a method of being able to identify the vast majority of elements which make up an explosive device, from the low- Z concentrations of the explosive compound, to the high- Z wiring, detonator components and housing.

Where PFNA uses nanosecond neutron bursts, the PFTNAA technique involves the use of a sealed tube neutron generator which produces microsecond wide neutron pulses. The specification of the generator determines the energy of the neutrons. Where some generators exclusively produce 14 MeV neutrons via the DT reaction, others generate a combination of 14 MeV and 2.3 MeV neutrons (via the deuterium-deuterium reaction).

The neutron generator is collimated, and the sample is initially irradiated by fast neutrons for the duration of the pulse width, during which inelastic scattering occurs and the characteristic carbon, oxygen and nitrogen gamma rays are detected by the NaI(Tl) detector and the spectra saved. Because the gamma emissions are prompt, these signals stop being produced very rapidly after the neutron burst.

Figure 3.1 shows the regions of signal production in PFTNAA, where the red box represents the neutron burst and the black line represents the buildup of fast neutrons through the sample.

Some of the neutrons are moderated by the sample and eventually reach thermal energies after several microseconds, at which point radiative capture interactions with hydrogen and nitrogen may take place and a second series of gamma rays are produced. This is represented by box (2) in figure 3.1. These gammas are detected by the same detector array and stored for further analysis. Finally, any radioactive isotopes produced as a result of the radiative capture interactions will then decay with the emission of gamma

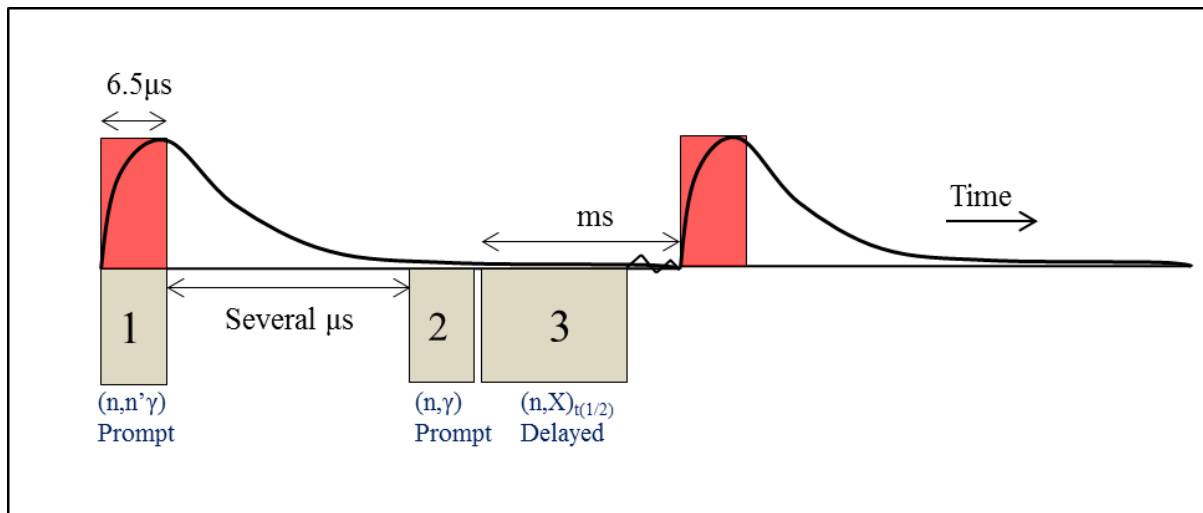


Figure 3.1: *Regions of signal generation after an initial burst of fast neutrons (red box).*

radiation, in a timescale which corresponds to the half-life of the radioisotope. Common elements detected at this stage include silicon, fluorine and phosphorus which are often found in explosive devices [1].

Provided the half-life is short compared to the duty cycle of the generator, three distinct regions of signal generation **can occur between pulses.**

The pulsed nature of this technique naturally improves the signal to noise ratio and allows a greater number of elements to be assayed during irradiation. However, the pulsing of neutrons is also the main disadvantage for PFTNAA in that having a long duty cycle dramatically reduces the magnitude of the incident flux compared to that obtainable using a continuous train of neutrons [3].

The aim of this study was to create a facility in which to assess the feasibility of PFTNAA for screening of explosives and contraband in **airborne cargo.** The following chapters present the facility in general, characterization of the pulsed neutron generator, and preliminary gamma ray measurements.

Chapter 4

The University of Sheffield Pulsed-Neutron Facility

4.1 Introduction and Background

[[[Estimating a D-T yield with a specific deuterium-tritium gas mixture in the chamber therefore becomes paramount in order for a future gas mixture refueling]]]

[THIS SECTION WILL INCLUDE THE THEORY BEHIND THE NEUTRON GENERATOR - HOW THE GENERATOR ACCELERATES THE PARTICLES?] Because of the nature of the generator gas mixture there will be a significant number of radiation emitting processes taking place during operation. These range from the production of a fast neutron emission spectrum, lower energy neutrons due to moderation by the generator assembly, bremsstrahlung, gamma rays from the neutron activation of the surrounding material and electromagnetic interference. As stated in the [REF BACKGROUND CHAPTER] the initial key reactions of interest are all threshold reactions ranging from [CHECK THIS 2 MEV TO 10.8 MEV], meaning that the incident neutron must have at least this energy to initiate the reaction from equation 2.22. The following chapter describes the origin of these (features??)

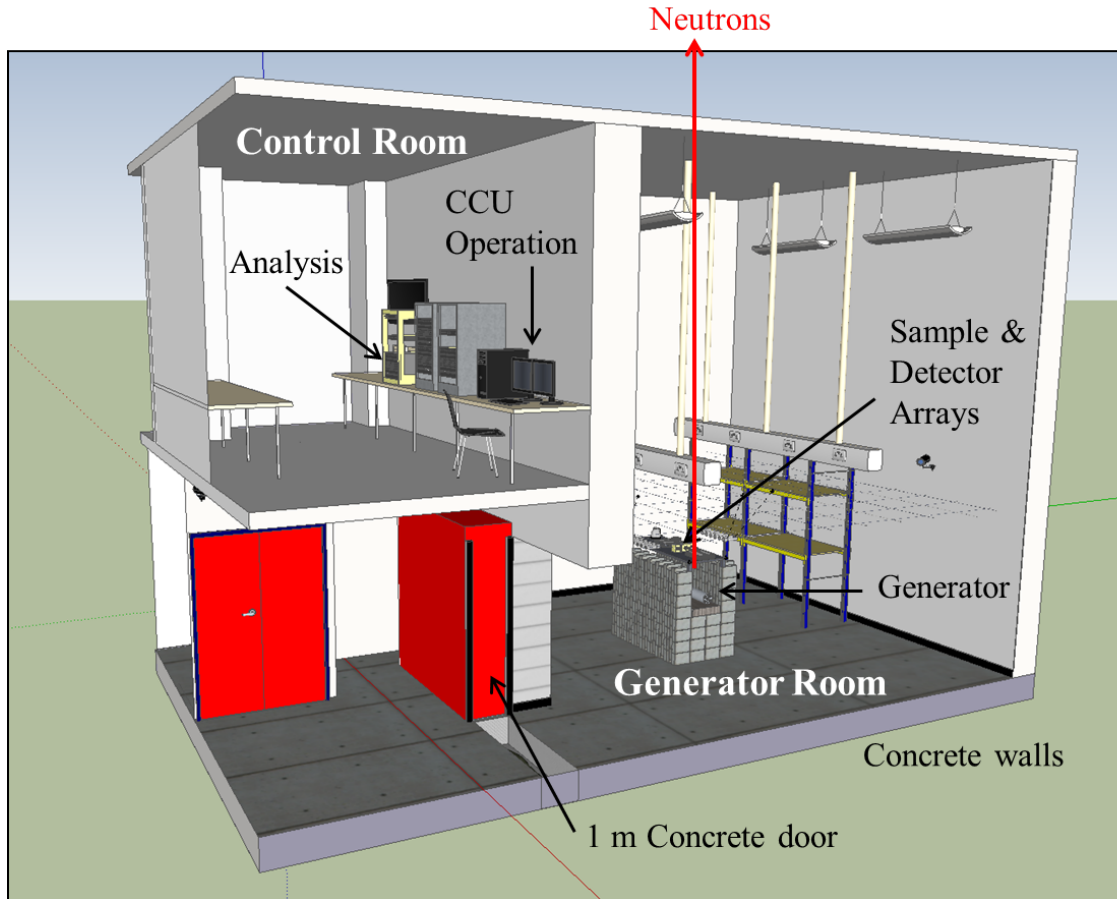


Figure 4.1: *Drawing of the facility*

4.2 The NSD-Gradel Portable Pulsed Neutron Generator (NG)

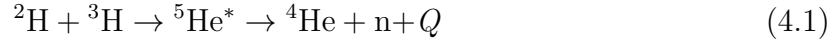
4.3 Neutron Production from the NG

[DESCRIBES HOW THE GENERATOR WORKS - THE CCU, HVPS, PULSE GENERATOR AND TRANSFORMER]

The NSD-Gradel fusion pulsed-neutron generator works under the principle of inertial electrostatic confinement fusion (IEC). HOLLOW CENTRAL CATHODE GRID ETC. By providing the gas ions with enough kinetic energy it is possible to induce fusion reactions such as the deuterium-tritium reaction.

4.3.1 The Deuterium - Tritium (DT) Reaction

The most important reaction is the DT interaction.



A deuterium ion ${}^2\text{H}$ and a tritium ion ${}^3\text{H}$ fuse together to form a single ${}^5\text{He}$ nucleus. This compound nucleus quickly decays (10^{-24} s) with the production of an alpha particle (${}^4\text{He}$ nucleus) and a fast neutron. Using equation 2.18, the Q -value for this interaction is + 17.59 MeV which is split between the kinetic energy of the two. The process can be visualized by figure 4.2 below.

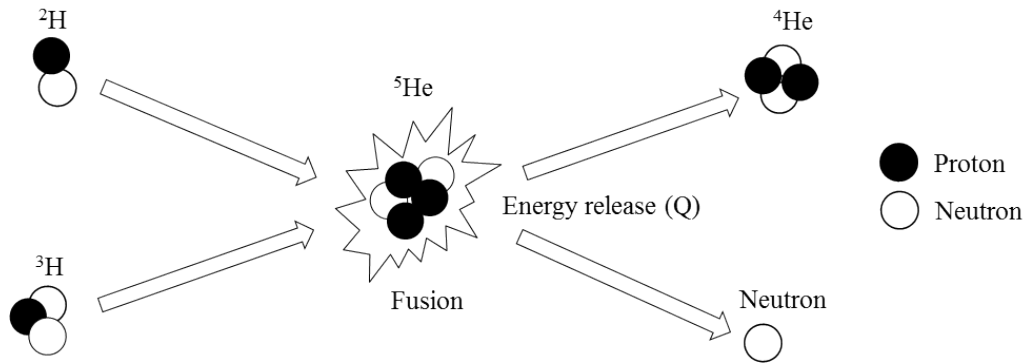
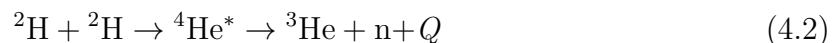


Figure 4.2: *Principle of DT Fusion. Taken from XXXX*

Using equation 2.28 the alpha particle carries away 3.59 MeV of the Q -value meaning that the remainder of the energy goes into the production of a 14.0 MeV neutron.

4.3.2 The Deuterium - Deuterium (DD) Reaction

As well as DT neutrons there will inevitably be fusion between deuterons. The equation for the reaction is written as



Two deuterium ions fuse together to form a single ^4He nucleus which decays with the production of a ^3He nucleus and a neutron. The Q -value for this interaction is $+3.27$ MeV which is split between the kinetic energy of the two. The process can be visualized by figure 4.3 below.

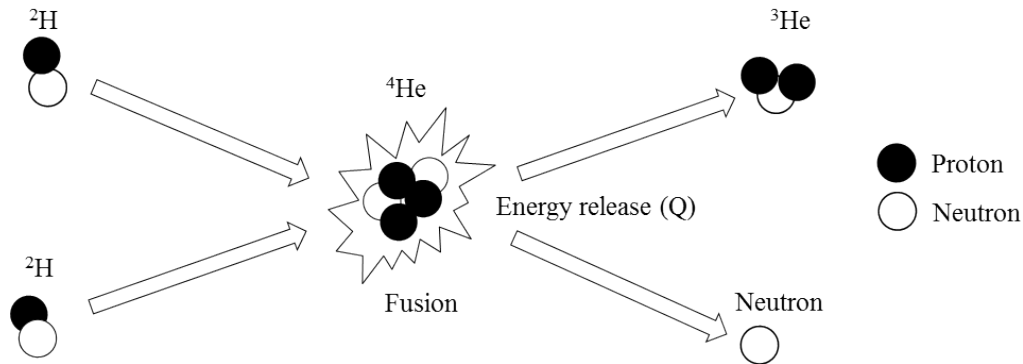


Figure 4.3: *Principle of DD Fusion. Taken from XXXX*

Using equation 2.28, the alpha particle has 0.93 MeV while the remainder, 2.3 MeV, is carried by the neutron.

4.3.3 Neutron generator operation

The generator unit consists of a central control unit (CCU), a high voltage power supply (HV), a pulse transformer (PT) and the reaction chamber (RC). The CCU is used for the sense and control of the overall generator and is linked to software located in the control room in the upper level of the facility where the performance can be monitored both before, and during, operation. The control of the NG is controlled via a front-end user interface which is where the initial start-up sequence is carried out. Initially, a getter temperature of 575 degrees Celsius has to be obtained in order to [release the gas mixture into the reaction chamber - THIS WILL BE IN MUCH MORE DETAIL], this step is performed over an adjustable heating and wait time. For optimum performance the heating time should be between 25 and 35 minutes, with the wait time being between 15 and 25 minutes. Once the NG is in standby mode the selectable options are the input high voltage, the pulse frequency and the pulse width. Frequencies between 2 Hz and 30

Hz are available as well as an additional 'single shot' option. The high voltage unit can deliver up to 600 V to the transformer which has a step-up ratio of 1:140.

In order for the reactions described above to take place, the gas ions must be accelerated to a minimum kinetic energy. Figure 4.4 shows the cross sections for the reactions as a function of the kinetic energy. The DT fusion cross section has a threshold of approximately 5 keV but the cross section does not become experimentally viable until kinetic energies of between 30 keV and 200 keV can be reached, with the peak of the cross-section located at around 80 keV. The manufacturer of the generator provided two operating environments for long-term stable operation and short-term enhanced performance, both of which are related directly to the neutron output. For long term stability, operating parameters of $6.5\mu\text{s}$ pulse width, 30 Hz frequency and 500 V input is recommended. However, for increased performance, the pulse width may be narrowed to $6.0\mu\text{s}$ and the high voltage increased to 550 V. These voltages correspond to acceleration energies of 70 keV and 77 keV respectively, both of which are satisfactory for 14 MeV neutron production (see below) As well as 14 MeV neutron production it is also possible to induce the DD

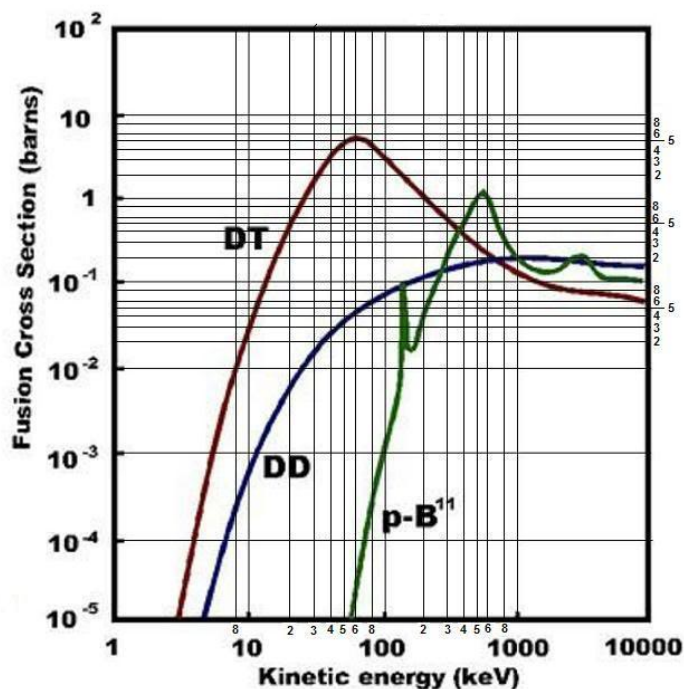


Figure 4.4: Fusion reaction cross-sections for neutron production. [REF]

reaction. However, the cross-section for the DD interaction is approximately 2 orders of magnitude lower than for DT, which means that although present, the DD flux would be substantially lower. It would be expected that there would be a neutron emission spectrum that contains two dominant peaks at 2.3 MeV and 14 MeV respectively.

4.3.4 Output Monitoring During Operation

Absolute calibration of the neutron flux required offline analysis which is the subject of a later chapter. However, real-time monitoring of the relative flux is also necessary. This was achieved using a Bonner sphere. The Bonner sphere consists of a ^3He neutron detector surrounded by a polypropylene sphere which moderates the neutron flux to thermal energies to be captured on the ^3He . The detector electronics then integrates the signals over a few seconds before displaying either CPS (counts per second) or an absorbed dose (in $\mu\text{Sv/h}$).

The operational parameters which have the greatest significance on the neutron output are the voltage applied to the pulse transformer and the getter temperature. Given that the manufacturer recommends running at 500 V it was useful to observe how the Bonner readout changed as a function of getter temperature. The default value was set to 564° C but it was observed over several tens of run hours that the Bonner reading deteriorated over time and it was suspected that the getter was not operating at its peak temperature and was reducing the neutron output - [explanation of how the getter works and how the hydrogen isotopes remain in the wall if a sufficient temperature isn't achieved - thus the number of ions in the reaction chamber reduces and hence the output - also explain how this leads to 'wall effect' insamuch as with the ions trapped in the getter and the nature of the chamber, ions can be accelerated into the wall of the chamber and neutrons can be produced over a wider area than that contained in the centre - This deviates the 'point source' theory (we know it's not a point source)... further still from being a point!!.

4.3.5 Experimental Method

A plot of flux ($\mu\text{Sv/h}$) against getter temperature was plotted to obtain a value for optimum output. The generator was set with an initial temperature of 555°C and allowed to run for a 5 minute period. Once the reading on the Bonner sphere had stabilized a further 2 minutes was observed before a reading was taken from the device. The getter temperature was increased by 5°C and the process repeated. This was continued until a maximum temperature of 590°C was observed. Figure 4.5 shows the result.

The fit of the curve is included and allows an approximate flux to be calculated for a

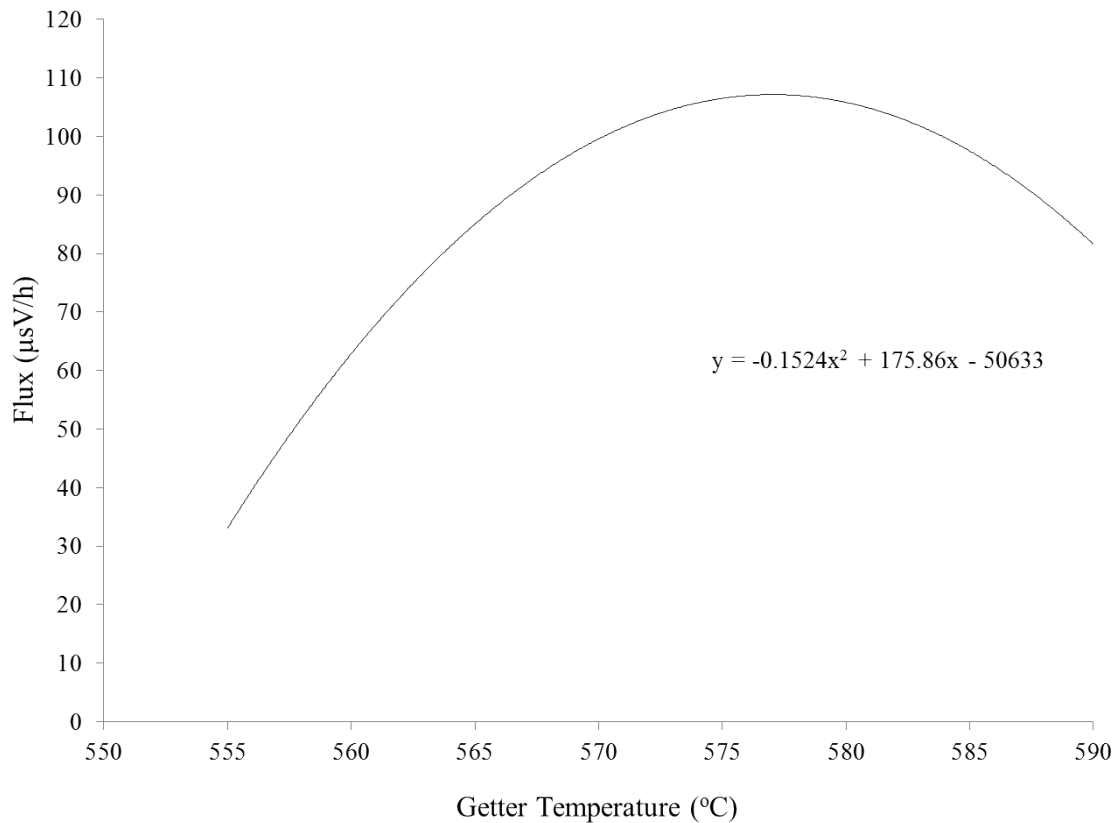


Figure 4.5: *Plot of absorbed dose against getter temperature for NG operation at $500\text{V}/30\text{Hz}/6.5\mu\text{s}$*

given getter temperature. This can then be verified against the Bonner sphere readout as a calibration tool at any point in the future, thus allowing a periodic assessment of peak performance and output.

The plot also shows that at the default temperature of 564°C the output is $(12.0 \pm 0.8)\%$ lower than can be achieved at a temperature of between 575 and 580°C respectively. It was therefore decided to use a new default of 575°C for the remainder of the experimentation and characterization. [INCLUDE IMAGE OF BONNER SPHERE STRUCTURE]

ERROR BARS ON PLOT

SHOULD THIS BE IN RESULTS? OR NOT IN AT ALL?

Chapter 5

Proton Recoil Detectors for Fast Neutrons

5.1 Introduction

As stated in chapter 2, neutrons are charge neutral particles and are therefore not affected by the Coulomb force when incident on a medium. This means that the neutron only interacts with the nucleus of the atom. As the volume of the nucleus is only a small part of the atom as a whole, neutrons can penetrate deeply into matter, making their detection challenging.

Standard charged particle detectors are ineffective at directly detecting neutrons; instead, positive detection relies on the observation of secondary products emitted as a result of either neutron capture or neutron scattering events.

For thermal neutrons, detectors are generally based on isotopes with large neutron capture cross-sections such as ^3He , ^6Li and ^{10}B , while for fast neutrons, detection is generally based on either conversion of all, or part, of the neutron energy into a recoiling nucleus via scattering interactions, where the charged nucleus can then be detected using conventional

charged particle detector materials, or moderation of the fast neutron to low energy and subsequent detection via a capture reaction.

Detectors based on ^3He and ^6Li are expensive¹ and becoming even more so, especially for ^3He based devices with the cessation of tritium production after the Cold War [ref]. This is contrary to our requirements for a cheap, robust and easily reproducible detector.

5.2 The Hornyak button

In the 1950s, Hornyak [11] developed a neutron detector based on fine particles of the inorganic scintillator silver-doped zinc sulfide, $\text{ZnS}(\text{Ag})$, suspended in a plastic matrix of polymethyl methacrylate (which is commonly referred to by its trade names of Lucite, Perspex or Plexiglas).

After an elastic collision with a fast neutron, a hydrogen nucleus in the plastic would recoil, and, upon encountering a scintillator grain, would produce ionization photons which could be detected by a photomultiplier tube.

The aim of Hornyak's design was to produce a detector capable of detecting fast neutrons from a plutonium-beryllium (Po-Be) source in an intense gamma background, by utilizing the decay characteristics of the ZnS phosphor [ref - Hornyak 1952].

As the diameters of the scintillator and plastic powder grains were approximately equal, a thorough mixing of the powders would yield a nearly homogeneous matrix structure once the Lucite had set.

Hornyak designed the detectors by estimating a mix ratio of the powders, by estimating the average range of a recoiling proton in Lucite after a collision with a neutron of 4 MeV (the average energy of a Po-Be neutron), and assuming that the proton would then go on to encounter at least one ZnS grain within this recoil distance.

¹Especially if the ^6Li is isotopically enriched

Figure 5.1 shows the design principle.

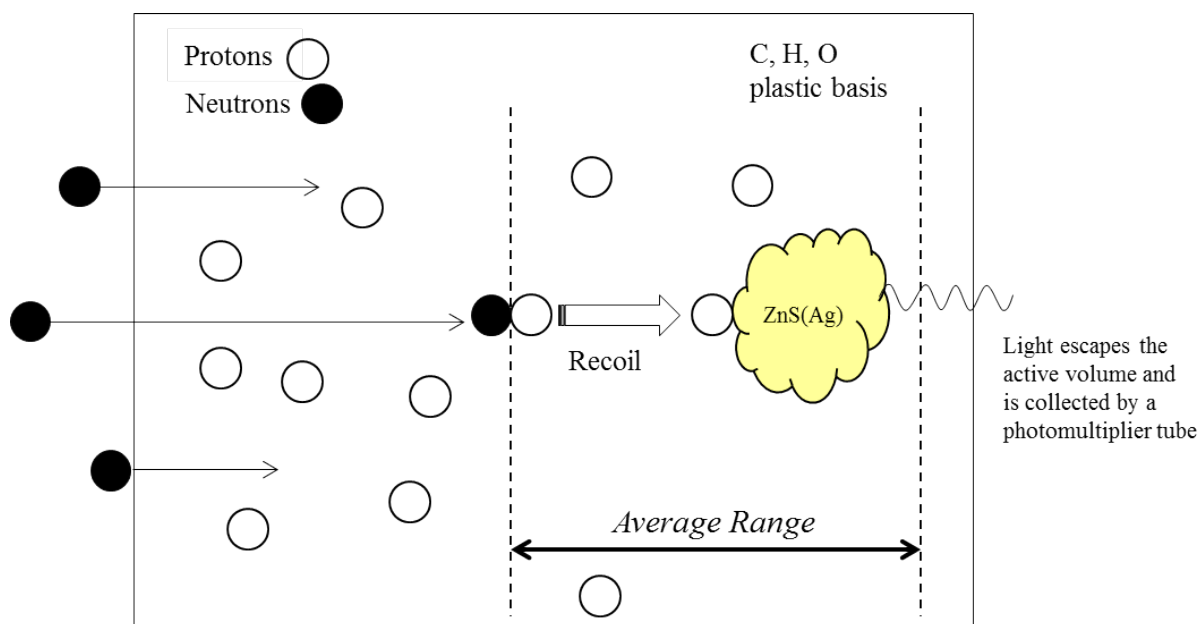


Figure 5.1: *Principle of proton recoil in scintillator-doped plastics*

Hornyak concluded a ratio of 1.5 grams of ZnS to 10 grams of Lucite was optimum for 4 MeV neutrons. The ZnS/Lucite mix was then moulded into 1" (2.54 cm) diameter disks and surface polished to a thickness of $\frac{1}{4}$ inch. An aluminium reflector was placed on one surface and the other surface was oil coupled to an RCA 5819 photomultiplier tube.

While Hornyak's original detectors were small, so-called "Hornyak buttons", the technology is low-cost and the fabrication procedure is simple, and it was therefore decided to investigate the production and performance of this technology for our application.

5.3 The Theory of Hornyak Button Design

5.3.1 Recoil Proton Energy Loss

After an elastic collision with a fast neutron, the resulting energy loss of the proton in a given medium is primarily dependent on the impact parameter of the incident neutron,

the energy of the neutron, and the type of medium it is travelling through. For hydrogen protons, the energy distribution of the recoils should be rectangular in shape, with a magnitude of zero up to the full neutron energy.

This means that the response function of a detector based on hydrogen scattering should have an equally rectangular shape as shown in figure 5.2 [22].

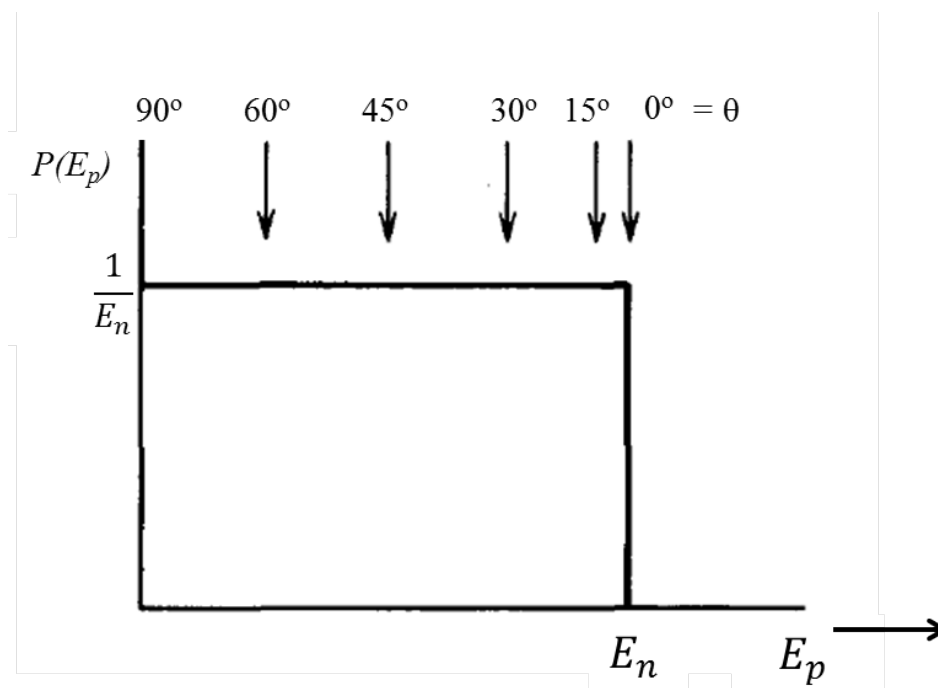


Figure 5.2: *Rectangular shape of hydrogen proton recoil energy distribution*

Thus, the average energy transferred to a proton over all scattering angles $\langle E \rangle_p$, can be assumed to be half of the incident neutron energy. This relationship can then be used to estimate the average recoil range of a proton in a given medium.

From the instant the proton recoils it begins to lose energy by exciting, or ionising, the surrounding atoms. Because the maximum energy transfer between a proton and an atomic electron is approximately $\frac{1}{500}$ of the initial energy per collision, it will take multiple collisions to bring the proton to rest. Initially, while the proton is relatively energetic, the energy loss per unit distance of the particle is small. However, after many collisions the energy, and hence the velocity, of the proton, will fall to much lower levels

and the energy loss per unit distance will increase dramatically.

The well-known equation which describes this energy loss of a charged particle in a medium is the Bethe-Bloch formula which can be written as [22]

$$-\frac{dE}{dx} = \frac{4\pi e^4 z^2}{m_0 v^2} N B, \quad (5.1)$$

where ze and v are the charge and velocity of the particle traversing the medium, N is the number density of the absorber, and B is a relativistic correction:

$$B = Z \left[\ln \frac{2m_0}{I} - \ln \left(1 - \frac{v^2}{c^2} \right) - \frac{v^2}{c^2} \right]. \quad (5.2)$$

For non-relativistic charged particles (as is the case in this application), only the first term in B is important and therefore equation 5.1 can be written as

$$-\frac{dE}{dx} = \frac{4\pi e^4 z^2}{m_0 v^2} N Z \left[\ln \frac{2m_0 v^2}{I} \right]. \quad (5.3)$$

where Z is the atomic number and I is the ionization potential of the absorber medium.

5.3.2 Mass ratio

Figure 5.3 shows the ZnS scintillator embedded in a plastic cube of volume R^3 where R is the average range of the recoil proton.

As the aim of this work is to produce a homogeneous material, the calculations below assume, for simplicity, a regular lattice of scintillator grains as sketched in figure 5.3.

The mass of the plastic contained within the cube can be calculated using the density of the detector medium ρ_{res} and the radius of a zinc-sulfide grain r_g

$$M_{res} = \rho_{res} \times V = \rho_{res} \left(R^3 - \frac{4}{3} \pi r_g^3 \right) \quad (5.4)$$

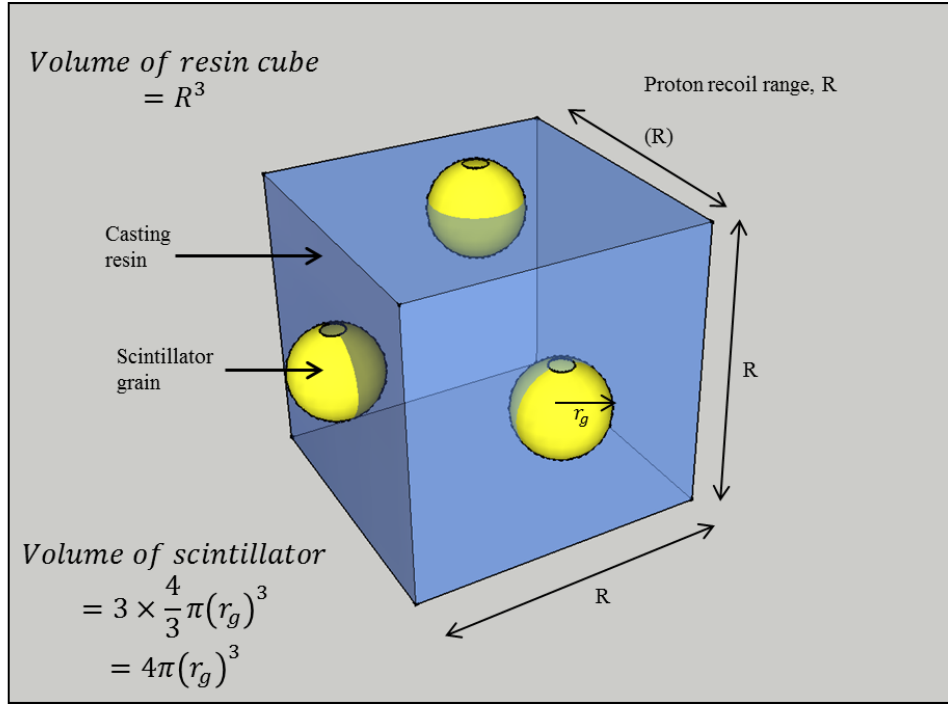


Figure 5.3: Diagram showing a cube of casting resin with embedded scintillator grains

where V is the volume of the resin and r_g is the average radius of a scintillator grain.

The total mass of the scintillator per cube is simply the mass of the three grains embedded within the plastic

$$M_{scint} = 3 \times \rho_{scint} V = 3 \times \rho_{scint} \times \frac{4}{3} \pi r_g^3 = 4\pi \rho_{scint} r_g^3 \quad (5.5)$$

Thus, the mass ratio is a dimensionless number which is a function of the density of the resin and scintillator, the proton recoil range, and scintillator grain size.

$$\frac{M_{scint}}{M_{res}} = \frac{4\pi \rho_{scint} r_g^3}{\rho_{res} \left(R^3 - \frac{4}{3} \pi r_g^3 \right)} \quad (5.6)$$

5.3.3 Detector Materials

An ongoing and important aim was to be able to build the detector as cheaply as possible using readily available off-the-shelf products. In the arts and crafts industry, there were

found to be many plastic resins manufactured for use in a broad range of applications, such as encapsulation, preserving biological samples and decorative castings. As a result, there were many reasonably priced sources on the market all of which supplied similar products under different trade names.

The resins were generally available as two-part products consisting of an alkyd liquid containing a percentage of polymer solution suspended in a styrene monomer, and a catalyst or liquid hardener, which when mixed together initiated cross-linking to form solid plastics [39].

We chose an acrylic modified polyester casting resin supplied by Alec Tiranti Ltd [REF] which contained approximately 61% carbon, 6% hydrogen and 33% oxygen by mass ($C_{27}H_{32}O_{11}$) and had a density of 1.1 g cm^{-3} when cured [40]. This product was selected as it cured to a clear plastic with a similar refractive index to glass and was intended to be mixed with a dye to alter its colour. It was therefore assumed that a small amount of powdered scintillator could be added without affecting the setting process.

5.3.4 Calculating the Range, R

The recoil range of a nucleus in a medium can be calculated using the TRIM [ref] program, which calculates the stopping distance of ions in matter. Because we know the average energy transferred by a neutron to the nucleus, and the chemical composition of the medium, it is possible to assess the suitability of a material using the TRIM database which estimates the average nuclear recoil range, R , over all scattering angles, in a given material.

A new compound was added to the TRIM database using the chemical formula of the Tiranti resin. The average proton recoil range for any incident neutron energy could be ascertained by making the “ion data” represent a proton of energy $\frac{1}{2}E_n$.

Figure 5.5 shows an example of the TRIM output for both the longitudinal range of the

protons (left) and ionization, as a function of depth into the resin (right) for 14 MeV neutrons.

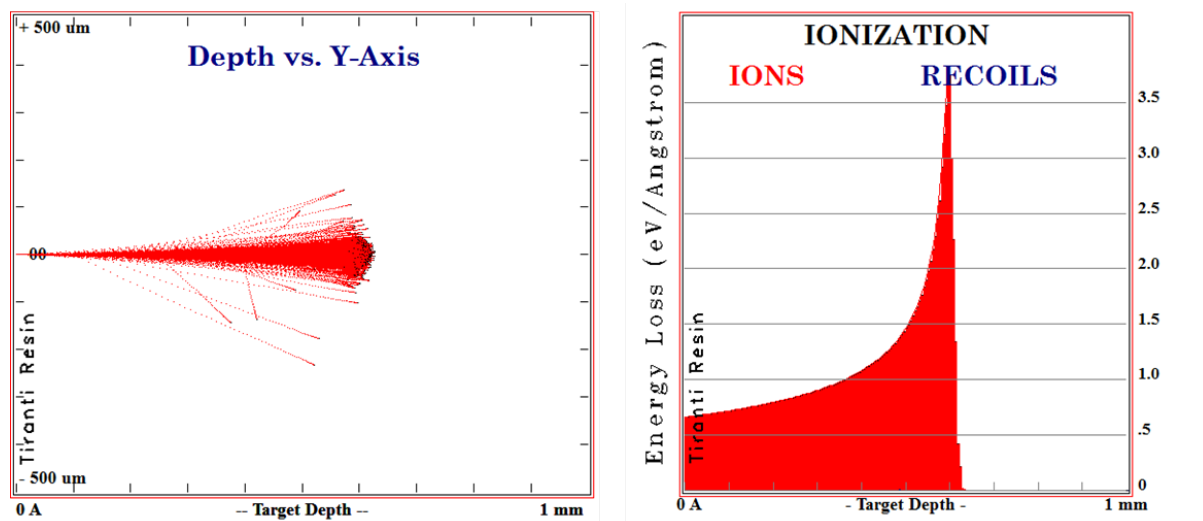


Figure 5.4: (left) TRIM output of average proton recoil range into polyester casting resin for 14 MeV incident neutrons. (right) ionization as a function of depth.

The average recoil range for 14 MeV neutrons (7 MeV recoil protons) over all scattering angles is 605 μm , with the majority of the energy deposition occurring in the final 10 microns. Assuming that the recoiling proton encounters a ZnS grain within this range, a scintillation flash will occur which can be registered by a photomultiplier tube, as sketched in figure 5.1.

Using the TRIM database it was possible to produce a plot of average proton recoil range as a function of incident neutron energy, figure 5.5. For neutrons of 1 MeV the average range is short at around 8 microns. As the incident neutron energy increases, more energy is transferred to the recoiling proton and hence the range in the plastic also increases. This is an important factor when designing a detector based on proton recoil and will be discussed in subsequent sections.

It is now possible to replace the R^3 term in equation 5.6 by the equation of the line in figure 5.5 and substitute for ρ_{scint} (4.09 g cm^{-3}), r_g (10 microns) and ρ_{res} (1.12 g cm^{-3}) to obtain

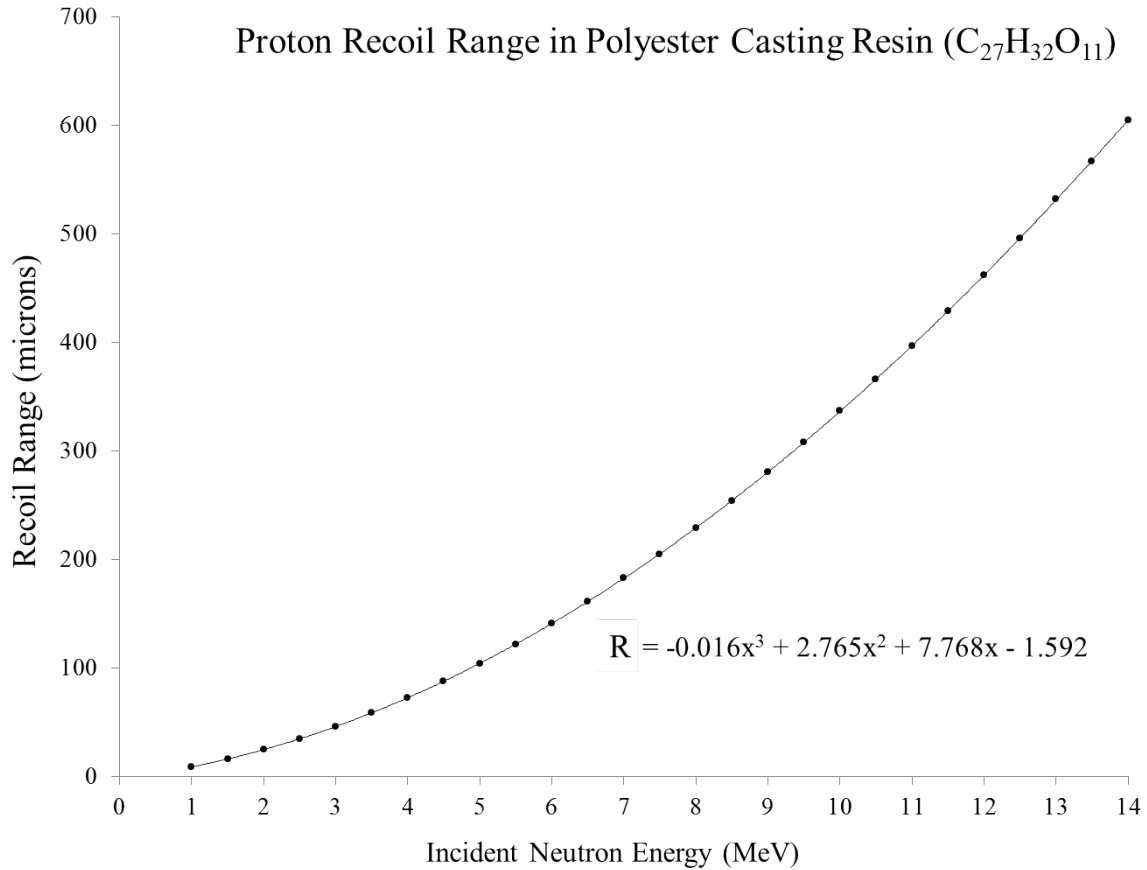


Figure 5.5: Plot showing the proton recoil range into our polyester casting resin when subjected to incident neutrons between 1 MeV and 14 MeV. The fit is a polynomial used to calculate the range R in this energy regime, to be used in equation 5.7.

$$\frac{M_{scint}}{M_{res}} = \frac{4\pi \times 4.09 \times 0.001^3}{1.12 \times (-0.016x^3 + 2.765x^2 + 7.768x - 1.592)^3}, \quad (5.7)$$

where x is the incident neutron energy in MeV. This equation can be used to determine the optimum mass ratio for any desired size of Hornyak button.

Hornyak [11] used a mass ratio of 10 grams of Lucite powder to 1.5 grams of ZnS was used for 4 MeV PoBe neutrons. By using equation 5.7 with an x of 4 MeV we get a mass ratio of 0.16. Using the dimensions of Hornyak's button, the mass of Lucite powder required is 10.2 grams with a mass of 1.6 grams of ZnS. This agrees well with the result in Hornyak's paper and adds validity to our design process.

Casting and Testing

It was anticipated that the efficiency of a 14 MeV detector would be very poor when exposed to lower energy neutrons (specifically the 2.3 MeV DD component of the generator, and the facility AmBe and ^{252}Cf sources), and because generator characterization and shielding considerations would require a range of neutron energies, it was decided that a multi-purpose button should be fabricated in an attempt to detect a wider neutron energy range.

A number of 2" (5.08 cm) EMI 9954 KA photomultiplier tubes were readily available, so it was decided to fabricate buttons of this diameter.

A spreadsheet was produced which would calculate the exact mixing ratio for a given scintillator, incident neutron energy, and detector dimensions. Figure 5.6 shows the inputs (in salmon) and the outputs in red font.

Producing this template meant that it was possible to experiment with the incident neutron energies using the fit from the data in figure 5.5 as the R^3 term in equation 5.7, before deciding on an optimum mixing ratio to cover as wide a range of neutron energies as possible.

	A	B	C	D	E	F	G	H	I					
1	Template For Hornyak style button mixing ratio - For any scintillator and plastic													
2														
3														
4														
5														
6	Neutron Energy	4	MeV											
7														
8														
9	Fit of recoil data, (R^3) term			$\frac{M_{scint}}{M_{res}} = \frac{4\pi\rho_{scint}r_g^3}{\rho_{res}(R^3 - \frac{4}{3}\pi r_g^3)}$										
10	1	-0.016												
11	2	2.765												
12	3	7.769												
13	4	-1.592												
14														
15	Proton recoil range	72.689	μm											
16														
17	Density of Scintillator (g/cm^3)	4.095			Mass of scintillator	2.7157	grams							
18	Density of plastic (g/cm^3)	1.125			Mass of resin	22.8018	grams							
19	Average scint grain diameter (μm)	10												
20	Diameter of detector (cm)	5.08												
21	Thickness of detector (cm)	1												
22														

Figure 5.6: *Diagram*

Using the spreadsheet in figure 5.6 with button dimensions of 5.08 cm in diameter and an arbitrary thickness of 1 cm, and optimising for 14 MeV neutrons, the calculated mass ratio was

$$\frac{M_{scint}}{M_{resin}} = 2.01 \times 10^{-4}. \quad (5.8)$$

while for 2.3 MeV neutrons the result was

$$\frac{M_{scint}}{M_{resin}} = 1.84. \quad (5.9)$$

The magnitude of the mass ratios showed that a much larger proportion of zinc sulfide was required in the button to accommodate the much shorter proton recoil range associated with the lower energy neutrons. This meant that equation 5.7 would break down when the average proton recoil range was comparable to the diameter of the scintillator grain (approximately 10 μm for 1 MeV neutrons) at which point the mass of scintillator required would be significantly greater than the mass of resin and a button could not be cast. This breakdown was evident up to neutron energies of around 3 MeV where the recoil range had only increased to around 45 μm and the mass of scintillator needed was still large.

A decision was therefore made to follow Hornyak's work, and base the fabrication on an average neutron energy of 4 MeV, at which point the average recoil range is significantly larger than the grain diameter, being sufficiently long that the amount of scintillator required would not be large enough to compromise the setting process, yet would be short enough to allow a wide range of neutron energies to be detected using the same button.

In order to determine the optimum detector thickness (rather than the arbitrary 1 cm mentioned above), a series of buttons of varying thickness were produced in order to investigate the opacity of the detectors to the scintillator emissions. Several casts ranging from 2.5 mm to 15 mm were produced using a mould consisting of an aluminium block with a 4 cm deep well. In the centre of the well a 5.3 cm (2.1 inch) diameter by 2.8 cm

thick cylindrical piece of aluminium was attached.

Using this template, the RTV silicone mould rubber could be poured in and left to set, producing a 2.8 cm deep cylinder to which the casting resin and scintillator mixture could be added. A series of buttons of thickness 2.5 mm, 5 mm, 7.5 mm, 10 mm and 15 mm were then produced. Figure 5.7 shows the mould template and figure 5.8 shows the finished detectors.

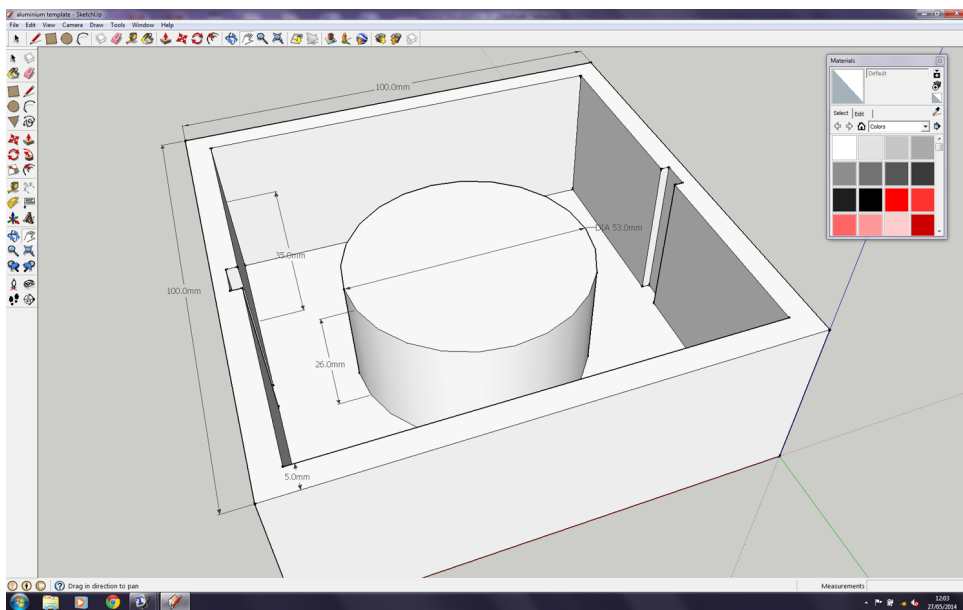


Figure 5.7: Aluminium mould template for casting the fast neutron buttons

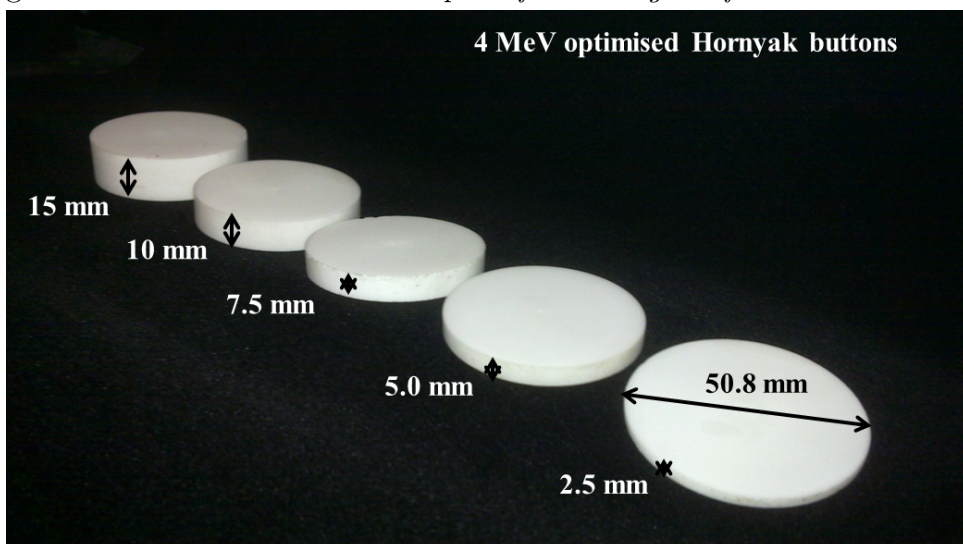


Figure 5.8: Cast and polished Hornyak style buttons of varying thicknesses.

The buttons were placed individually in a dark box and coupled to a PM tube. Light pulses were generated by a IBH NanoLED system [18] and passed through each button in order to assess the transparency of the detector. A 455 nm LED was selected to approximately match the peak emission wavelength of the scintillator. Figure 5.9 shows the experimental setup.



Figure 5.9: *IBH NanoLED [18] system with a Hornyak style button coupled to a 5 inch diameter EMI 9791 KB photomultiplier tube*

A series of 5 runs was undertaken for each of the button thicknesses and the mean pulse height and standard error on the mean recorded. A plot of relative pulse height against button thickness could then be produced. Figure 5.10 shows the data obtained for the experiment.

The data showed that as the thickness of the button increases, the level of self-absorption by the ZnS(Ag) content of the button increases.

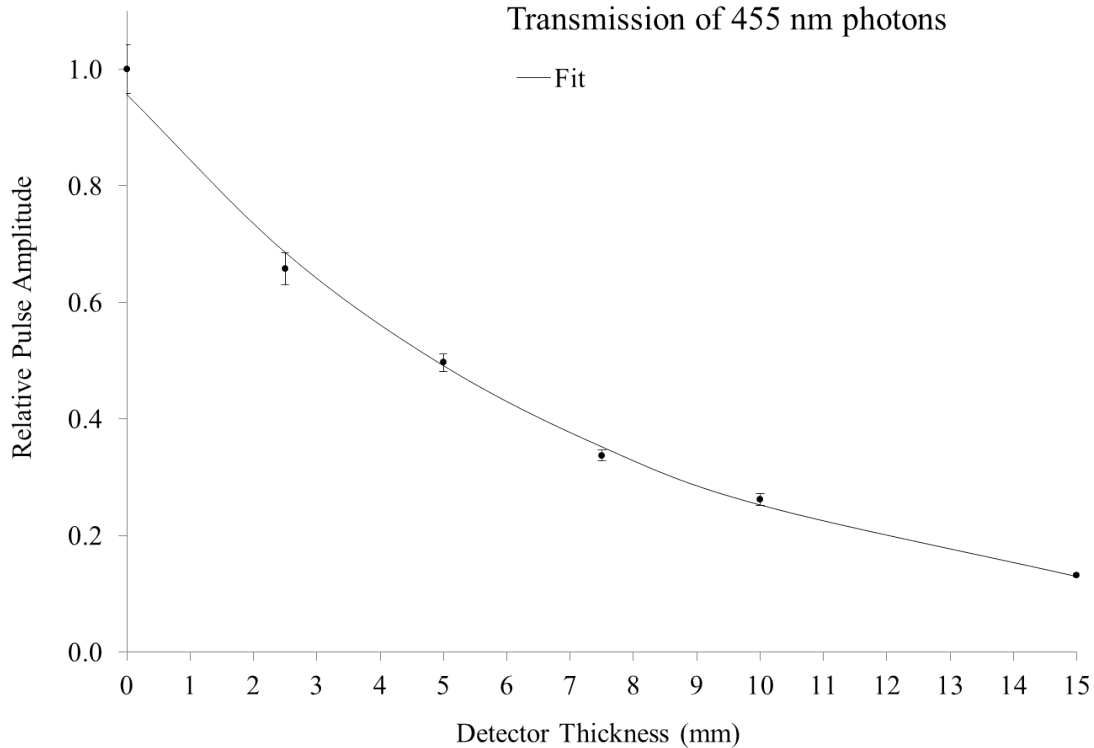


Figure 5.10: *Pulse height as a function of button thickness for several detectors. The half-value thickness is highlighted.*

The half-value thickness of 5.2 mm, derived from an exponential fit with $a = 0.957$ and $b = -0.133 \text{ mm}^{-1}$, was selected as the optimum thickness for the selected mixing ratio and all subsequent buttons were produced to these specifications.

5.3.5 Detector Configuration and Signal Processing

The anode output from an uncoupled 9954 KA photomultiplier tube was fed into a LeCroy Waverunner 104 MXi 1 GHz oscilloscope and the pulses observed. The level was increased until the random noise from the tube was suppressed and the oscilloscope level recorded².

One side of a Hornyak button was mounted onto a 2" diameter disc of aluminized mylar

²The discrimination level was sufficient to suppress the low amplitude background noise from the tube. However, there were many large spikes of hundreds of millivolts still being recorded. This is addressed in the next section.

using a small amount of low tack adhesive spray, the other side was optically coupled to the tube with a 2" diameter by 1 mm thick Slygard pad.

The tube was housed in a μ -metal shield and 1 mm thick aluminium casing. Black insulating tape was used to cover any joins in the casing and the detector was left for 24 hours to allow the ZnS to relax after exposure to ambient light.

After this period the noise level was reassessed and compared to the previous results in both a dark and light environment to make sure that there were no light leaks in the detector. The detector was then incorporated into the signal processing chain depicted in figure 5.11.

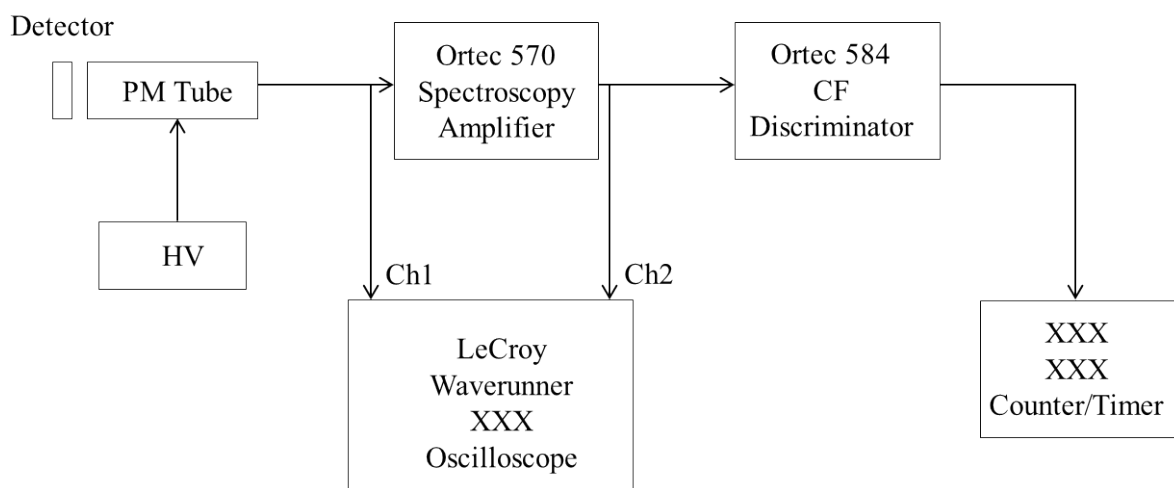


Figure 5.11: *Signal processing chain used for pulse shape discrimination*

The tube output was fed into the Ortec 570 spectroscopy amplifier with a 3 μ s pulse shaping time. The shaped pulse was a unipolar Gaussian, with a pulse height proportional to the integrated charge. These signals were then sent to an Ortec 584 constant fraction discriminator.

The detector was placed in a natural background environment and the level on the discriminator set to zero. The threshold level was then increased incrementally until the low amplitude tube noise was suppressed. With no neutrons present there were occasional large amplitude/narrow width voltage spikes most likely caused by background cosmic

ray interactions in either the photocathode, or the dynode chain, some of which were large enough that when integrated over $3 \mu\text{s}$ would cause a trigger. However, the discrimination level remained low so not to risk losing real, small-amplitude neutron events in the detector. Figure 5.12 shows a comparison between signals obtained by having the detector in the neutron flux from a ^{252}Cf source, placed on the detector top (bottom image), and with no source present (top image)

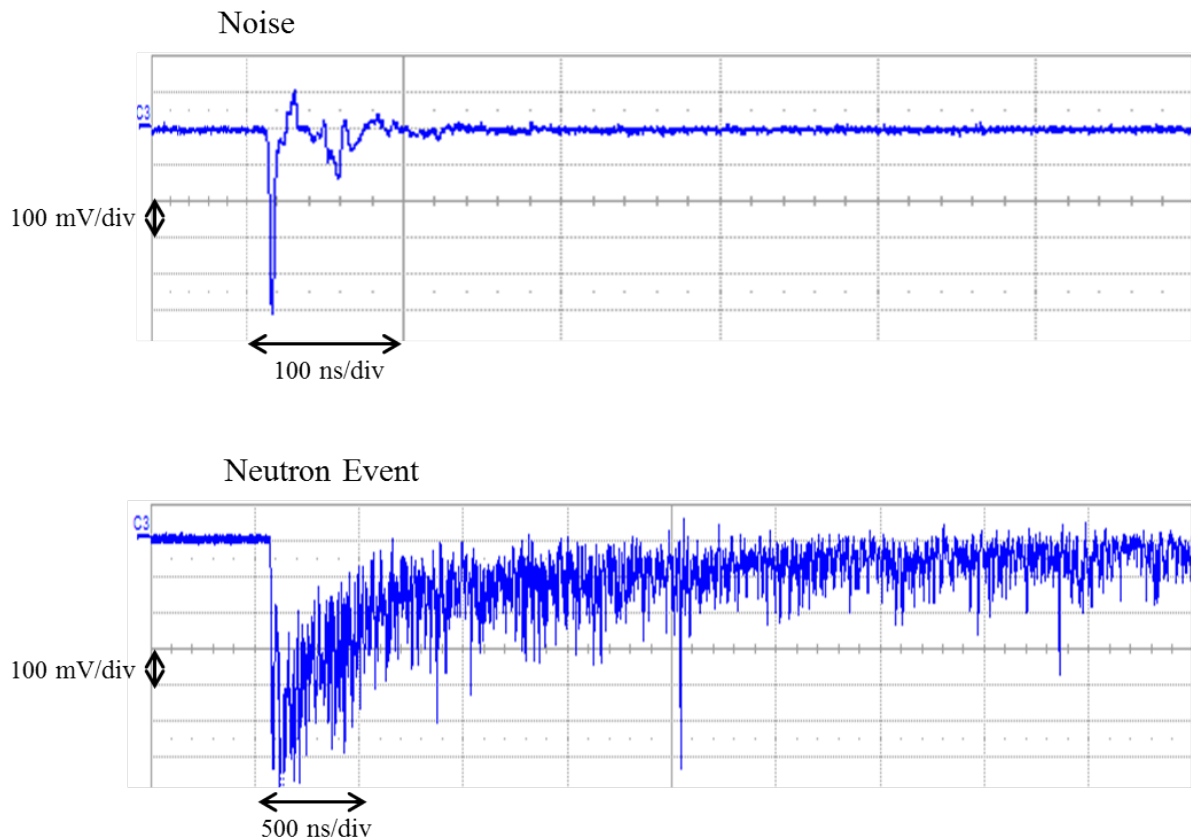


Figure 5.12: *Pulse shape comparison between random photomultiplier tube noise and a recoil proton ionizing the $\text{ZnS}(\text{Ag})$ scintillator. Note, the neutron induced pulse also shows a superimposed noise pulse approximately $2 \mu\text{s}$ into the event.*

The first experiment was a simple count of events over a 3 minute period. Initially, there was no source present; then the detector was exposed to a $2.85 \text{ kBq } ^{252}\text{Cf}$ source which emitted a continuous spectrum of neutron energies with a “most probable” energy of approximately 2 MeV [16] and finally, a $37 \text{ kBq } ^{137}\text{Cs}$ gamma source. Figure 5.13 shows the result.

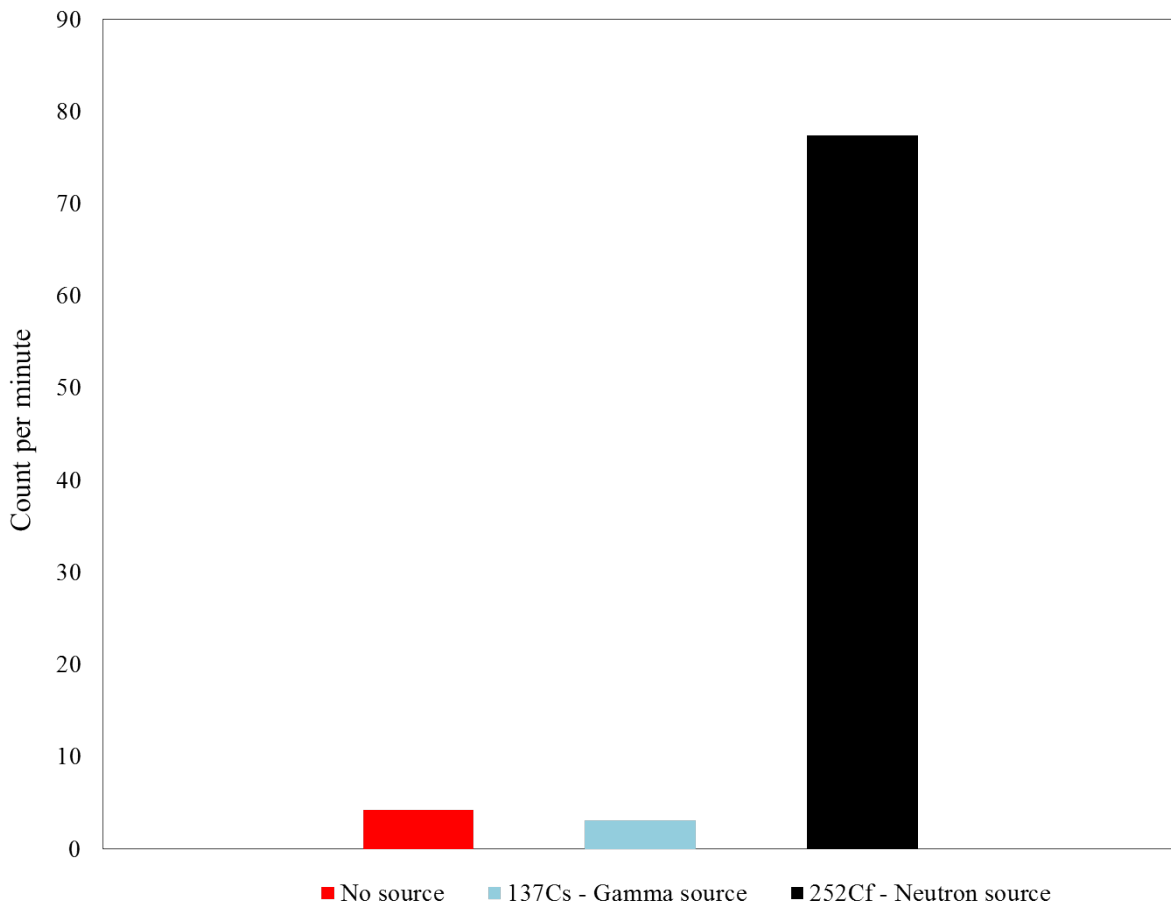


Figure 5.13: *Count comparison between Hornyak button exposure to gamma and neutron source relative to background.*

The plotted data has been background subtracted, where “background” corresponds to the raw photomultiplier tube output with no detector optically coupled to the photocathode and accounts for large amplitude pulses caused primarily by cosmic ray interactions in the dynode material or photocathode. This background can then be subtracted from subsequent data sets thus allowing detector only events to be recorded.

When no source was present, the count was 4.0 ± 0.3 counts per minute, 3.0 ± 0.2 counts per minute during gamma exposure, and 77 ± 5 counts per minute after exposure to the neutron source.

Given the relatively small amount of scintillator present and the way in which gamma-rays interact in the ZnS(Ag), it was expected that the detector would be insensitive to

gamma radiation and there would be no statistical difference in the magnitude of the counts with the difference being consistent with zero. This was not the case as the difference was calculated to be 1.0 ± 0.1 counts per minute. A possible motive for the discrepancy was that the ^{137}Cs source may have been acting as a background shield by generating frequent narrow pulses for which the detector electronics were rejecting due to the high discrimination level. The constant processing of these pulses may have led to cosmic ray interactions being vetoed due to pulse processing dead-time.

It is clear however, that when the detector was exposed to fast neutrons the count increased significantly. This provided confidence that the detectors could indeed be used to detect fast neutrons from various sources with varying neutron emission energies.

5.4 Longer Exposure to Neutrons

The performance of the detector was extended in an attempt to assess whether or not the buttons could be used to observe structure in the neutron emission spectrum of both the ^{252}Cf and americium-beryllium sources.

5.4.1 ^{252}Cf

First, the detector was exposed to the ^{252}Cf source for a 60 minute acquisition and the peak amplitude of the shaped pulses recorded. This shown in figure 5.14. The neutron event rate was calculated to be 80 ± 1 counts per minute which was in good agreement with the initial tests.

The detector was also exposed to a ^{60}Co source, and no source, for the same count duration. The data is compared to the spontaneous fission spectrum of a ^{252}Cf source produced by AEA Technology Ltd, Harwell, Oxfordshire, where the spectrum was measured using a stilbene crystal and pulse shape discrimination [16].

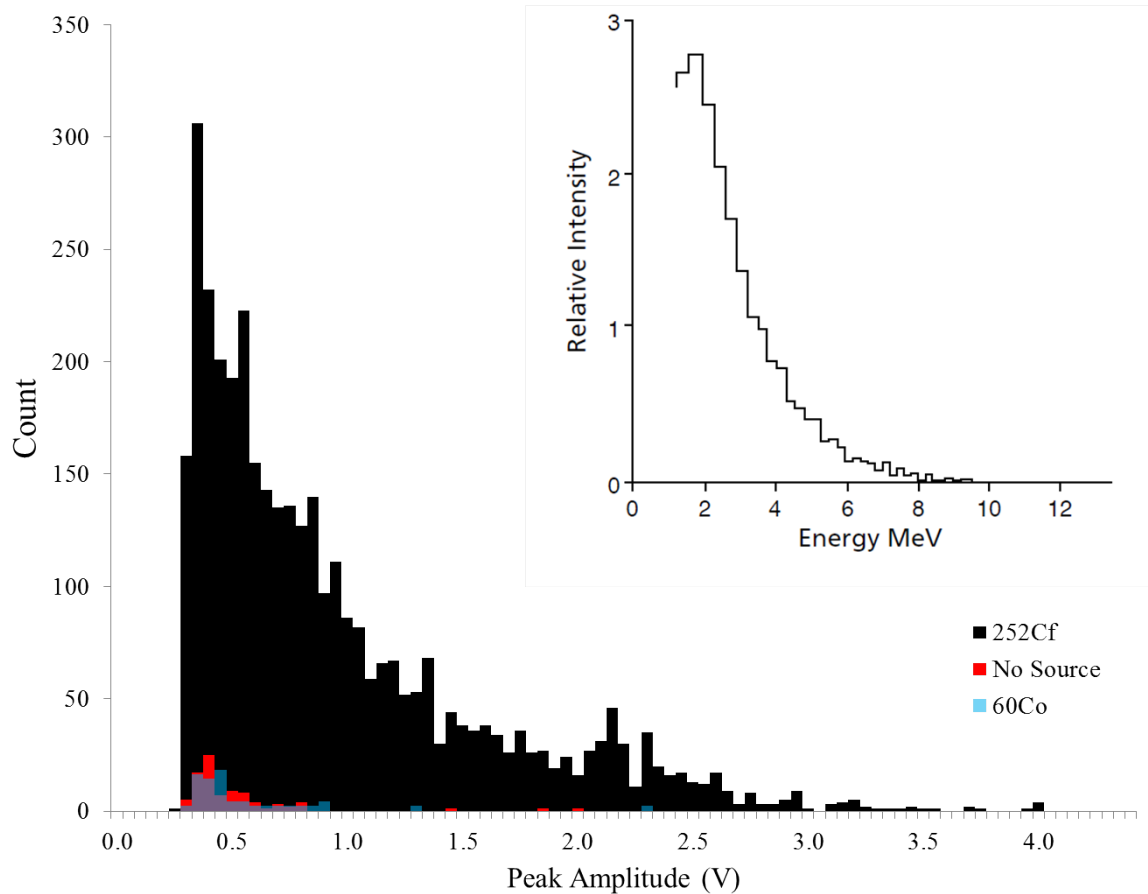


Figure 5.14: *Pulse height spectrum from ^{252}Cf neutrons on a 5.08 cm diameter by 1 cm thick Hornyak button at the University of Sheffield (main). Also, the ^{252}Cf fission spectrum produced by AEA Technology at Harwell, Oxfordshire, UK (inset) [16]*

The result obtained from our detector has the same general shape as the AEA spectrum. However, with no obvious features to correlate, no quantitative comparison is possible in the absence of a calibration to convert peak amplitude to MeV.

As the Hornyak buttons were intended to be used in a multi-detector array for neutron transmission experiments where only a yes/no indicator was required, this was not a major issue at this stage and could be explored further at a later date.

5.4.2 AmBe

The detector was exposed to a XXXX Bq/Ci AmBe source at a distance of 50 cm for 24 hours. Figure 5.15 shows the spectrum along with a comparison AmBe spectrum taken from [44], which is the international standard recommended AmBe neutron energy spectrum.

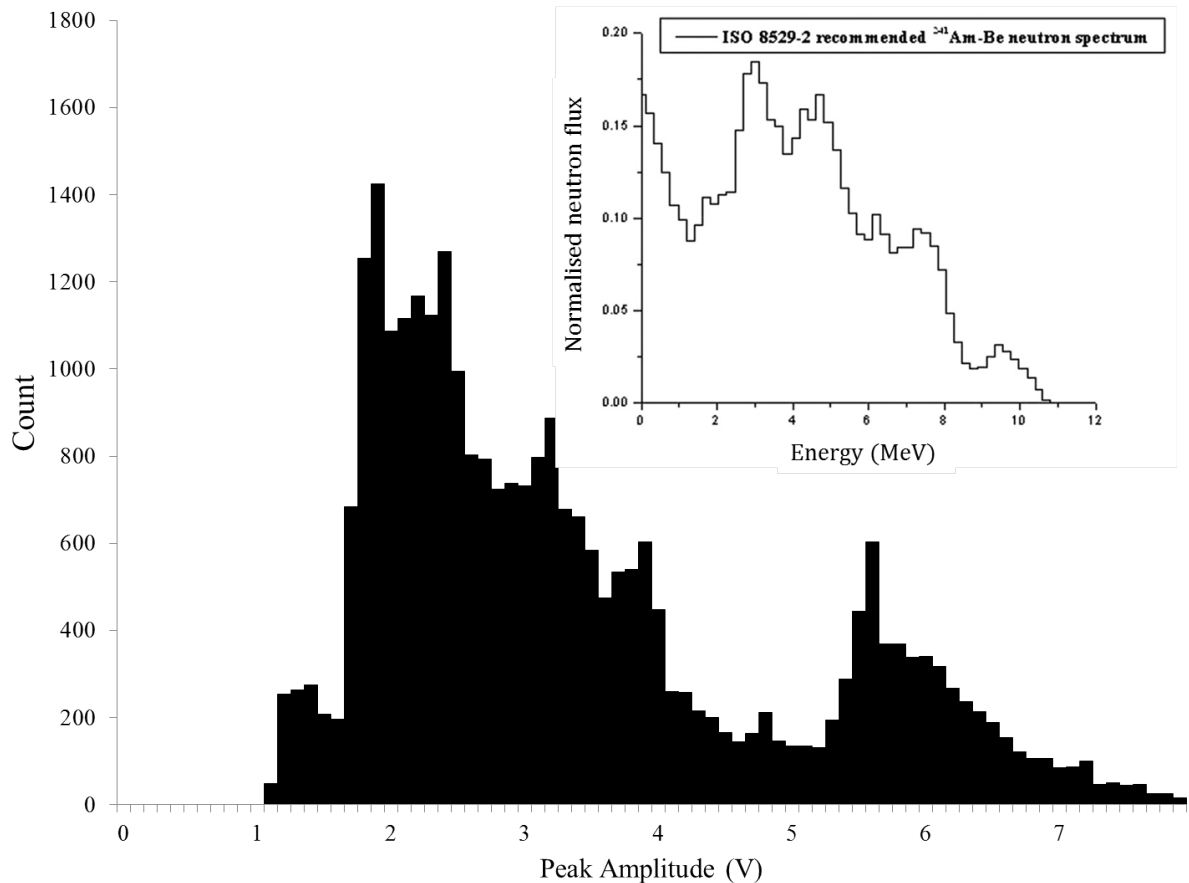


Figure 5.15: Comparison between pulse height spectra from the University of Sheffield americium-beryllium neutron source (main) and the ISO recommended spectrum (inset)

There is some evidence of structural similarities between the distribution produced from our detector and the reference spectrum. However, as with the ²⁵²Cf source, it is not possible to correlate the positions of the spectral features without a calibration of our detector against a known standard. Therefore only a visual impression is provided.

5.5 Detector Efficiency

A simple intrinsic efficiency measurement was carried out on the button using the ^{252}Cf source. Because the source was relatively weak, it was placed directly on the detector top and it was assumed given the isotropic nature of the source, that with this geometry the number of neutrons incident on the button was roughly $\frac{S}{2}$, where S is the number of emitted fission neutrons per second.

The acquisition was carried out for 30 minutes, and the rate R of recorded neutron events was 78 ± 2 per minute, corresponding to 1.30 ± 0.03 neutrons per second.

The efficiency was calculated from

$$\epsilon = \left(\frac{R}{\frac{1}{2}S} \right) \times 100\% \quad (5.10)$$

which gave an absolute detector efficiency of $0.091 \pm 0.005\%$.

Because this is a simple efficiency calculation there is no energy dependence on the value as the source emits a continuous spectrum of neutron energies. However, if the average neutron energy of ^{252}Cf neutrons is around 2 MeV, it can be argued that the detector efficiency corresponds roughly to this energy.

A similar type of detector currently on the open market is the Eljen-410 fast neutron detector, manufactured by Eljen Technology [9]. The Eljen-410 consists of ZnS embedded in a hydrogenous polymer matrix, as in our detector, but incorporates concentric clear plastic cylinders to improve light collection. Its efficiency is 0.67% at 2 MeV.

Factoring in a typical bialkali photomultiplier tube efficiency of $\approx 20\%$, yields an intrinsic detector efficiency of $0.455 \pm 0.03\%$. This suggests that our detector efficiency is broadly similar but slightly lower, as expected from its simpler design.

5.6 Conclusions

A candidate technology for a low-cost, easily reproducible and robust fast neutron detector was considered, and fabricated using readily available materials that were safe to handle with minimal precaution and cheap to buy in the arts and craft industry.

The buttons themselves were very cheap to produce (less than £5.00 sterling per detector) and the bulk of the cost pertains to the price of the photomultiplier tube and signal processing electronics. However, in terms of a “detector crystal” the Hornyak style buttons were orders of magnitude cheaper than comparable market fast neutron detectors with a similar intrinsic efficiency.

The buttons are capable of detecting fast neutrons over a range of neutron energies, from approximately 1 MeV upwards³, and are capable of registering counts from 14 MeV generator neutrons (discussed in chapter 6), making the detectors multi-functional for a range of experiments.

In terms of the cargo screening project, the detectors will eventually be built into a larger array allowing neutron transmission experiments to be performed. The results from the transmission work will allow positional information on the threat object to be ascertained, and this combined with the elemental information from the gamma spectroscopy, will allow a more concise evaluation of the threat to be determined. A thorough efficiency calibration of the detectors will be undertaken using monoenergetic neutron sources in order to investigate neutron emission spectra in further detail.

Finally, we have plans to replace the ZnS(Ag) scintillator with ZnO(Ag) (silver-doped zinc oxide), which has a much faster decay time than ZnS (ns as opposed to several μ s), and could therefore be used to evaluate the neutron generator output pulses in an attempt to ascertain the structure of the pulse shape and the time/duration of the neutron output.

³Although the upper limit of neutron sensitivity is unknown

Chapter 6

Shielding and Collimation of the Neutron Source

6.1 Shielding Requirements

The neutron generator produces an isotropic flux of fast neutrons. Operationally, it is more convenient to have a collimated “beam” of neutrons with minimal neutron flux elsewhere. In order to achieve this it was necessary to design and construct a neutron shielding system with an appropriate geometry, and it was decided that a collimated beam in the upward direction would be advantageous. This design maximizes flexibility allowing many different detectors to be deployed in a variety of configurations, and has structural advantages since collimating the beam upwards allows the weight of the shielding to be supported by the floor.

6.2 Shielding Geometry and Materials

The generator is placed on a bulk collimator with a thickness sufficient to moderate the fast neutrons in the downward and sideward directions. This section was primarily con-

structured from high-density magnetite concrete which contains a number of low-Z elements as well as a large quantity of iron ore. It is also advantageous to borate the shield, so plaster sheets mixed with colemanite [21] were fabricated and interleaved within the concrete stack. Colemanite is a boron rich material, and as boron has a much larger neutron capture cross-section than hydrogen, can absorb thermalized neutrons within the shield, completely removing them from the system and minimizing the amount of diffusion into the detector arrays. Neutron capture on boron also induces a lower energy gamma-ray than those associated with the concrete meaning a few mm of lead at the extremities of the stack would suffice to attenuate any gamma-rays reaching the edges. Figure 6.2 is a 3D drawing of the design. The “beam port” section of the collimator was constructed of borated paraffin wax sheets and edged with lead flashing; and will be discussed in greater detail in the following sections.

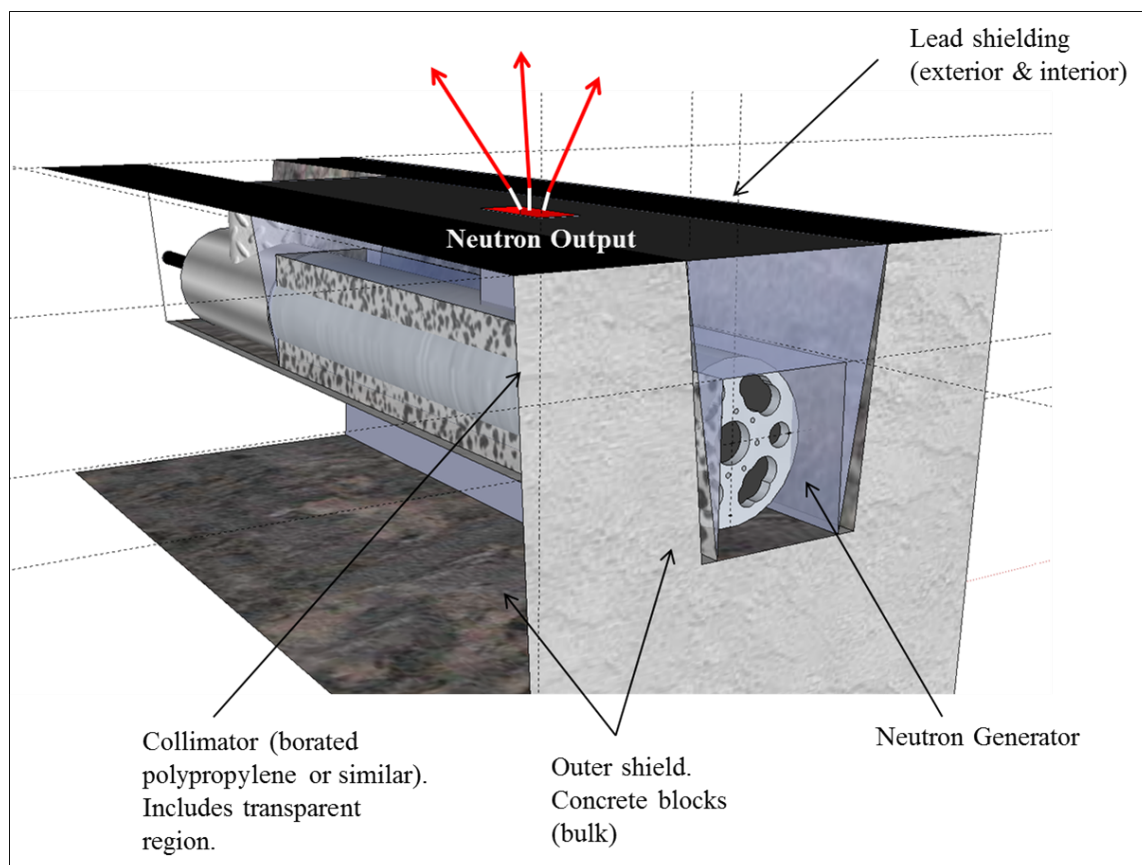


Figure 6.1: *Cut-away drawing of the neutron collimator showing the generator in situ*

6.3 Tests of Shielding Materials

Fast Neutrons

It was necessary to measure the unshielded fast neutron flux at varying distances from the source, thus enabling a comparison to be drawn when moderating materials were added to the experimental setup. First, the front edge of a 5 mm thick fast-neutron recoil button (as described in Chapter 5) was fixed to a clamp at a distance of 3.5 cm from the outer edge of the chamber wall and centred on the reaction chamber. A 0.3 cm lead plate was attached in front of the button to protect the detector from bremsstrahlung radiation. Figure 6.2 shows the experimental setup.

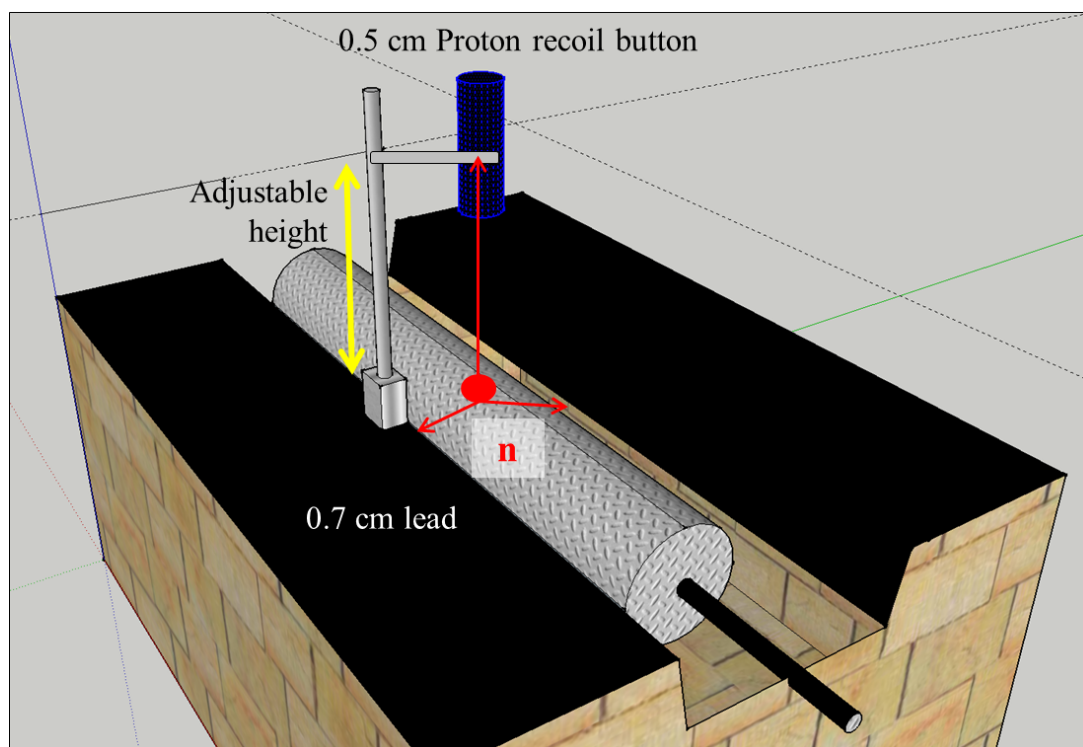


Figure 6.2: *Diagram showing the experimental setup for determining the quality of the collimator materials.*

The number of counts was recorded over a 3 minute period; the counter was zeroed and the experiment repeated until 5 data sets had been obtained so that an average count and standard error on the mean could be recorded. The detector was then moved away

from the chamber incrementally and the acquisition repeated up to a distance of 50 cm. The experiment was then repeated using increasing thicknesses of moderating material. A 3.5 cm sheet of polypropylene was placed between the outer edge of the generator and the face of the recoil button. An average count was taken before the source-detector distance was increased by adding a second 3.5 cm thick sheet of polypropylene to form a layered stack. The procedure was repeated until a stack thickness of around 50 cm had been tested. The experiment was then repeated again, this time by replacing the polypropylene sheets with borated paraffin wax sheets of the same dimensions.

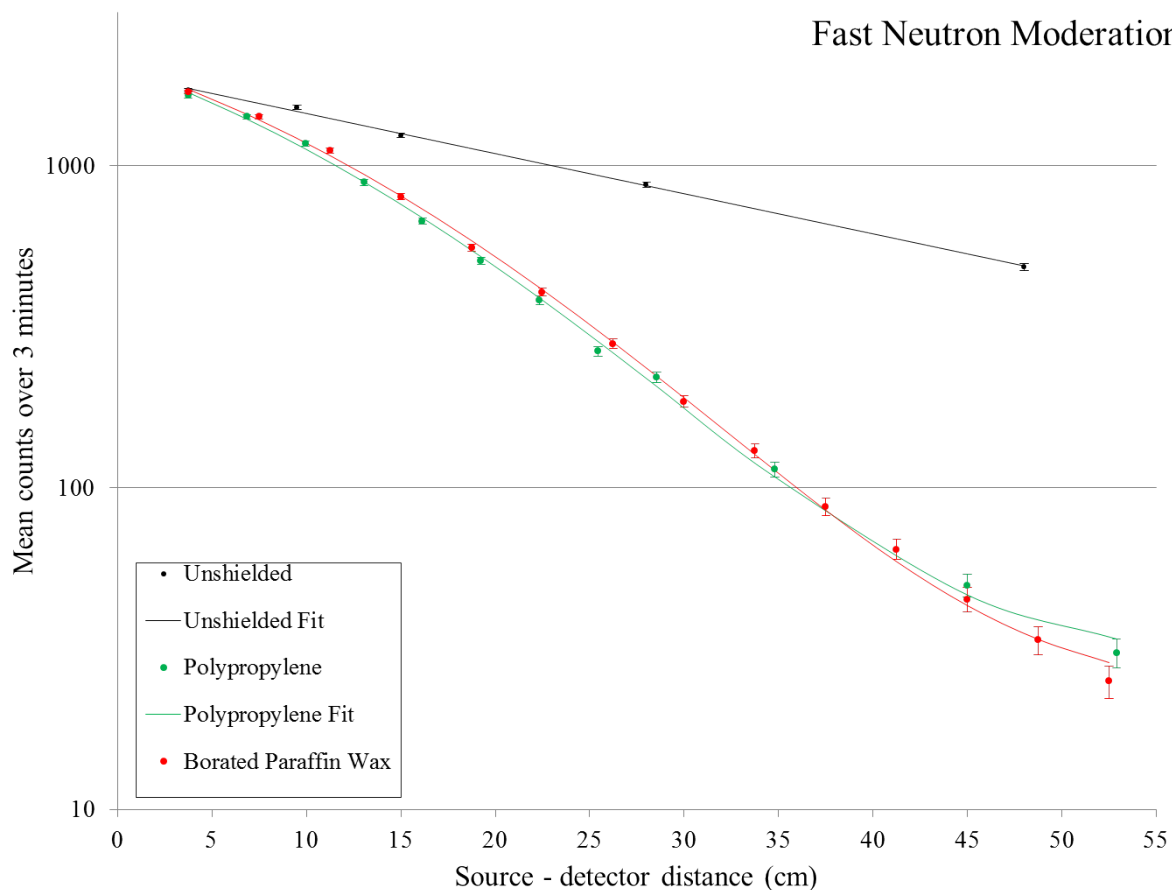


Figure 6.3: Plot showing the effects of the generator collimator on fast neutrons. The fits to the data are described in the text.

Figure 6.3 shows the neutron flux as a function of distance from the reaction chamber for an unshielded detector (black), polypropylene only shielding (green) and the borated

paraffin wax shield (red). The error bars represent the standard error on the mean.

For a point isotropic neutron source the flux at a distance r away is

$$f(r) = \frac{N}{4\pi r^2} \quad (6.1)$$

where N is the number of neutrons emitted per second.

The data for the unshielded flux did not show $1/r^2$ behaviour and instead were fitted to a simple exponential in the form of $y = a \times \exp(bx)$. A nonlinear least squares regression curve fitter [33] was used to generate the fit parameters $a = 1940 \pm 30$ and $b = -0.0287 \pm 0.0008 \text{ cm}^{-1}$ to produce the line for the unshielded flux depicted in figure 6.3. This form produced a good fit with an RMS error of 1.57. The data was also fitted with a constant background c , but the value of the background was not well constrained and was consistent with zero.

The geometrical attenuation equation (6.1) assumes a point source, emitting monoenergetic neutrons, in an infinite vacuum. These were not the conditions under which our experiment was undertaken. The neutron generator is not a point source, nor is it monoenergetic, as stated in Chapter 4, and the generator was already partially collimated in the concrete bulk shield and placed inside a concrete room. The presence of the bulk material would inevitably lead to scattered neutrons emerging from the surroundings with enough kinetic energy to register in the detector. The fact that the flux fits well to an exponential and not to the form of equation 6.1 is evidence that a detailed simulation would be needed to understand fully how neutrons are attenuated in this geometry. However, for the present purpose of optimizing the shielding, a good empirical fit to the data, as provided by the exponential, is all that is necessary.

The addition of polypropylene and borated wax meant that as well as simple geometric attenuation and neutron scattering, the effect of the material attenuation had to be considered also. For a collimated parallel beam of neutrons in a homogeneous attenuating

medium, the number of emitted neutrons passing through a thickness of material x , without interaction, can be modelled on the equation

$$N(r) = Ne^{-\Sigma x} = Ne^{-\frac{x}{\lambda}} \quad (6.2)$$

where N is the number of incident neutrons and λ is the neutron mean free path in the medium [37].

When the shielding material was present, equation 6.1 is modified in order to account for this attenuation, and the neutron flux at distance x from the source now becomes¹

$$f(r) = \frac{N}{4\pi r^2} e^{-\frac{x}{\lambda}} \quad (6.3)$$

The contribution from equation 6.2 was evident when attempting to fit the polypropylene and borated wax data. Simply fitting the data to $y = a \times \exp(bx)$, or even $y = a \times \exp(bx) + c$, did not yield good enough results to account for the contribution from material attenuation with RMS errors of around 3.50 for in both cases. It can clearly be seen from the data shown in figure 6.3, that below 35 cm the trend is not linear and the slope becomes steeper with increasing material thickness. The exponent was therefore modified to include a quadratic term in an attempt to improve the quality of the fit.

The data was fitted to the form $y = a \times \exp(bx + cx^2) + d$ which yielded a much better result, with RMS errors of 1.62 for polypropylene and 1.31 for borated wax. The coefficients polypropylene were: $a = 2032 \pm 78$, $b = -0.049 \pm 0.006 \text{ cm}^{-1}$, $c = -0.0013 \pm -0.0003 \text{ cm}^{-2}$ and $d = 30 \pm 5$ and for borated wax were: $a = 2058 \pm 61$, $b = -0.045 \pm 0.005 \text{ cm}^{-1}$, $c = -0.0013 \pm -0.0002 \text{ cm}^{-2}$ and $d = 23 \pm 3.4$. The d terms represent a constant background (in counts), presumably arising from neutron scattering in the room, which was present during every experimental run. The magnitude of the backgrounds were

¹ x is the as same distance r from equation 6.1, but the medium has changed and therefore the distance term has been changed to account for this

consistent with each other; the fit to the unshielded data gave -55 ± 168 counts, which is not significant but not in disagreement.

The data was re-plotted to highlight the effectiveness of the shielding materials at stopping fast neutrons compared to the unshielded flux. This is shown in figure 6.4.

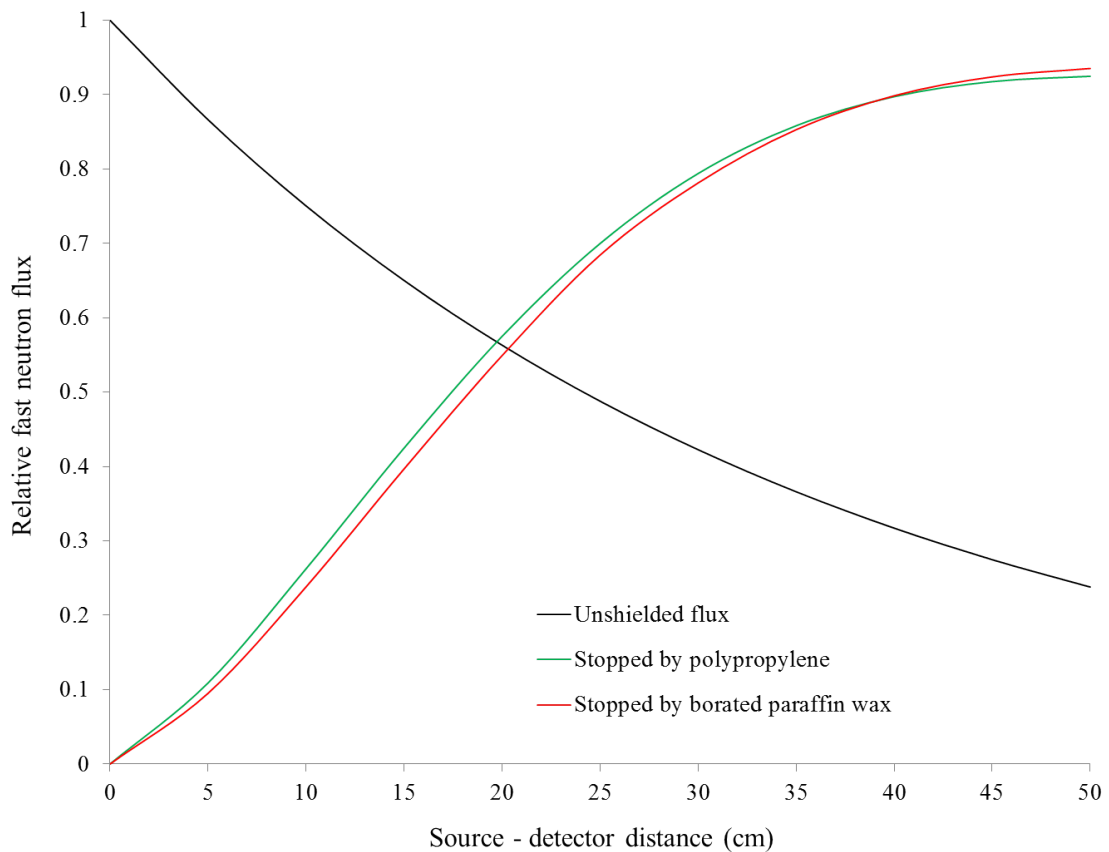


Figure 6.4: *Comparison between unshielded neutron flux and relative stopping power of shielding materials*

The fits were normalized to 1 at $x = 0$. The relative flux for the unshielded data is thus simply $y = \exp(bx)$, and the fraction of flux stopped by the shielding material is $\left(1 - \frac{y(\text{shielded})}{y(\text{unshielded})}\right)$. There is little difference in the effectiveness of either polypropylene or borated wax at moderating fast neutrons. However, the shielding must also protect the detectors from thermal neutrons, and this is the regime in which boron is expected to be advantageous.

Thermal Neutrons

Once the fast neutrons have been moderated to thermal (low) energies there should be a diffuse cloud of thermal neutrons in the room. Some of the thermal neutrons will capture on the hydrogen content of the collimator producing 2.2 MeV gamma rays. This is not a desirable scenario as it could distort the spectrum significantly by adding to the gamma background. However, the boron content of the paraffin wax should act as a thermal neutron “sponge” to mop up some of the thermal flux and reduce the probability of hydrogen capture. Neutron capture on boron will also prevent the thermal flux from reaching the detector arrays and interacting with the crystals.

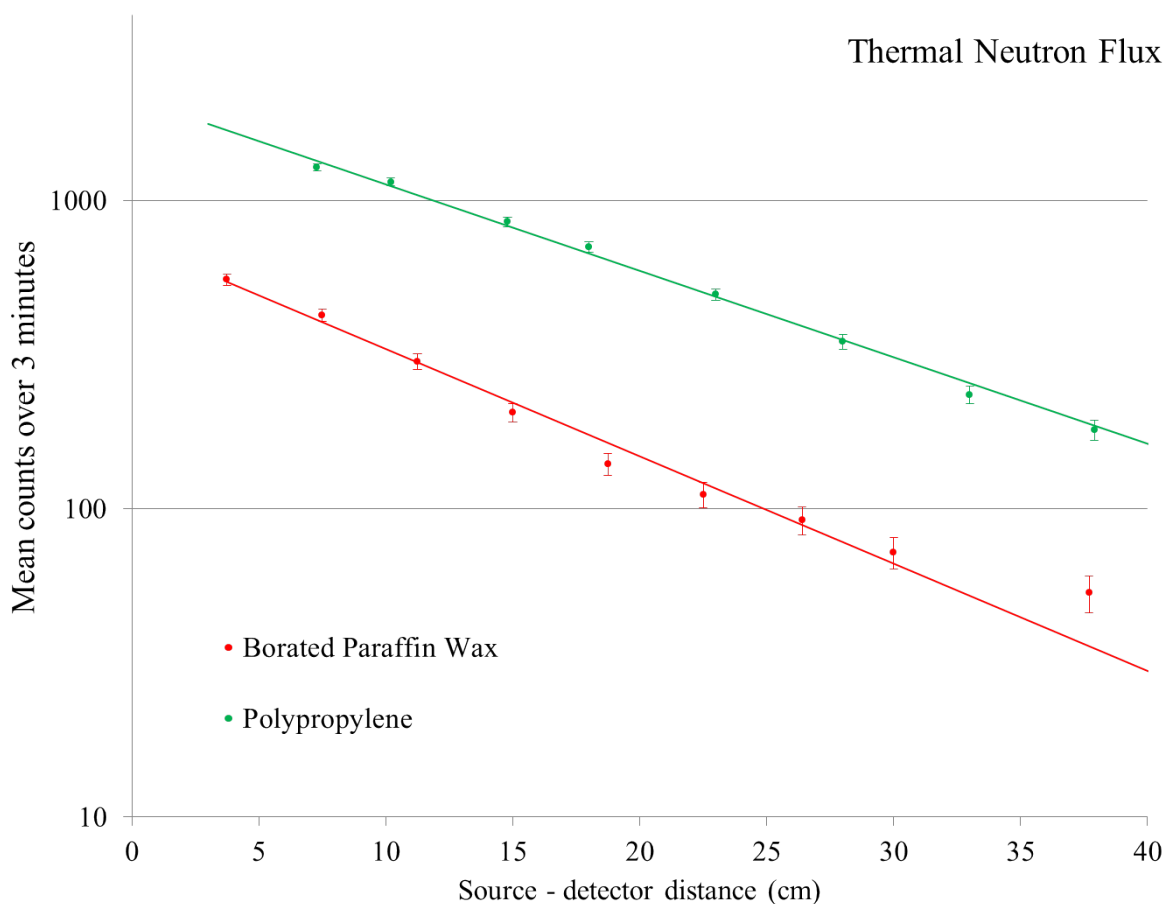


Figure 6.5: Plot showing the effects of the generator collimator on thermal neutrons.

Figure 6.5 shows the reduction in thermal flux as a function of moderator thickness for both polypropylene and borated paraffin wax. Unlike the shielded data for fast neutrons,

the behaviour of thermal flux could be fitted to a simple exponential of the form $y = a \times \exp(bx)$. The data was also fitted with a constant background c , but the value of the background was again not well constrained and consistent with zero. The fit parameters were $a = 2152 \pm 86$ and $b = -0.0646 \pm 0.0024 \text{ cm}^{-1}$, with an RMS error of 1.30 for polypropylene, and $a = 735 \pm 43$, $b = -0.0802 \pm 0.0040 \text{ cm}^{-1}$ and an RMS error of 1.41 for borated paraffin wax. There is some evidence for a background flux in the borated wax data, but not enough to justify a more complicated fit

6.3.1 Conclusion

The choice of shielding thickness requires a trade-off between reduced flux (caused by increased source to sample distance) and better collimation. As reduced flux can be offset by longer exposure, it was decided that better collimation was the more important factor.

From figure 6.4, it can be seen that there is little improvement in shielding of fast neutrons beyond 35 cm. This thickness of borated wax also reduces the thermal neutron rate to around 50 counts/3 min, comparable to the fast neutron rate (see figure 6.3). Therefore, this thickness was selected as the best choice for effective collimation.

6.4 Determining a suitable aperture width

The geometry of the collimator aperture was determined based on the proposed sample size for the initial experiment, which was a box of dimensions $18 \times 18 \times 25 \text{ cm}^3$. The width of the aperture at the sample would therefore be 18 cm. However, the neutron production region of the generator is not expected to be $\geq 18 \text{ cm}$ wide, so the effective collimator geometry should be conical in order to reduce the neutron background.

The exact geometry of the neutron production region is unknown, although it is assumed the generator resembles a bar source rather than a point, as stated in chapter 4. Therefore,

an estimate of the width of the source had to be made in order to construct the most efficient collimator possible. If the collimator aperture at the source was too narrow, fast neutrons would be lost through the sample due to scattering from the collimator itself. If it was too wide, the neutron background in the room would be increased and more shielding would be required around the detector arrays.

6.4.1 Experimental setup

A 33 cm high stack of borated paraffin wax was arranged with an initial aperture width of 30 cm, corresponding to ± 15 cm from the expected centre of the reaction chamber. The fast neutron button was placed on top of a lead shield and centred as shown in figure 6.6. The detector counted for a 3 minute acquisition, repeated over 5 runs. The mean and standard error on the mean were recorded.

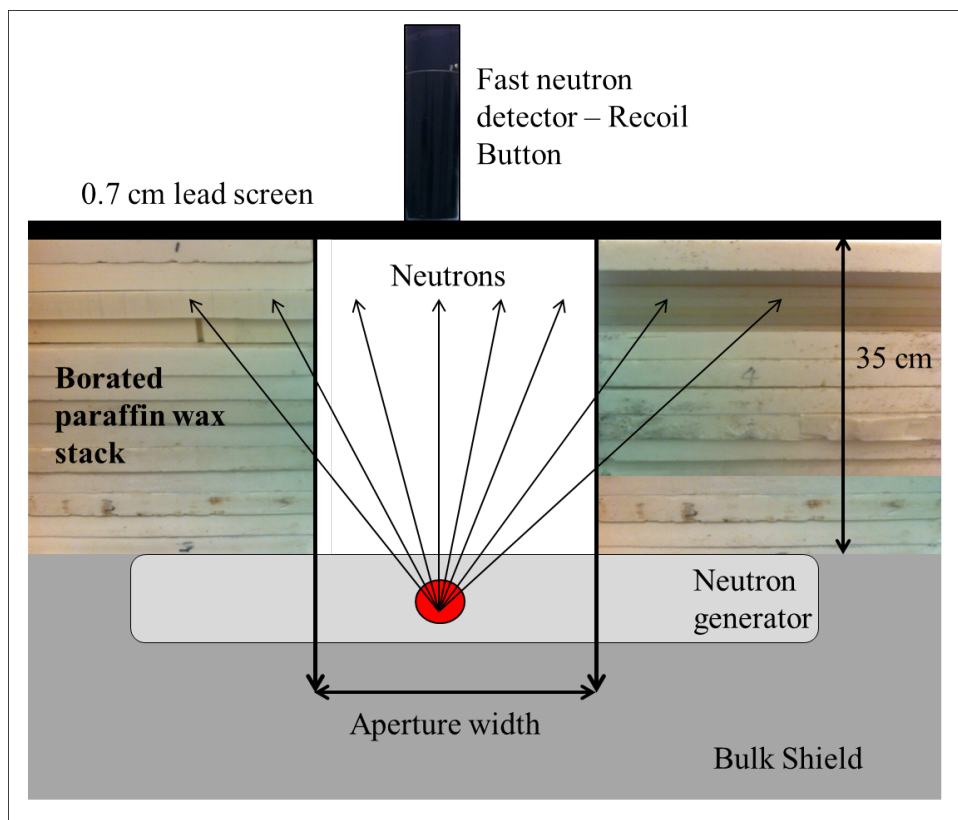


Figure 6.6: *Experimental setup for determination of the collimator aperture width*

The aperture width was then narrowed in increments of 2 cm (1 cm each side) until an aperture width of 5 cm was achieved, corresponding to the width of the fast neutron button. This was the limiting factor in the experiment given that a collimator aperture narrower than the detector width would interfere with the fast neutrons incident on the detector surface. Figure 6.7 shows the result.

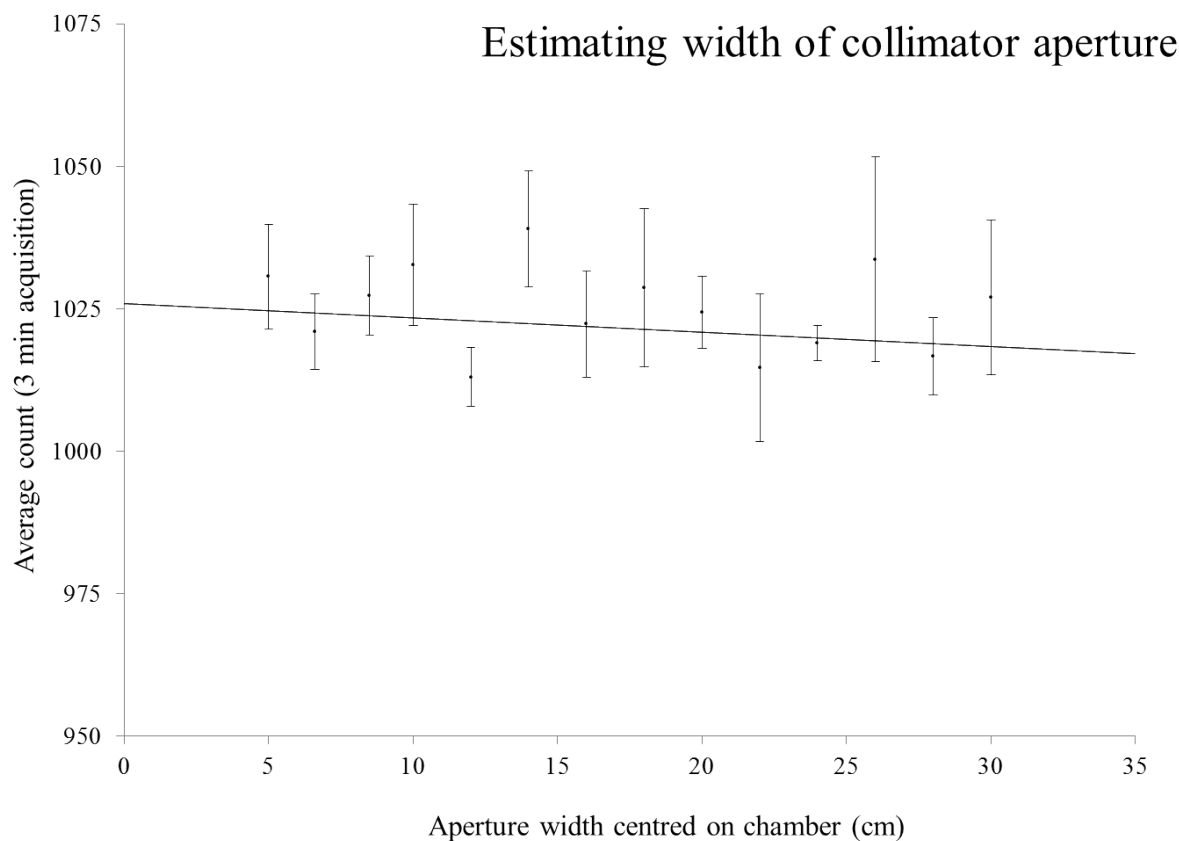


Figure 6.7: *Plot showing the number of counts as a function of aperture width. The detector was positioned directly above the centre of the neutron generator*

The data shows that for an aperture between 30 cm to 5 cm there is no significant difference in the number of counts recorded by the button, indicating that the bar source is not greater than 5 cm in width. The data in figure 6.7 was fitted to a straight line. The gradient was $-0.16 \pm 0.26 \text{ cm}^{-1}$, consistent with zero, and the y- intercept was 1024 ± 5 counts [33]. The magnitude of the standard errors are large. This is most likely due to small number statistics, and the variation in the total number of neutrons emitted by the generator per pulse.

6.5 Collimator Construction

In order to prevent the weight of the collimator and the lead shielding being placed on the NG chamber, a wooden frame to which mild steel plates could be bolted was constructed. At the aperture, angle iron was spot welded to the steel bottom to provide extra support. Figure 6.8 shows the base.

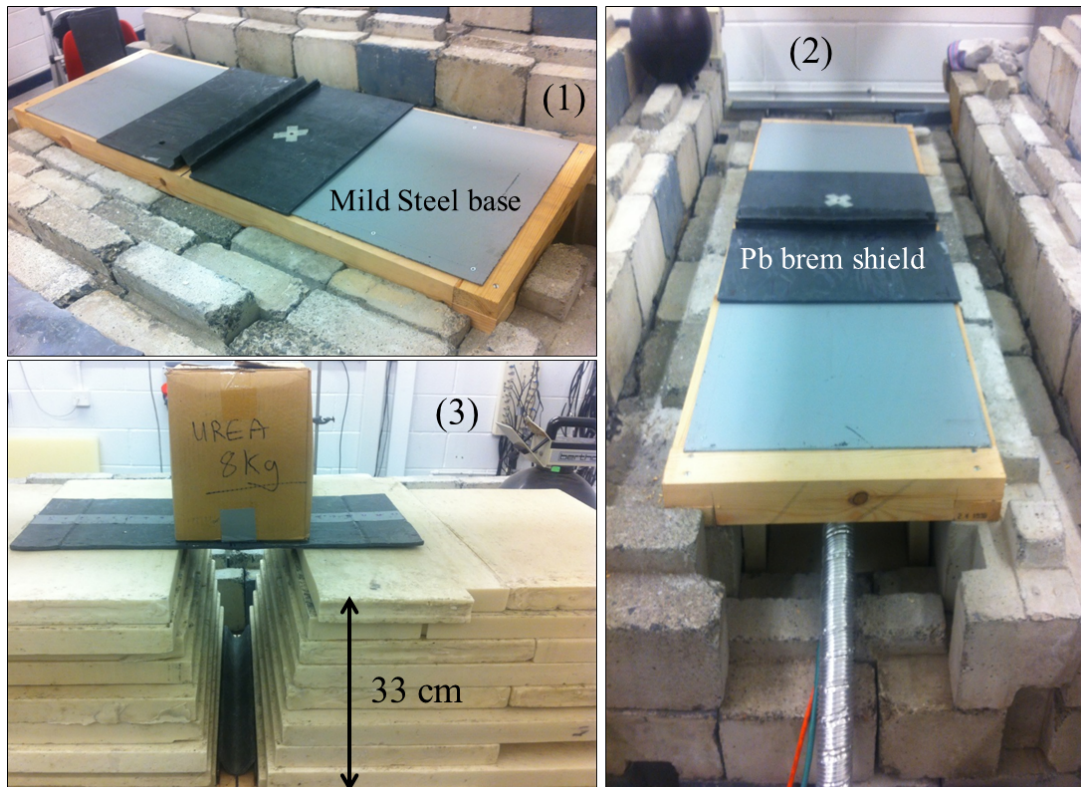


Figure 6.8: Construction of the collimator support (1) & (2). Finished collimator with sample in situ (3).

The frame is situated directly on the bulk collimator which will take the weight of the shielding. The mild steel plates were covered in 0.5 cm of lead flashing in order to attenuate the bremsstrahlung radiation emitted. The aperture was also covered with lead to stop bremsstrahlung radiation in the upward direction of the fast neutrons. Image (3) shows the borated paraffin wax stack and aperture opened up to a sample size of 18 cm, the setup for the initial sample interrogation experiments.

6.5.1 Collimator Measurement

The collimator was tested using a 33 cm stack and a 5 cm vertical aperture. Figure 6.9 shows the experimental setup. The fast neutron button was placed at the outer edge of the collimator, which corresponded to a distance of 30 cm from the neutron generator housing, at the location of the expected centre. A 3 minute count was repeated over 5 runs and a mean and standard error on the mean recorded.

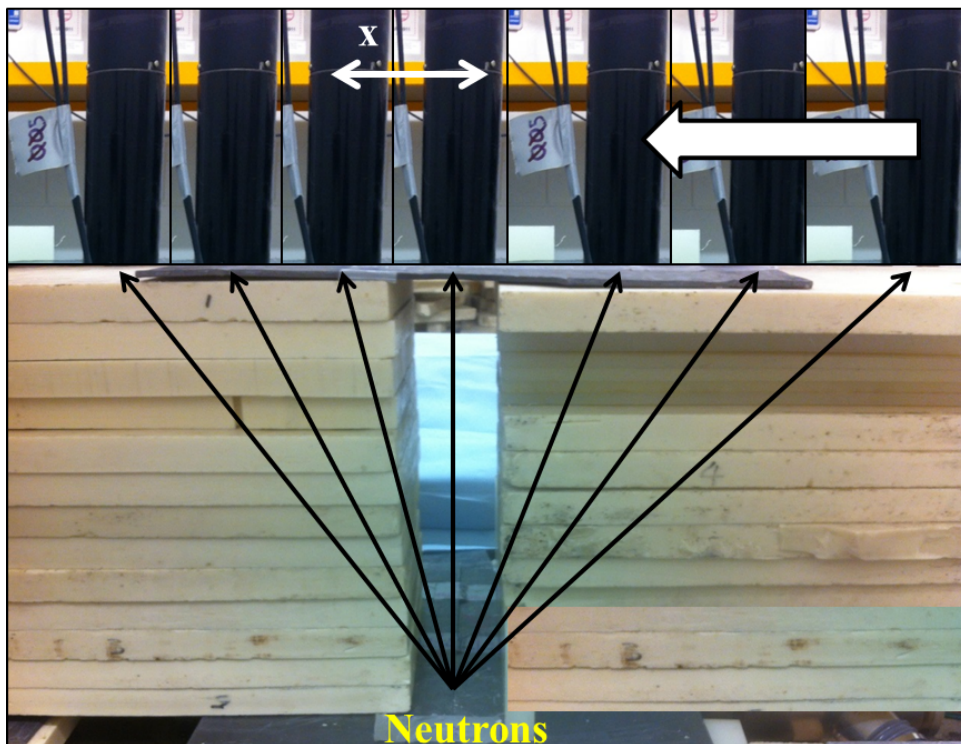


Figure 6.9: *Experimental setup to determine collimator effectiveness.*

The centre of the detector was initially placed 30 cm from the centre of the aperture, and then moved incrementally in steps of 1" (2.54 cm) horizontally toward the aperture. Once the leading edge of the button had reached the aperture edge, the increments were shortened to $\frac{1}{2}$ " (1.27 cm) until the detector had completely passed over. The detector was again moved horizontally away from the aperture towards the other end in increments of 1", again to a distance of 30 cm.

The fit for an unshielded flux (section 6.3) was used to calculate a reference value at each detector position x , defined as the horizontal offset of the detector centre from the aperture centre. This was then compared to the empirical flux as shown in figure 6.10.

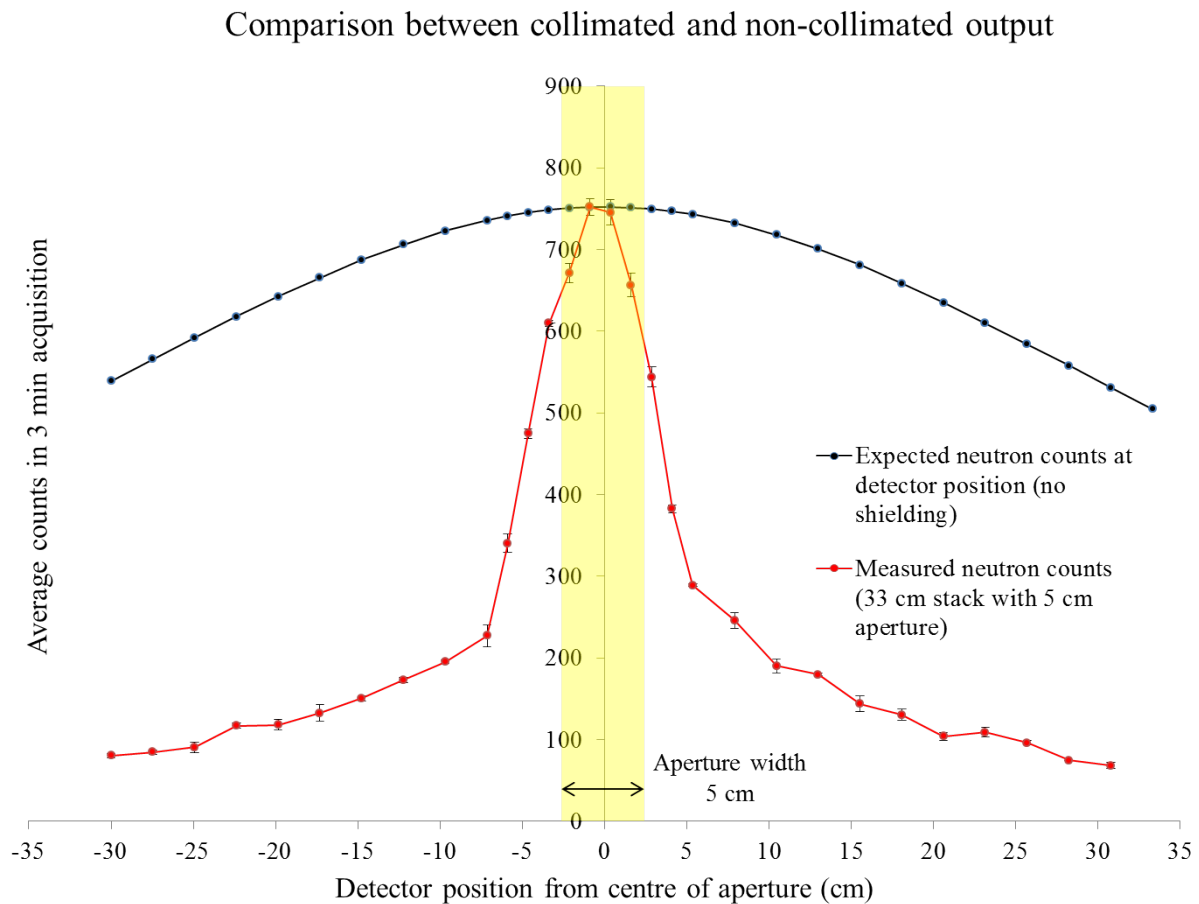


Figure 6.10: Plot showing the effectiveness of a vertical 5cm aperture collimator against generator fast neutrons.

The curve shows that when the detector is positioned directly over the collimator aperture, the number of neutrons passing through the detector resembles that of the unshielded flux. Also, when the detector is located away from the aperture, the flux drops as expected.

The width of the distribution is dependent on the diameter of the fast neutron button and the neutron background. The broadening across at the aperture appears as a result of the detector being partially obscured as it is moved incrementally across.

Because the detector diameter equals the aperture width, only when the button is directly

over the aperture centre should the count correspond to that of the unshielded flux. This is not the case as the data shows the maximum is positioned approximately 0.6 cm to the left. Given the uncertainty in the exact location of the region of neutron production, this was taken as the expected centre and the final collimator was centred on this position.

6.6 Conclusion

The bulk collimator was constructed and based around the dimensions of the neutron generator. The pulse transformer and cooling fan are also shown in figure 6.11.

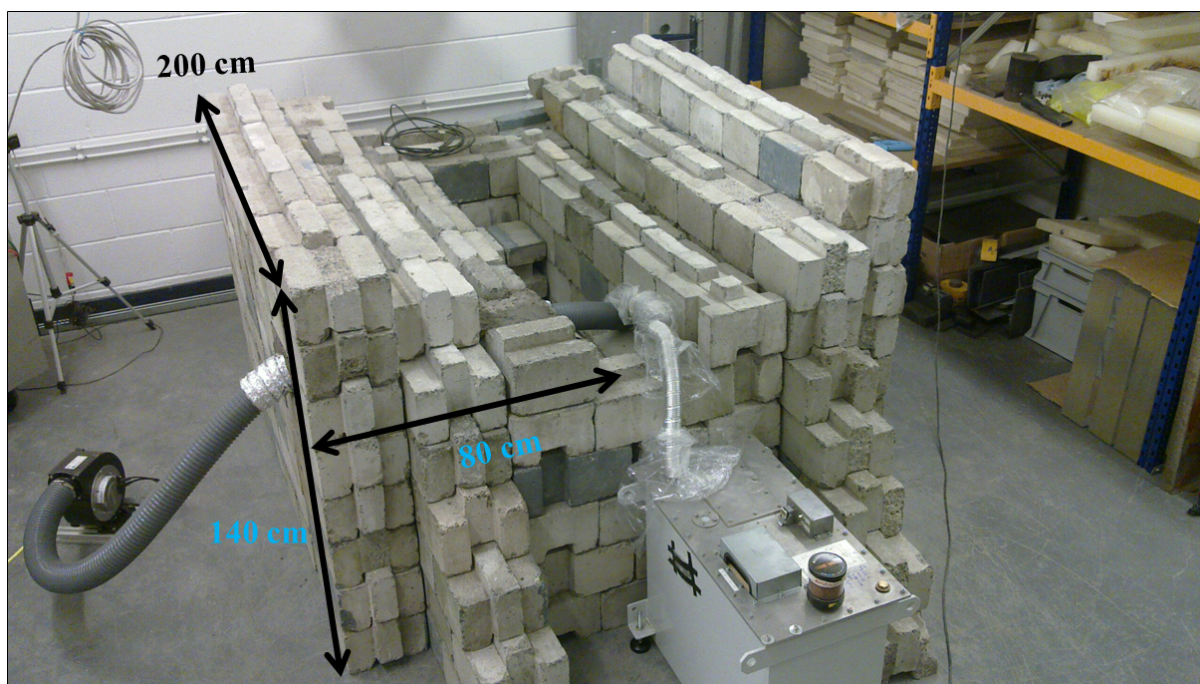


Figure 6.11: *Magnetite concrete block bulk shield.*

The generator itself was positioned in the centre supported by a wooden arch, which can be seen in figure ?? and surrounded by borated paraffin wax.

Finally, the collimator support shown in figure 6.12 and borated paraffin wax sheets were positioned on top.

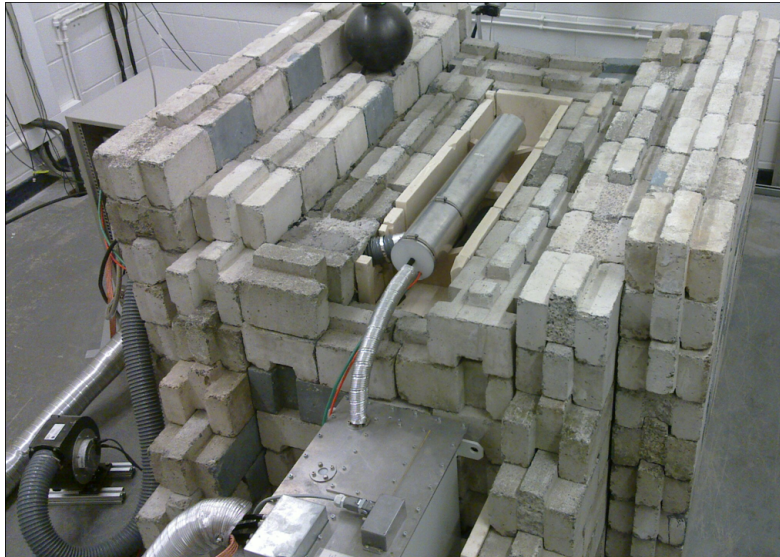


Figure 6.12: *Generator in situ.*

From the results of the materials testing, the dimensions of the beam port were 33 cm in height with an aperture width of 5 cm at the chamber wall and a width of 18 cm at the sample. This is shown in figure 6.13.

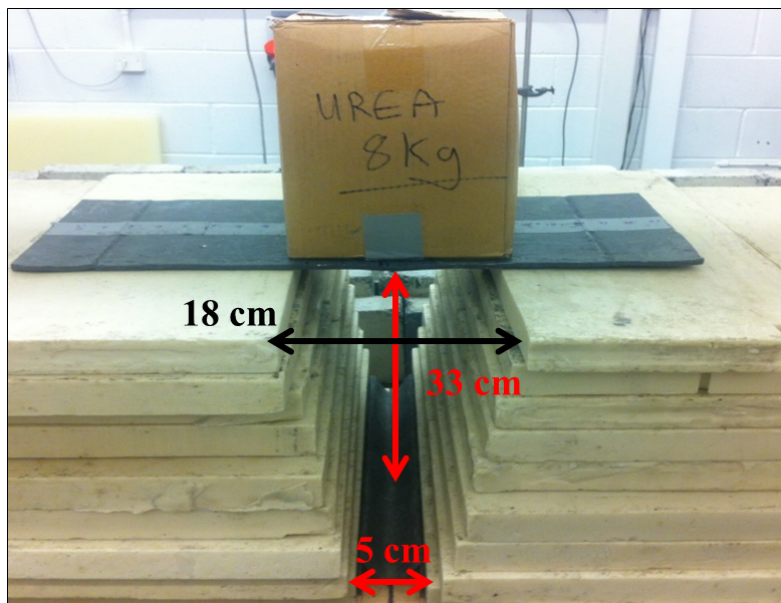


Figure 6.13: *Final collimator construction with sample in situ*

For an 18 cm wide sample, the neutron flux passing through the bottom face shows around a 3% deviation from the maximum value at the centre of the aperture. However the flux will drop by a factor of 2 by the time it's reached the sample top.

The collimator was constructed of materials which were readily available at the facility, cheap to build and safe to handle. This meant that the collimator geometry could be changed easily and quickly to suit a variety of sample geometries.

As this is a simple collimator, there are other materials and design considerations which could be taken into account to improve the effectiveness of the collimator. These will be discussed briefly in Chapter 9

Chapter 7

Estimating the Neutron Yield Using Fast Neutron Activation Analysis (FNA)

7.1 Introduction

This chapter describes the theory, experimental methodology and results regarding an estimation for the neutron yield of the generator. The related theory in terms of neutron and gamma interactions with matter is covered in chapter 2.

There are several factors which can affect the magnitude of the neutron yield, set out in chapter 4, and therefore the generator yield will have a tendency to fluctuate over time. Although these factors have been addressed and specific parameters can be adjusted to optimize performance, an “experimental standard” needs to be established for which the yield can be evaluated at any given time.

Being able to estimate a true yield is vital to understanding the observed signals emanating from a material under interrogation. Knowledge of the generator output charac-

teristics combined with nuclear cross-sections and target material properties means that the level of signal generation induced in a given phantom threat object can be estimated and compared to experimental data.

7.2 Activation Materials

The selection of the activation materials was based on several factors, namely:

- type of reaction product and the feasibility of detection;
- the cross-section for interaction with fast neutrons;
- half-life of the relevant reaction;
- availability of appropriate materials.

The first three points go hand-in-hand. The material must have a reaction that can be initiated with up to 14 MeV neutrons for which the cross-section is of reasonable magnitude. The activated nucleus must then subsequently decay via an exit channel which provides a suitable secondary radiation for detection. It must also have a half-life that is appropriate for the laboratory conditions, long enough to enable transportation between the generator room and counting setup without an appreciable decay of the activated isotope, but short enough that a significant level of activity can be induced in a realistic time frame. Finally, the sample material must be obtainable at reasonable cost and without need for isotopic enrichment.

There are a number of materials that can be used as threshold activation detectors with half-lives ranging from seconds to several days, but few have half-lives of suitable duration for the current experimental arrangement. The two most promising materials are aluminium and copper which have half-lives of around 10 minutes, making the irradiation and counting procedure possible in a reasonably short turnaround time and the repeat experiments feasible.

7.2.1 The $^{27}\text{Al}(n, p)^{27}\text{Mg}$ Reaction

Elemental aluminium is composed exclusively of ^{27}Al . There are two reactions with appreciable cross sections, appropriate thresholds and suitable decay products. The first is the $^{27}\text{Al}(n, \alpha)^{24}\text{Na}$ reaction with a cross section of around 0.1 barns, a threshold of 4.9 MeV and an E_γ of 1.37 MeV, which can be observed from the β^- decay of ^{24}Na to the 2+ excited state of ^{24}Mg . However, with a half-life of 15 hours this reaction is disfavoured due to the long count time required to produce a significant decay curve.

The second reaction is the $^{27}\text{Al}(n, p)^{27}\text{Mg}$ with a cross section of 0.07 barns and two gamma lines at 0.84 MeV and 1.01 MeV from the β^- decay of ^{27}Mg to the +1/2 (branching ratio $\epsilon_B = 71\%$) and +3/2 ($\epsilon_B = 29\%$) excited states of ^{27}Al respectively. The threshold for this reaction is around 2.2 MeV, making it a possible activation material for measuring the combined DD/DT yield. However, at 2.2 MeV the cross-section is very low (10^{-6} barns) and does not become measurable until around 3.8 MeV, where it is around 10^{-2} barns. The half-life for this reaction is 9.46 minutes, and is appropriate for our setup, being long enough to avoid significant loss of gamma intensity during the transport time from the generator to the counting room.

The cross-section as a function of neutron energy for the two reactions is shown in figure 7.1. The neutron energies associated with the NG output have been labelled for convenience.

7.2.2 The $^{63}\text{Cu}(n, 2n)^{62}\text{Cu}$ Reaction

Naturally occurring copper is composed of two isotopes, ^{63}Cu and ^{65}Cu , with isotopic abundances of 69.1% and 30.9% respectively. The preferred isotope for 14 MeV activation is ^{63}Cu which has an (n, 2n) reaction with a cross-section of 0.5 barns and a threshold of 11.9 MeV. The (n, 2n) reaction produces a residual nucleus of ^{62}Cu which decays by electron capture to ^{62}Ni with a half-life of 9.80 minutes. This decay time is suitable for

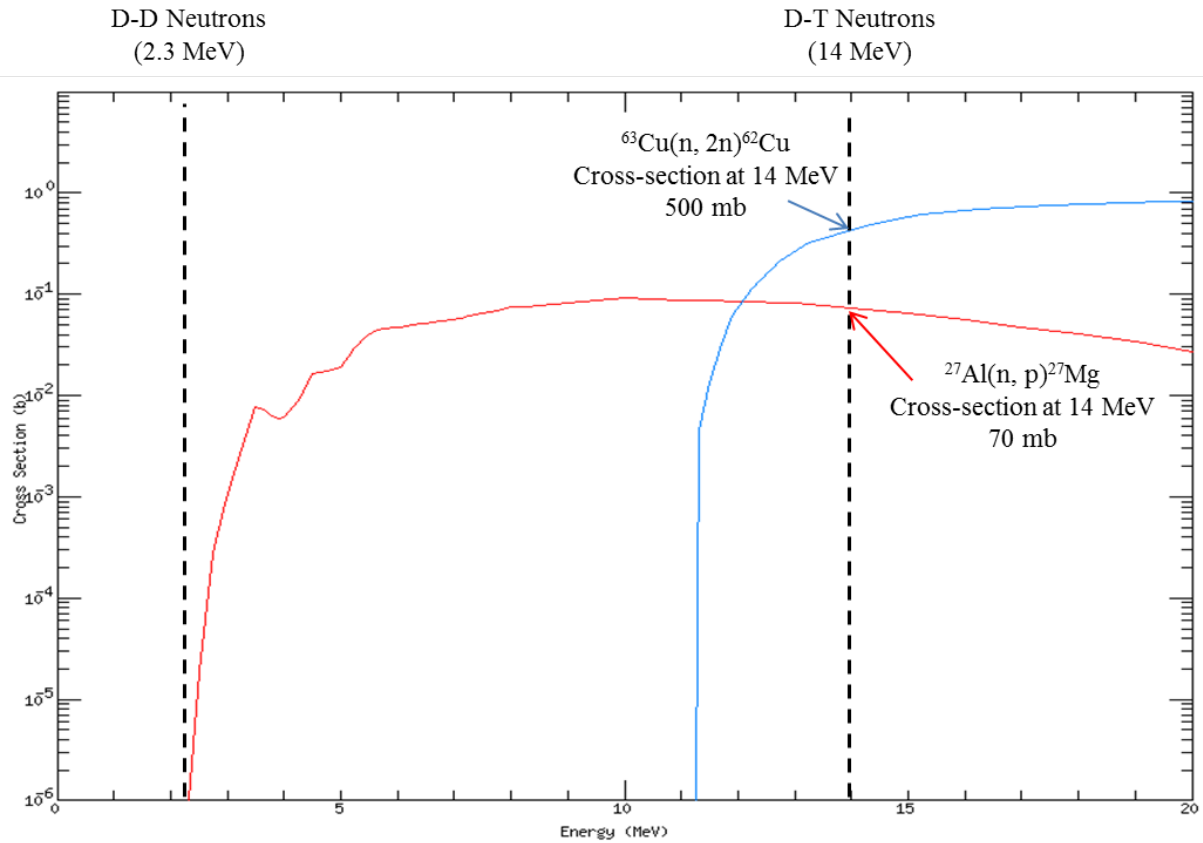


Figure 7.1: *Cross-section as a function of neutron energy for isotopes of aluminium and copper*

the laboratory setup.

The positrons annihilate with free electrons in the sample and surrounding materials, and the 511 keV gamma-rays are counted. ^{65}Cu also has a cross section of a similar magnitude for an (n, 2n) reaction with a marginally lower threshold of 10.7 MeV, the residual ^{64}Cu nucleus decays by positron emission to ^{64}Ni ($\epsilon_{\text{R}} = 61\%$). However, the half-life for this particular decay mode is of the order 12.7 h, meaning that an extremely long count duration would have to be performed in order to make a suitable measurement.

Given that both isotopes will be activated during irradiation, a correction will need to be made to the yield calculation in order to separate the ^{65}Cu component from the ^{63}Cu . This will be explained in section 7.3.2.

7.3 The Yield Equation

7.3.1 Derivation of the Yield Equation

When a sample is placed in a neutron flux, the rate R at which activation occurs is

$$R = \phi \Sigma_{act} V, \quad (7.1)$$

where ϕ is the neutron flux averaged over the surface of the sample, Σ_{act} is the macroscopic cross section averaged over the neutron energy spectrum and V is the sample volume.

The macroscopic cross section, Σ_{act} , is given by

$$\Sigma_{act} = n\sigma(E)$$

where n is the number density, and $\sigma(E)$ is the energy dependent microscopic cross section for the reaction of interest. The number density can be calculated from

$$n = \frac{N_A \epsilon_A \rho}{A_W}$$

where N_A is Avagadro's constant, ϵ_A is the fractional abundance of the isotope in the sample, ρ is the density of the sample and A_W is the mass number. The macroscopic cross section is therefore

$$\Sigma_{act} = \frac{\epsilon_A N_A \rho \sigma(E)}{A_W}$$

Writing $\rho = M/V$ and substituting Σ_{act} into (7.1) gives

$$R = \frac{\phi \epsilon_A N_A M \sigma(E)}{A_W}. \quad (7.2)$$

When a material is placed in a flux of neutrons, the number of radioactive nuclei N induced in time t is calculated from the difference between the rate of formation and the

subsequent rate of decay

$$\frac{dN}{dt} = R - \lambda N$$

where R is the rate of activation and $-\lambda N$ is the rate of decay. Solving this first order differential equation for the condition $N(0) = 0$ we obtain the result

$$N(t) = \frac{R}{\lambda}(1 - e^{-\lambda t}). \quad (7.3)$$

Because activity A is defined as λN , equation 7.3 can be written as

$$A(t) = R(1 - e^{-\lambda t}). \quad (7.4)$$

Figure 7.2 shows the buildup of activity of a sample after insertion in a neutron flux. The half-life for the reaction of interest will determine the time for which the sample needs to be irradiated in order to approach a saturation value, at which point the rate of formation and the rate of decay reach equilibrium and no further gain in the induced activity can be achieved.

This saturated activity is denoted A_∞ ; setting $t = \infty$ in equation 7.4 gives $A_\infty = R$. The activity of a sample removed after an irradiation time t is therefore

$$A_0 = A_\infty(1 - e^{-\lambda t_0}). \quad (7.5)$$

Substituting equation 7.2 into equation 7.5 gives

$$A_0 = R(1 - e^{-\lambda t_0}) = \frac{\phi \epsilon_A N_A M \sigma(E)}{A_W} (1 - e^{-\lambda t_0}). \quad (7.6)$$

From the decay curve shown in figure 7.2 we can calculate the number of events recorded

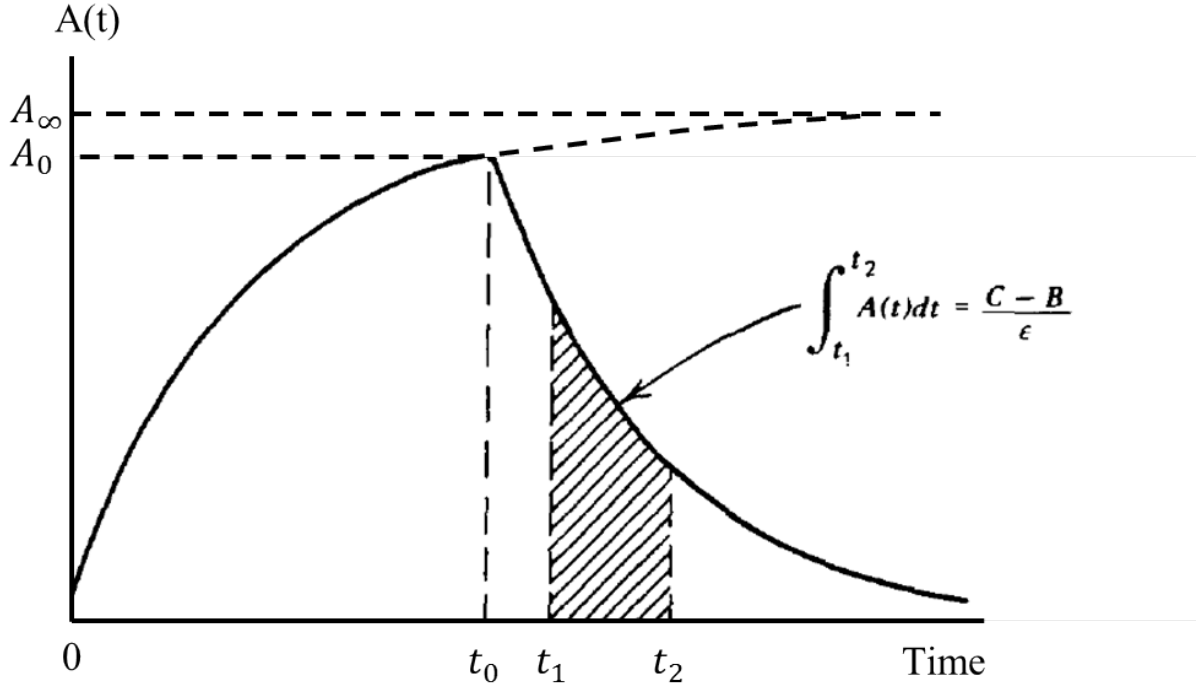


Figure 7.2: Buildup and decay of the induced activity of a sample. Exposure to a neutron flux begins at $t = 0$, the sample is removed from the neutron flux at time t_0 and counting takes place between t_1 and t_2 . [22]

between any given time periods t_1 and t_2 from

$$C = \epsilon_D \int_{t_1}^{t_2} A(t) dt + B \quad (7.7)$$

where ϵ_D is the detector counting efficiency, $A(t)$ is the induced activity after the irradiation time t_0 , and B is the background counts in $t_1 - t_2$.

After the end of irradiation, the number of activated nuclei decreases by the usual law of radioactive decay

$$A(t) = A_0 e^{-\lambda t} \quad (7.8)$$

Substituting A_0 into the above from equation 7.6 and then $A(t)$ into 7.7 we get

$$C = \epsilon_D R (1 - e^{-\lambda t_0}) \int_{t_1}^{t_2} e^{-\lambda t} dt + B \quad (7.9)$$

Performing the integration we have

$$C = \frac{\epsilon_D R}{\lambda} (1 - e^{-\lambda t_0}) (e^{-\lambda t_1} - e^{-\lambda t_2}) + B \quad (7.10)$$

where t_1 and t_2 are the arbitrary times from the decay curve shown in figure 7.2. If we now substitute in our equation for R back into the above we obtain

$$C = \frac{\phi \epsilon_D \epsilon_A \epsilon_B \epsilon_S M N_A \sigma(E)}{\lambda A_W} (1 - e^{-\lambda t_0}) (e^{-\lambda t_1} - e^{-\lambda t_2}) + B. \quad (7.11)$$

Next, we can define a total neutron yield as

$$Y = \phi t_0 4\pi d^2 \quad (7.12)$$

where $4\pi d^2$ is the surface area of the sphere of radius d (distance to the centre of the sample from the centre of the neutron source), t_0 is the irradiation time and ϕ is neutron flux averaged over the foil surface.

Finally, rearranging equation 7.11 to make the neutron flux the subject gives

$$\phi = \frac{(C - B)\lambda A_W}{\epsilon_A \epsilon_D M N_A \sigma(E) (1 - e^{-\lambda t_0}) (e^{-\lambda t_1} - e^{-\lambda t_2})}. \quad (7.13)$$

We can estimate the generator yield from

$$Y = \frac{4\pi d^2 (C - B)\lambda A_W t_0}{\epsilon_A \epsilon_D M N_A \sigma(E) (1 - e^{-\lambda t_0}) (e^{-\lambda t_1} - e^{-\lambda t_2})}. \quad (7.14)$$

To clean up the equation we can group the terms which are related to the properties of the specific sample material and the counting setup by defining a parameter X which

includes a new variable ϵ_s , the branching ratio for the specific decay channel.

$$X = \frac{\epsilon_A \epsilon_D \epsilon_B N_A \sigma(E)}{A_W} \quad (7.15)$$

Thus, the final yield equation now becomes

$$Y = \frac{4\pi d^2 (C - B) \lambda A_W t_0}{X M (1 - e^{-\lambda t_0}) (e^{-\lambda t_1} - e^{-\lambda t_2})} \quad (7.16)$$

which gives the total number of neutrons emitted over the irradiation time by the neutron generator. Therefore, using $\frac{Y}{t_0}$ will give the yield in neutrons per second, and $\frac{Y}{t_0 \times f_p}$, where f_p is the pulse frequency, gives the number of neutrons per pulse.

7.3.2 Corrections to the Yield Equation

Detector Efficiency

The X-term is a simple factor which takes into consideration the properties of both the counting system and the sample material. The term contains two energy dependent variables, namely the neutron cross-section for the reaction of interest at 14 MeV and the detector counting efficiency for energy E_γ . The remaining terms are properties of the sample element and decay probabilities.

Because there are only two activation gamma-ray energies of interest (0.84 MeV for aluminium and 0.511 MeV for copper), we can modify ϵ_D in the X-term to an absolute detector efficiency for the counting geometry used, by using radioactive calibration sources with emissions of similar energy using

$$\epsilon_D = \frac{\text{Total number of events recorded in photopeak of energy } E_\gamma \text{ in time } t}{\text{Total number of quanta of energy } E_\gamma \text{ emitted by the source in time } t} \quad (7.17)$$

Equation 7.17 depends on several factors, namely the energy of the gamma-ray, the

counting geometry of the experimental setup, the quantum efficiency (QE) of both the detector crystal and the light collection device (photocathode QE), the level of attenuation in the source matrix, and the material surrounding the detector (i.e. detector housing and shielding materials). By calculating the efficiency with a detector top geometry we can generate this efficiency for the same conditions as the activation count

Copper Corrections

Figure 7.3 shows the gamma emission spectrum of copper sample 2 after a count time of 50 minutes following a 50 minute irradiation.

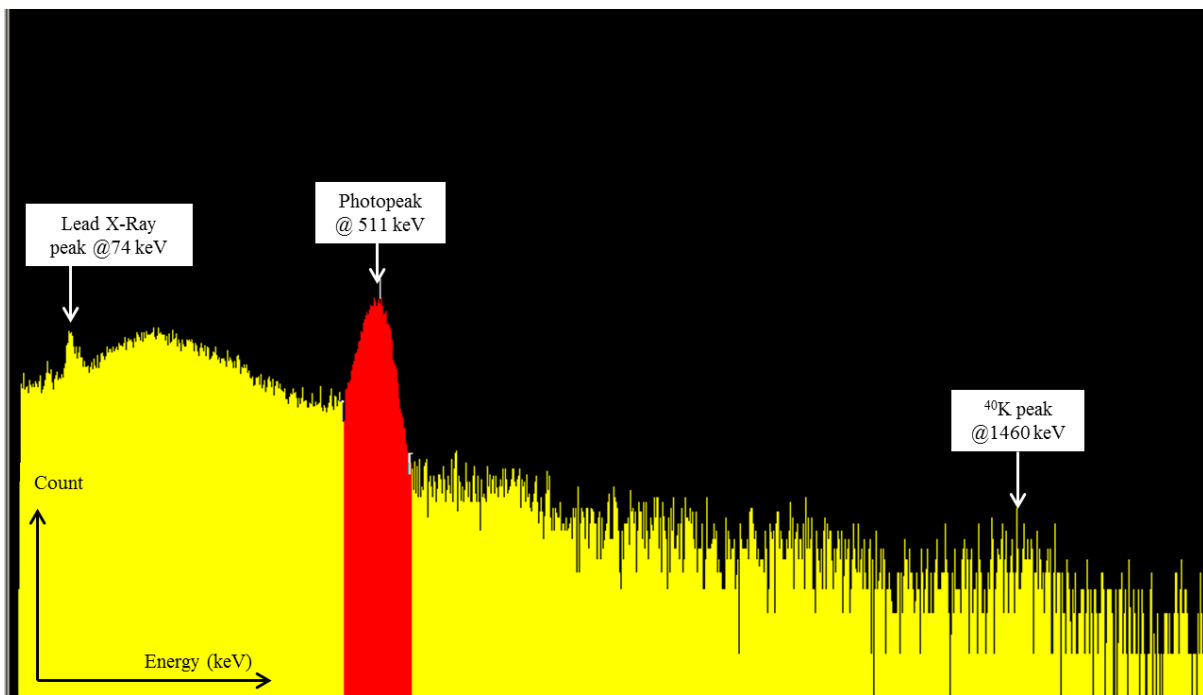


Figure 7.3: *Activation spectrum from Cu sample 2.*

The peak at 511 keV will include contributions from the decay of ⁶²Cu and ⁶⁴Cu and therefore only a certain percentage of the total peak area will originate from a particular isotope. By looking at the yield equation

$$Y = \frac{4\pi d^2(C - B)\lambda t_0}{XM(1 - e^{-\lambda t_0})(e^{-\lambda t_1} - e^{-\lambda t_2})} \quad (7.18)$$

and the X-term

$$X = \frac{\epsilon_A \epsilon_D \epsilon_B N_A \sigma(E)}{A_W} \quad (7.19)$$

it is clear that a correction needs to be made to the $(C - B)$ term in 7.18 in order to take into account the fractional abundance as stated in 7.19. Other terms in the equation which differ between isotopes are ϵ_B (the branching ratio of the decay mode), $\sigma(E)$ (the cross-section for the (n, 2n) reaction at 14 MeV) and λ (the decay constant, which is determined by the half-life). The rest of the terms in equations 7.18 and 7.19 are constants.

If we define a new term, α , which defines the fraction of $(C - B)$ that corresponds to each decay, we can separate the yield equation isotopically by stating that for ^{63}Cu and ^{65}Cu respectively

$$Y_{63} = \frac{4\pi d^2 \alpha (C - B) \lambda t_0}{X_{63} M (1 - e^{-\lambda t_0}) (e^{-\lambda t_1} - e^{-\lambda t_2})} \quad (7.20)$$

$$Y_{65} = \frac{4\pi d^2 (1 - \alpha) (C - B) \lambda t_0}{X_{65} M (1 - e^{-\lambda t_0}) (e^{-\lambda t_1} - e^{-\lambda t_2})} \quad (7.21)$$

It is now possible to equate the above given that the generator yield should be the same for both isotopes,

$$\frac{\alpha \lambda_{63}}{\sigma(E)_{63} (1 - e^{-\lambda_{63} t_0}) (e^{-\lambda_{63} t_1} - e^{-\lambda_{63} t_2})} = \frac{(1 - \alpha) \lambda_{65}}{\sigma(E)_{65} (1 - e^{-\lambda_{65} t_0}) (e^{-\lambda_{65} t_1} - e^{-\lambda_{65} t_2})} \quad (7.22)$$

This can be solved for α , the result being $\alpha = 92\%$, which corresponds to the fraction of the background subtracted peak area $(C - B)$ from the ^{63}Cu decay. This means that the contribution to the peak area from ^{64}Cu decay is just 8%, as expected for a much longer half-life.

7.4 Experimental Method

Estimating ϵ_D for the NaI(Tl) Scintillation Detector

It is possible to determine the absolute photopeak efficiency experimentally using radioactive materials of known activity. A set of $1\mu\text{Ci}$ (37 kBq) Canberra laboratory calibration sources were acquired containing ^{22}Na , ^{54}Mn , ^{60}Co , ^{133}Ba and ^{137}Cs isotopes which provided a gamma-ray energy range of 80 keV to 2505 keV¹. The sources ^{22}Na and ^{54}Mn produce gamma radiation of energy very close to the energies associated with the radioactive decay of the activated samples of ^{63}Cu and ^{27}Al respectively, namely the 511 keV positron annihilation peak associated with the copper samples, and a gamma of 835 keV (^{27}Al $E_\gamma = 847$ keV) for the aluminium. It was therefore possible to calculate ϵ_D experimentally for use in the yield equation. Figure 7.4 shows the decay schemes.

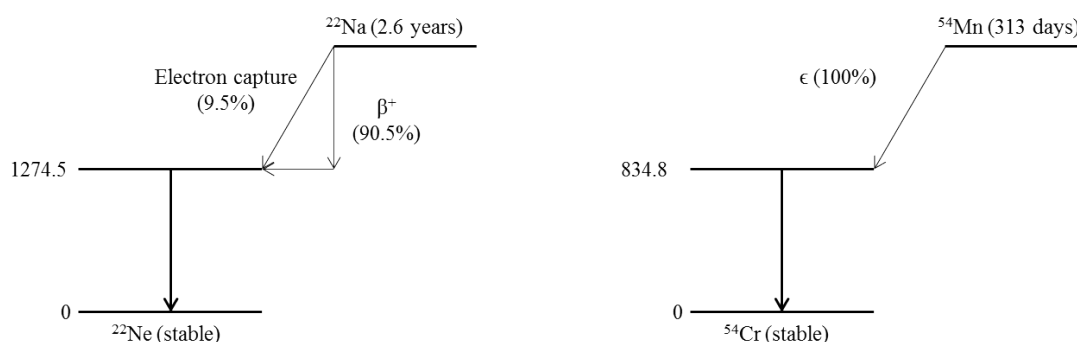


Figure 7.4: Decay scheme of ^{22}Na and ^{54}Mn

On the date of the experiment the sources were exactly 4 years old and the corrected activity could be estimated using the equation

$$A(t) = A_0 \exp(-\lambda t) \quad (7.23)$$

where A_0 is 37 kBq, λ is the decay constant and t is 4 years.

¹1173 keV and 1332 keV sum peak from ^{60}Co

From figure 7.4 (the ^{22}Na level diagram), the branching ratio for positron decay is 90.5%; only this fraction of decays will produce annihilation gamma-rays at 511 keV and so the activity of the source should be adjusted to take this into consideration. For ^{54}Mn , the 843 keV gamma is emitted in 100% of decays and no adjustment is needed.

The source was placed directly on the detector top to mimic the geometry associated with the counting of the activated samples, and a spectrum was produced over a 600 second period. Figure 7.5 shows the annihilation peak at 511 keV, where the peak limits were estimated using the “peak locate w/report” feature in the Canberra GENIE2000 MCA software [?].

The background subtracted peak area was taken and used in equation 7.17 along with the total number of 511 keV gamma-rays emitted by the source over the counting window. The absolute full-energy peak efficiency was found to be $2.03 \pm 0.14\%$.

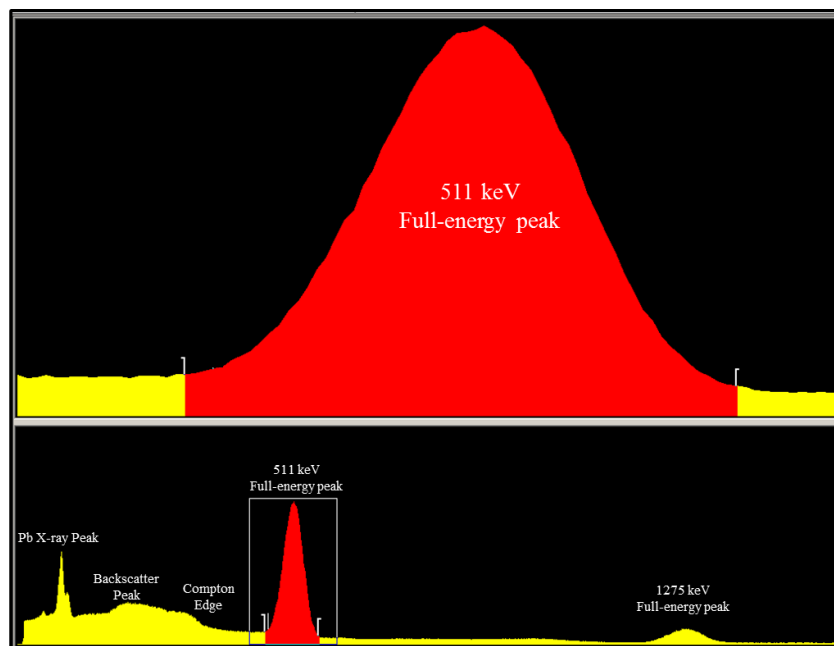


Figure 7.5: ^{22}Na spectrum highlighting the 511 keV annihilation peak and other key spectral features

The process was then repeated for the ^{54}Mn source. However, because the half-life of ^{54}Mn is much shorter than the half-life of ^{22}Na , the activity of the source was reduced

significantly relative to the ^{22}Na and therefore the acquisition time was increased to 30 minutes in order to obtain better counting statistics. The efficiency was measured at $8.02 \pm 0.29\%$. These values could then be inserted into the X-term as ϵ_D in equation 7.15.

7.4.1 The Copper and Aluminium Samples

The aluminium and copper samples were cylinders of 1 cm diameter and 1 cm thickness. Four samples of each material were taken from two different batches of copper and aluminium rods and polished. Figure 7.6 shows the samples.

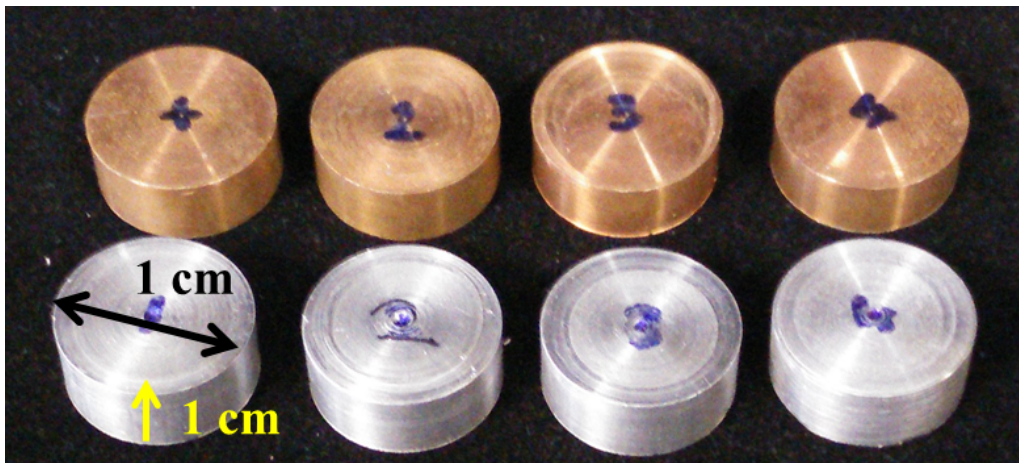


Figure 7.6: *Schematic of the reaction chamber*

The samples were labelled according to the element, sample number (1-4) and date of irradiation (e.g. ddmmyyCu1).

7.4.2 Sample Irradiation Geometry

The closest point at which the sample could be placed relative to the centre of the neutron production region was on the outer housing of the generator, the exact location determined using the data in figure 6.10.

Figure 7.7 shows a simple drawing of the setup with the sample location marked in red.

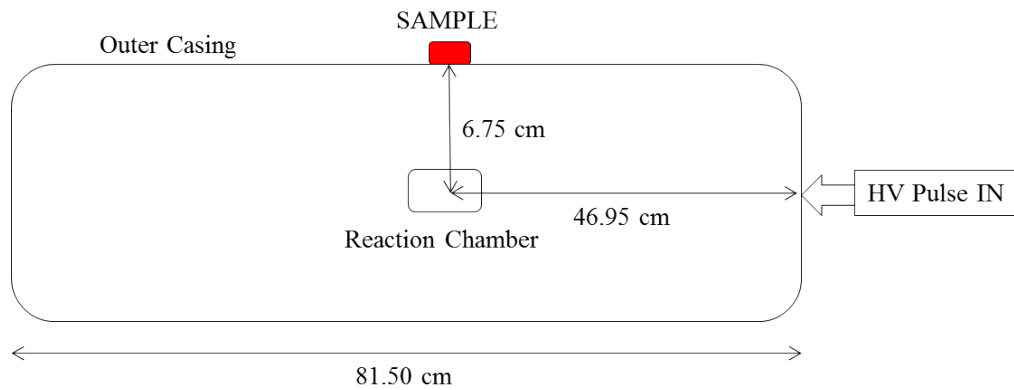


Figure 7.7: *Schematic of the reaction chamber*

As mentioned in chapter 4, the radius of the outer casing was approximately 6.75 cm and with the sample cylinder being 1 cm thick, the distance between the centre of the neutron production region and the centre of the sample was taken to be 7.25 ± 0.50 cm. This was used as the distance term d in equation 7.12.

The sample was positioned directly on the detector housing and irradiated for 1 hour. This was long enough to build up a satisfactory level of activation and approach saturation as shown in figure 7.2. At the end of the irradiation time the activated sample was transferred to the detector top of the NaI(Tl) detector located in the control room; the time duration of the move was recorded.

7.4.3 Experimental Method: The decay curve

The activation spectrum was saved at intervals of 3 minutes until 60 minutes had elapsed. Figure 7.8 gives a visual example of how the activation spectrum of a ^{63}Cu sample builds up over a period of time after irradiation.

Following the count the saved files were sequentially uploaded back into the software and the peak locate w/report sequence executed to identify the limits of the full-energy peaks.

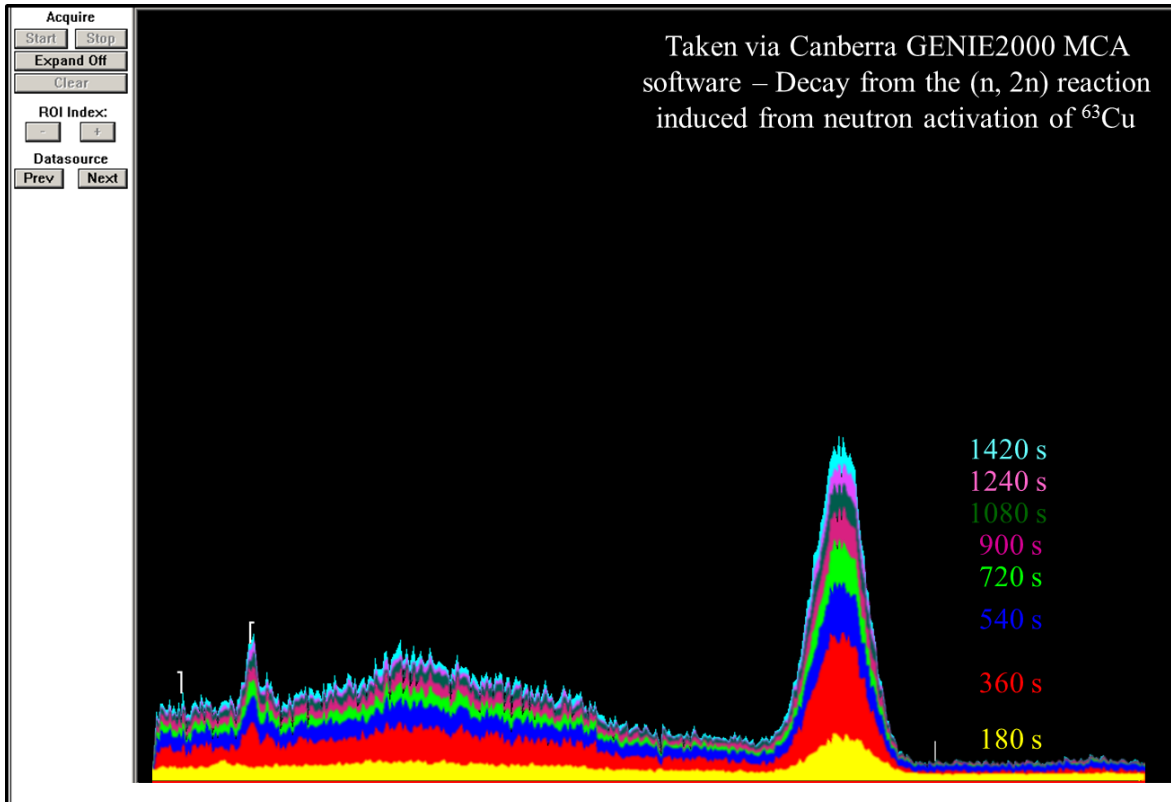


Figure 7.8: *Overlay of spectra produced over time from a neutron activated copper sample*

The nett area of the photopeak (integral area between the limits of the peak minus the background counts), was recorded at each time interval so that the reduction in sample activity could be plotted as a function of time.

The data was fitted to an exponential in the form $y = Ae^{-\lambda t}$, where the gradient λ is the decay constant. The decay constant can then be used to calculate the half-life of the activated isotope which can be compared to the expected value.

Finally, it was necessary to calculate the area under the curve between two arbitrary time intervals t_1 and t_2 , by subtracting the nett peak area of the spectrum corresponding to t_2 , from that obtained at t_1 .

This provides a value of $(C - B)$ shown on figure 7.2 which can be used in equation 7.16, along with the timing information t_1 , t_2 and t_0 .

7.4.4 The Yield Template

A spreadsheet for each activation material was created which would allow the calculation of the neutron yield from equation 7.16. Producing a template for each material meant that many of the terms in equation 7.16 could remain constant over the 4 samples and only certain variable terms to be inputted after the irradiation and count procedure, namely the counts in the peak area ($C - B$), corresponding to the time interval t_1 and t_2 , the irradiation time t_0 , and the sample mass².

7.5 Results: Aluminium Samples

Figure 7.9 shows an example of the spectrum produced from one of the activated samples. The full energy peak, shown in red, is at 0.849 ± 0.006 MeV according to the “peak locate” software, which is in good agreement with the expected value of 0.844 MeV. The second peak at 1.01 MeV is also visible.

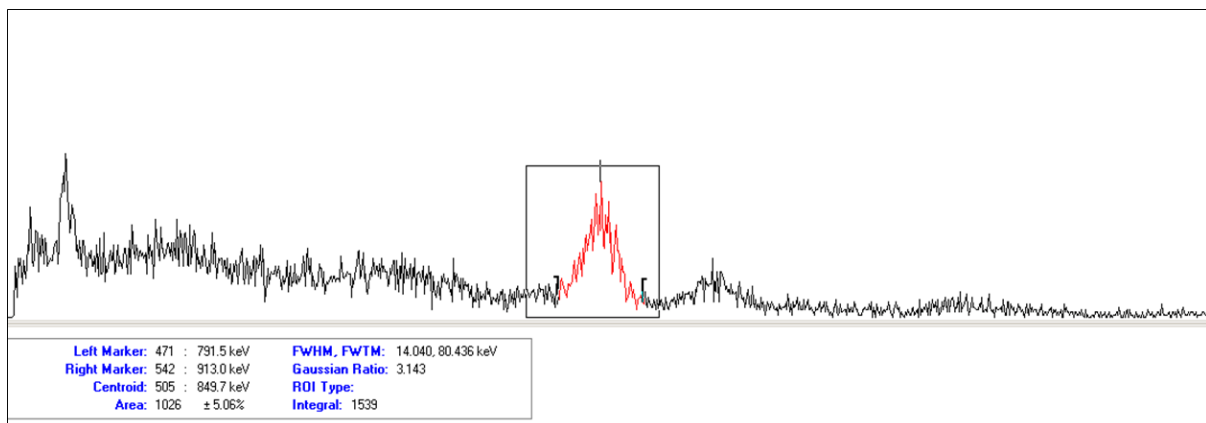


Figure 7.9: *Activation spectrum acquired from aluminium sample 190713Al2*

For each sample an arbitrary t_1 and t_2 were chosen and the counts in the full-energy peak recorded between those limits. The values of t_1 and t_2 were varied between samples.

²The sample dimensions had very small (but measurable) differences. Therefore, the mass was inserted on a sample to sample basis

The save files were uploaded back into the software and analysed to produce a plot of activity as a function of live time. These data were then fitted with an exponential, $Ae^{-\lambda t}$, and the calculated half-life compared with the nominal value of 9.46 minutes. Figure 7.10 shows the plotted data and table 7.1 shows the fit results and final yield.

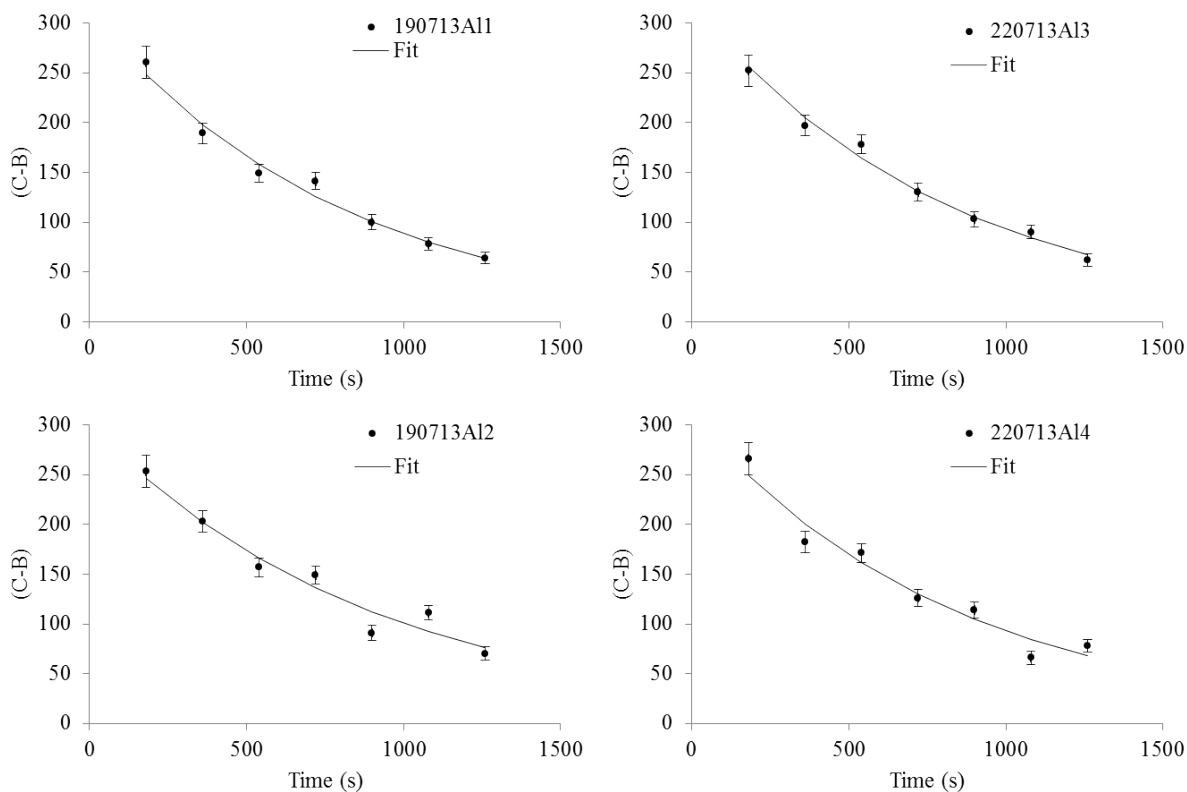


Figure 7.10: *Exponential decay of activated ^{28}Al*

Table 7.1: Aluminium Activation Results

Sample	Fitted A	Fitted λ ($\times 10^{-3}$)	Fit RMS	Half-life (min)	Yield ($\times 10^6$)
190713A11	310 ± 17	1.25 ± 0.08	1.00	9.2 ± 0.6	2.80 ± 0.20
190713A12	299 ± 31	1.09 ± 0.14	1.90	10.6 ± 1.4	2.54 ± 0.18
220713A13	319 ± 15	1.23 ± 0.07	0.91	9.4 ± 0.5	2.76 ± 0.19
220713A14	309 ± 30	1.20 ± 0.14	1.81	9.6 ± 1.1	2.72 ± 0.19
Weighted Mean	313 ± 10	1.22 ± 0.05	n/a	9.43 ± 0.35	2.71 ± 0.09

The fit results are consistent with each other and with the nominal half-life of ^{28}Al . The error on the neutron yield is based on the fit results; there is an additional systematic error of 14% from the uncertainty on the distance between the sample and the neutron source (taken to be ± 5 mm).

Sources of uncertainty will be discussed in section 7.7.

7.6 Results: Copper Samples

Figure 7.11 shows an example of the spectrum produced from one of the activated samples. The full energy peak, shown in red, is at 0.515 ± 0.018 MeV which is in good agreement with the positron annihilation peak energy of 0.511 MeV.

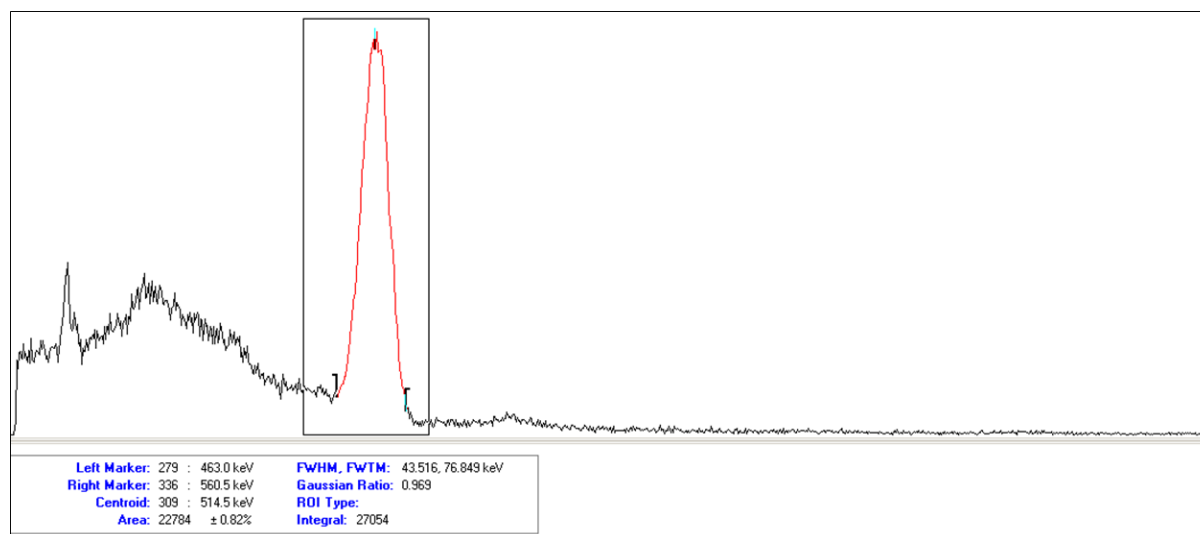


Figure 7.11: *Activation spectrum from copper sample 240714Cu1*

Figure 7.12 shows the plotted data and table 7.2 shows the fit results and final yield.

Table 7.2: Copper Activation Results

Sample	Fitted A	Fitted λ ($\times 10^{-3}$)	Fit RMS	Half-life (min)	Yield ($\times 10^6$)
240713Cu1	6584 ± 90	1.16 ± 0.03	1.24	10.0 ± 0.2	2.97 ± 0.21
310713Cu2	6294 ± 486	1.22 ± 0.09	7.29	9.4 ± 0.7	2.70 ± 0.19
060813Cu3	6282 ± 148	1.18 ± 0.03	2.35	9.8 ± 0.2	2.82 ± 0.20
060813Cu4	6452 ± 315	1.17 ± 0.06	4.76	9.9 ± 0.5	2.90 ± 0.20
Weighted Mean	6495 ± 74	1.17 ± 0.02	n/a	9.88 ± 0.13	2.84 ± 0.10

Of the four samples analysed, samples 310713Cu2 and 060814Cu4 show scatter which is larger than would be expected by statistics alone, which is reflected in the poor fit RMS values.

Differences in sample quality, or fluctuations in neutron output, would not explain this

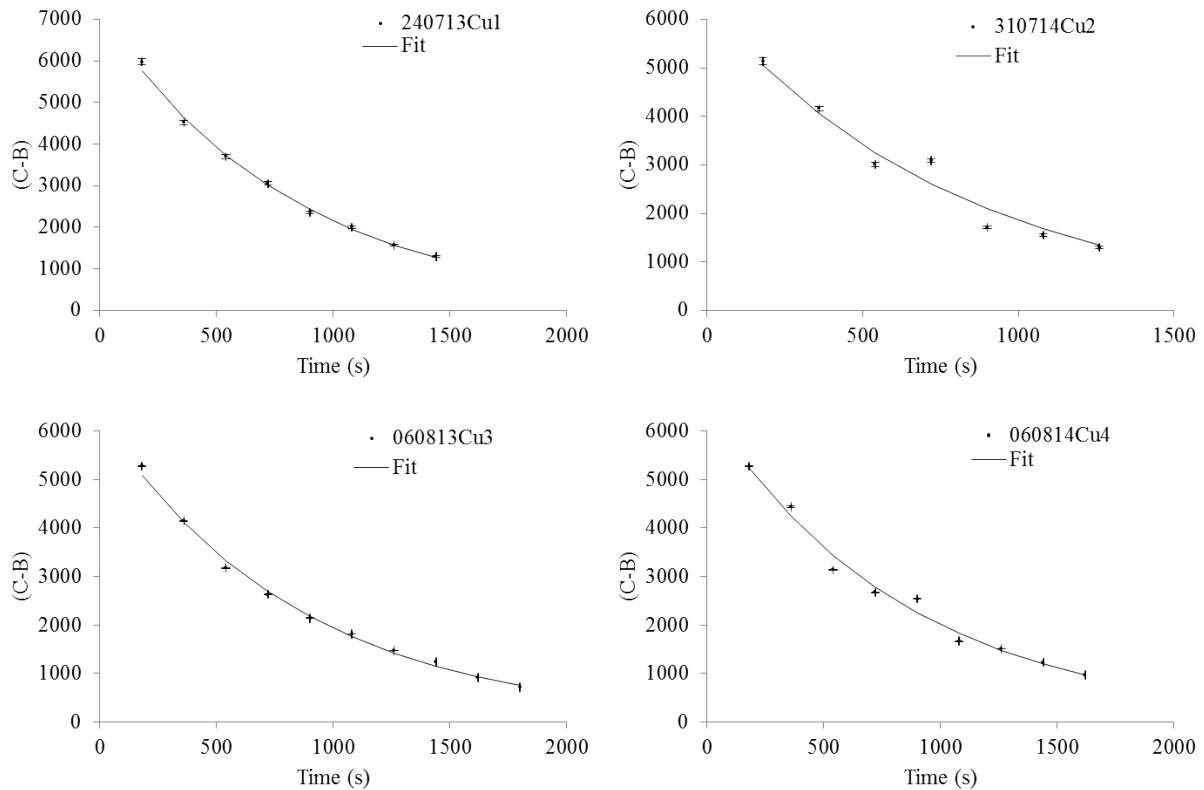


Figure 7.12: *Exponential decay of activated ^{63}Cu*

level of scatter given that data points represent successive measurements of the same sample, after a single irradiation.

In order to maintain consistent measurements over all samples, the software’s “peak analysis w/report” feature was used to measure all background subtracted peak areas. However, fluctuations in the level of background noise over the duration of a count may have led to inconsistencies in the software’s ability to accurately determine the peak limits between measurements, which would have had a significant impact on the magnitude of the nett peak area.

For sample 240713Cu1, there is evidence that the level of neutron activation may have been higher. This can be seen in figure 7.12 which shows the first measured point being around 10% larger than the corresponding points of the other three samples.

While this is not statistically significant, it may reflect some real variation in the yield

from the neutron generator as a result of variations in neutron output owing to small fluctuations in getter temperature over the course of an irradiation procedure. This is discussed in chapter 4, section 4.3.5.

Despite this, all the fitted values are consistent to within 2σ and yield half-lives that are consistent with the expected value.

7.7 Systematic Errors

Barring the $(C - B)$ term, the remaining terms in the yield equation can be split into three categories: timing, element properties and irradiation and counting geometry, all of which introduce sources of uncertainty.

The uncertainty in $(C - B)$, from which the neutron fluxes are calculated, is purely statistical and is derived from the errors associated with the exponential fits as discussed above. However, in addition to the statistical errors, causes of systematic error must be taken into account from the remainder of the terms.

7.7.1 Timing

Due to the long irradiation and counting procedure, the errors associated with the terms t_0 , t_1 and t_2 are assumed to be negligible. After irradiation, the sample transfer time from the generator to the counting detector is accounted for in the exponential decay curves, and the associated error is also considered negligible.

7.7.2 Element-Dependent Systematic Errors

Generally, the elemental properties such as the material density and isotopic abundance, along with the reaction cross-sections and branching ratios (which are element depen-

dent), can be obtained from standard reference sources [ref]. As the associated errors are small with these parameters, any systematic errors introduced by these values are assumed to be negligible also.

The detector efficiency ϵ_D , discussed in section 7.4, is dependent on the energy of the emitted gamma-ray and is characteristic of the sample material. It can therefore be classed as an elemental term.

The efficiency calibration energies of 835 keV (from ^{54}Mn), and 511 keV (from ^{22}Na), are close enough to the energies of interest (844 keV for aluminium and 511 keV for copper) so that no significant systematic error is introduced by the energy dependence of the efficiency. However, the measured efficiencies themselves introduce errors of 4% and 5% for aluminium and copper respectively.

7.7.3 Geometry

In all experiments of this nature there are systematic errors which arise from the experimental setup. The systematic errors due to the counting geometry are negligible, and because the level of induced activity in the sample is low (and therefore pulse pile-up is not an issue), can be minimized by adopting a detector top geometry identical to that used in the efficiency calibration.

The largest source of uncertainty associated with the irradiation geometry is derived from the source to detector distance, d . As described in chapter 4, the neutron generator is a DT fusion source supplied as a sealed tube with a spherical cathode grid, as advised by the manufacturer [ref NSD]. However, the exact dimensions and properties of the grid are proprietary information and no detailed technical drawing was provided other than a basic CAD drawing of the outer dimensions with an “approximate” centre.

The analysis presented here is based on the assumption that the region of neutron production is approximately spherical and is centrally located, so that the distance from the

source to a sample located directly on the tube is half the tube diameter. While this is a reasonable assumption to make, it is not guaranteed to be correct and therefore a large uncertainty of ± 5 mm was assigned to d . This led to a systematic error of $\pm 15\%$ in the derived neutron yield.

It should be noted that this estimate is very approximate, and more studies would have to be done if we wanted to use the facility for cross-section measurements. However, it is adequate for the analysis reported here, which is a feasibility study rather than a precision measurement.

It is possible to assess the validity of the above claims by irradiating (at least) two samples simultaneously at either side of the generator chamber and comparing the results, but the experimental setup with the bulk shielding around the tube was not designed to facilitate this at this stage and therefore will be done at a later stage.

7.8 Conclusions

The yield values derived from the aluminium and copper samples are consistent with each other and lead to a final value for the neutron generator yield of $(2.70 \pm 0.07) \times 10^6$ neutrons per second.

The systematic error on this value is dominated by the uncertainty in the effective position of the neutron source within the generator, which is estimated to contribute $\pm 15\%$.

Detector efficiency systematic errors of about $\pm 5\%$ were obtained using different calibration sources for the two sample elements and are therefore assumed to be uncorrelated, leading to an overall systematic error of $\pm 3\%$ on the mean of the two results.

The neutron flux as specified by the manufacturer for the operating parameters used in this experiment is 4×10^6 neutrons per second, which is 33% higher than our result shows. This is partly because the manufacturer quotes the total flux from both DT and DD

fusion, whereas our measurements are for DT neutrons only. The relative cross-sections for DD and DT fusion under these conditions are 7 barns and 0.04 barns respectively, so we estimate that only a small percentage of the total yield is from DD neutrons assuming the output is a function of the relative cross-sections.

Based on our result, this corresponds to an estimated DD yield of only 0.014×10^6 neutrons per second, and although not included in our measurement, would not increase our final yield significantly enough to approach the manufacturer's quoted figure.

It is possible that the systematic error is larger than anticipated, although at this stage it is impossible to address this without further experimentation. The quoted yield from the manufacturer was derived before the generator was delivered and was not compared to our experimental yield until over a year after its arrival and after 100+ hours of generator run time during the characterization and installation process had elapsed. Also, the manufacturer did not provide an associated error on their measured yield, and performed the measurement using a proton recoil detector rather than via neutron activation. Without knowing their sources of uncertainty it is impossible to know exactly how accurate our result is.

The manufacturer also informed us that the deuterium-tritium gas mixture was "lean" in its tritium content. If the gas mixture was identical during both yield assessments (ours and NSD Fusion) then our results are not consistent. If, however, the gas mixture was lower in tritium during our characterization then this would be reflected by a lower measured result, as is the case with our data.

As stated in section 7.7.3, the source position could be better localised by making multiple measurements simultaneously in order to avoid additional effects from pulse to pulse variations. This could be achieved by positioning samples at several different points around the generator casing and triangulating the centre position using the results. It is possible that this measurement can be undertaken in the future.

Chapter 8

Thermal Neutron Activation

Analysis of Hydrogen and Nitrogen

8.1 Introduction: (n, γ) reactions on ^1H and ^{14}N

This chapter documents the experimental work undertaken to identify the lines of interest from both hydrogen and nitrogen in bulk samples. The main body of the theory is outlined in chapter 2 but a brief outline is given here.

8.1.1 The $\text{H}(n, \gamma)\text{D}$ reaction

The cross-section for this reaction is 330 mb at 0.025 eV [REF]. A thermal neutron is captured by a hydrogen nucleus forming a deuterium nucleus. Using equation 2.32 the excitation energy ($S_n + E_n$) of the compound nucleus is 2.22 MeV which is equal to the binding energy of the deuteron. Because there are no excited states of deuterium, a direct transition to the ground state is the only possible decay mode and therefore a gamma-ray of this energy is emitted [REF].

As the energy of this gamma is low (relative to the other key gamma-rays of interest)

it was the first signal identified and could then be used as a calibration point for the detector array.

8.1.2 The $^{14}\text{N}(\text{n}, \gamma)^{15}\text{N}$ reaction

The cross-section for this reaction is 79.5 ± 1.4 mb [23]. A thermal neutron is captured by a ^{14}N nucleus producing an excited compound state of ^{15}N with an excitation energy of 10.83 MeV. This energy again goes into the production of gamma ray photons but unlike deuterium, there are several excited levels below the neutron separation energy resulting in a series of discrete lines being emitted (see chapter 2). The key gamma-ray of interest has an energy of 10.8 MeV; This transition has a cross-section of 11.3 ± 0.8 mb [23].

This energy corresponds to the largest direct transition in excited ^{15}N and is characteristic to nitrogen as there are very few other isotopes having decay modes emitting a gamma approaching such a large energy [12]. This line should therefore be easily distinguishable in the spectrum and will act as positive identification of nitrogen in the sample [14].

8.2 Experimental Setup

The configuration and operating procedure for the neutron source is discussed in chapter 4 and the shielding and collimation of the generator in chapter 6. This setup remained the same throughout the experiments (unless stated). The following section describes the gamma-ray spectroscopy setup and shielding only.

The detector used was a Scionix 4" \times 4" thallium-doped sodium-iodide scintillation detector. The detector was placed on top of the lead-lined borated paraffin wax stack, parallel to the sample location at a distance of 10 cm from the centre and perpendicular to the direction of the collimated neutron flux (figure 8.1).



Figure 8.1: *Figure showing the collimated neutron generator, shielded scintillation detector and sample location.*

The primary shield was constructed of $5\text{ cm} \times 5\text{ cm}$ lead blocks positioned in a stack surrounding the active volume of the crystal as well as the photomultiplier tube and the preamplifier. Figure 8.2 shows the construction.

Initially, the front face of the detector was positioned at the very edge of the lead stack in order to have the crystal as close to the sample as possible. Although this configuration was not ideal in terms of reducing the background acceptance window for the detector, it was seen as a viable trade-off to make in the early stages to minimize the sample-detector distance given that the amount of activation was expected to be low. In further experiments the location of the detector was altered to improve the signal-to-noise ratio, where this occurs the new configuration will be discussed in the relevant section.

The rear of the lead stack had an aperture in order to feed the signal output and high voltage input through to the photomultiplier tube, but this was back-filled with further

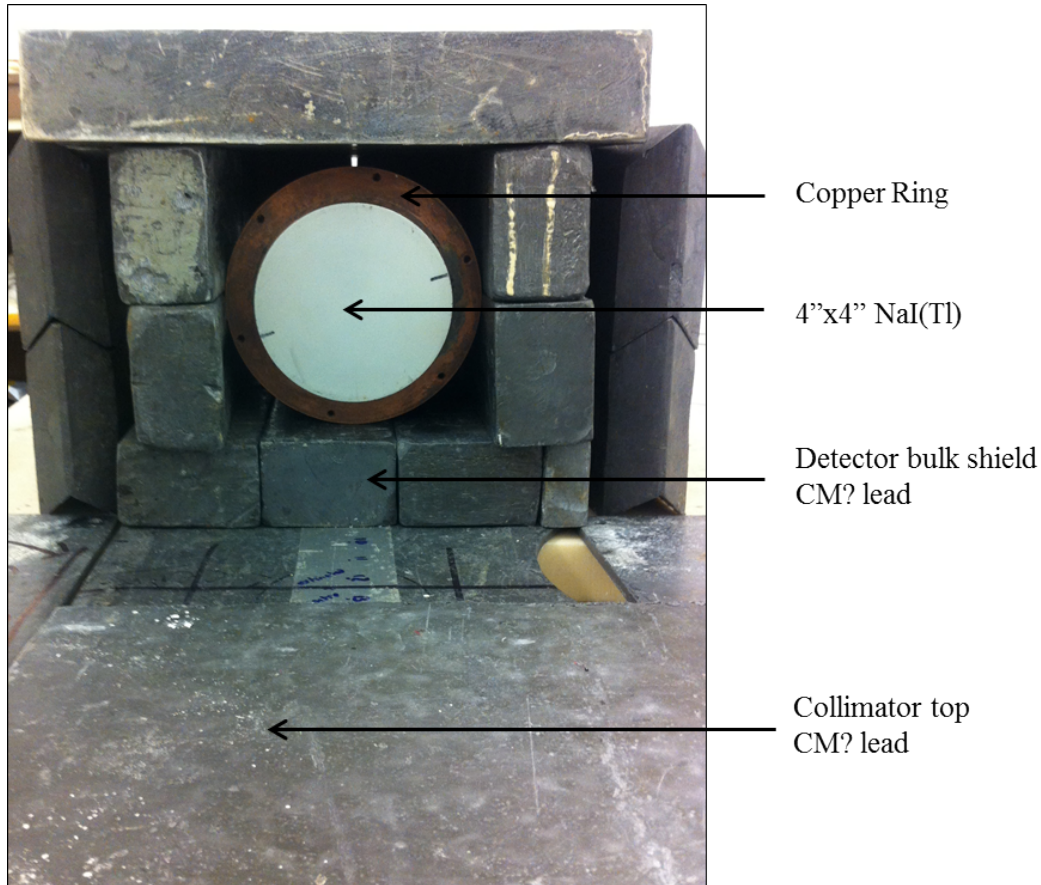


Figure 8.2: $4'' \times 4''$ Sodium-Iodide scintillation detector *in situ* shielded with lead

lead blocks to minimize the background. Finally, the NaI(Tl) crystal was sheathed with a 0.5 cm thick collar to shield the detector from low energy gamma-rays produced by activation of the lead stack.

8.2.1 Data acquisition

The output of the photomultiplier tube was passed through a switched attenuator to reduce the amplitude of the output pulses given that typical anode signals from NaI(Tl) detectors induced by $> \text{MeV}$ gamma rays can often reach 10V+ and the dynamic range of the MCA was only 0V - 2V . The attenuator output was fed to the input of an Ortec 570 spectroscopy amplifier with a shaping time of $0.5 \mu\text{s}$, through an Ortec 426 linear gate and a Kromek K102 USB- MCA to the PC. The gate was set to DC Indibit mode. A pulse

height spectrum could then be produced using the Kromek KSpect gamma acquisition and analysis software. All MCA data was taken over 4096 channels which is the maximum capability of the hardware. The data was re-binned during the course of the analysis in order to highlight certain features in the spectrum; where this has taken place it will be noted.

Determining the gate width

The gate width was determined by a Tennelec TC410A delay/gate generator. The 24V sync output from the generator CCU was sent to the input of a t_0 module designed and built by Dr. John McMillan which acted as a fan-out of both NIM and TTL outputs, corresponding to the start of the high voltage pulse from the neutron generator control (discussed in chapter 4). The NIM output acted as the trigger input for the delay/gate generator, and the subsequent logic output was sent through a Caen 2255A dual timer to the DC inhibit on the rear of the linear gate. The delay period could then be set by the TC410A and the gate width determined by 2255A up to a width of several milliseconds. This provided a positive “blanking pulse” which would inhibit the registering of events occurring during the width of the gate. Figure 8.3 shows the flow diagram.

For radiative capture reactions it was necessary to blank pulses associated with events occurring both during and several microseconds after the fast neutron burst to allow for the neutron thermalization time. Calculation of the thermalization time is a complex scenario dependent on several factors beyond the scope of this thesis, but a brief summary of the theory is included below.

In a given material, the mean distance a neutron travels between interactions is called the *mean free path*, λ , which is the inverse of the macroscopic cross-section Σ , written as

$$\lambda = \frac{1}{N\sigma} = \frac{1}{\Sigma} \quad (8.1)$$

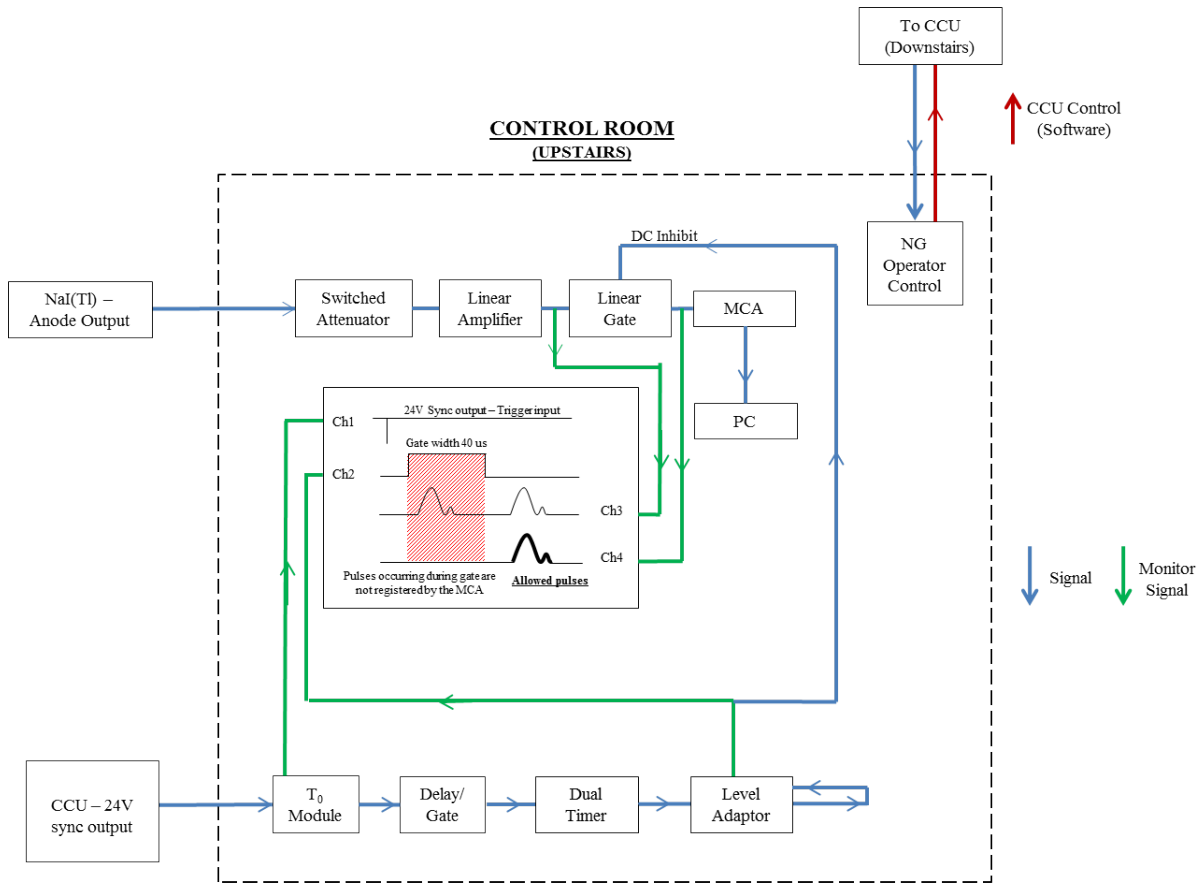


Figure 8.3: *Signal processing chain for thermal neutron induced events*

where N is the number density (cm^{-3}) and σ is the microscopic cross-section for the interaction (cm^{-2}). The complexity arises when we estimate the reaction rate $\frac{\lambda}{v_n}$, where v_n is the neutron velocity.

Because the microscopic cross-section is energy dependent in a given medium, the magnitude of the cross-section will change after each collision and therefore the mean free path and reaction rate will also alter. A full Monte-Carlo simulation with all the known constituent materials is the only way of accurately predicting the neutron thermalization time.

A crude approximation was calculated based on the time of flight of both a 14 MeV and a 2.3 MeV neutron through the sample geometry, undergoing a series of elastic scattering events until the kinetic energy was 0.025 eV. I have assumed that the sample consists

of a cube where the probability for a head-on collision with a hydrogen nucleus is 1. The neutron passes through the sample, elastically scattering with a proton at the far end of the sample. Given that a neutron of energy $E_{initial}$ transfers energy $\frac{E_{initial}}{2}$ in a head-on collision with a stationary proton, a 14 MeV neutron will take around 30 of these collisions to reach thermal equilibrium, and a 2.3 MeV neutron around 25 collisions [REF KNOLL].

It was assumed the neutron then travels the distance of the sample again in the opposite direction with reduced energy and interacts again in a head-on collision on the opposite side; this process repeats itself over several collisions until the neutron is thermalized. A spreadsheet was produced which calculated the neutron velocity from its kinetic energy after each interaction using

$$v = \sqrt{\left(\frac{2E_n}{m}\right)} \quad (8.2)$$

It was then possible to work out the time of flight for the initial distance travelled plus the flight time after each collision and sum them over the required number of collisions.

For a sample size of 12 cm the thermalization time using this method was 180 μs for 14 MeV neutrons and around 160 μs for 2.3 MeV neutrons respectively.

This of course assumes that the neutron travels the same distance of 0.12 m after every collision; in reality this is not the case as the mean free path is constantly changing. Therefore, these figures represent an extreme case and it is highly unlikely that a neutron would take such a long time to thermalize in a “real” sample. A second case was then investigated in which the distance travelled was scaled according to the elastic scattering cross-section. Figure 8.4 shows the cross-section in barns as a function of neutron energy.

At thermal energies up to around 1 eV, and from 0.1 MeV to 14 MeV the cross section decreases by an order of magnitude or more, whereas between 1 eV and 0.1 MeV the cross-section is flat. Plotting these three regions in Excel and producing a fit for each region allowed the hypothetical distance travelled after each of the 30 collisions to be

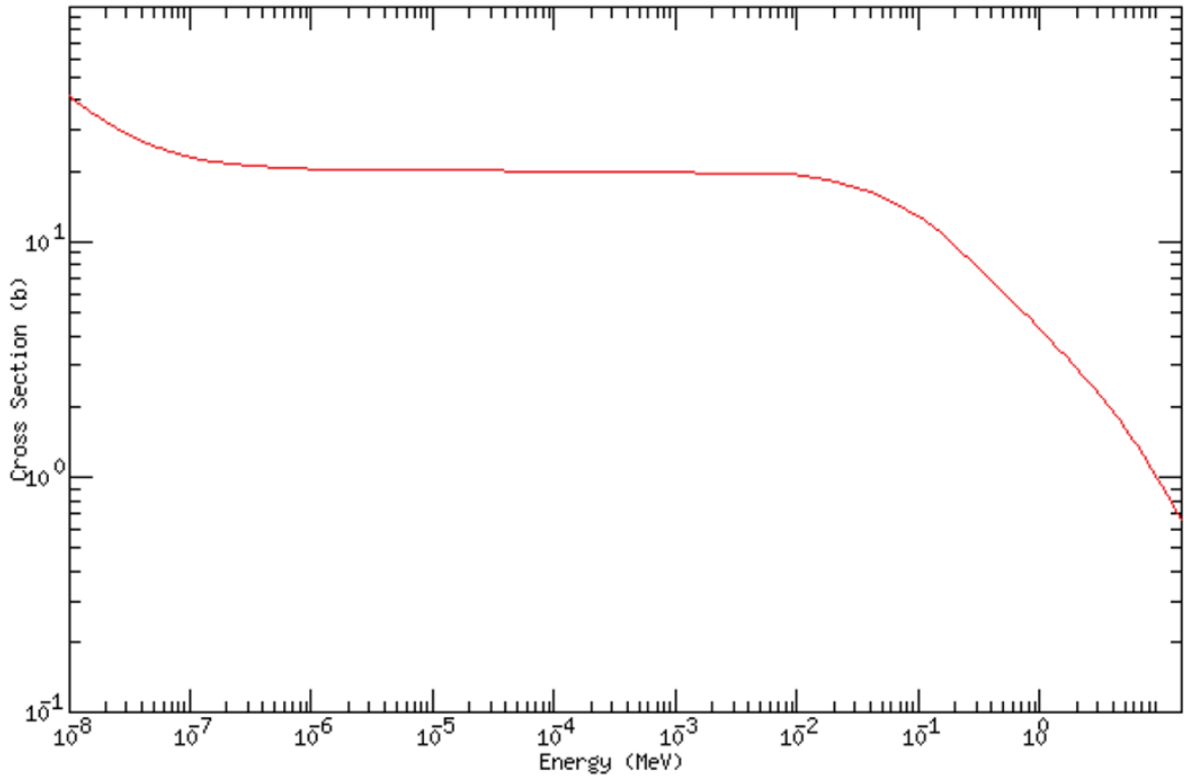


Figure 8.4: *Elastic scattering cross section between thermal energies and 15 MeV. Taken from [REF ENDFPLOT]*

scaled according to the relevant energy dependent cross-section.

This meant that over the first 8 collisions the distance travelled reduced but then remained constant over the next 18 until the neutron had energy 0.1 MeV. The distance then again reduced over the remaining collisions according to the scaling factor. By working out the time-of-flight for each of the new distances and summing, the thermalization time is calculated to be around 15 μs to 20 μs for 2.3 MeV and 14 MeV neutrons respectively.

Again, this is a unrealistic case, but gives some rough approximations as an estimation of a gate width for the detector setup. A paper by [FIND ONE NOW] using a Monte Carlo simulation estimates a neutron thermalization time of [ADD THIS NUMBER US] in typical plastic compounds of similar chemical compositions to our samples. Although just a hand-waving argument it adds substance to the selection of our gate width without having to perform the complex simulation. Figure [ref APPENDIX IMAGE] shows the

template.

Using this argument the gate was set at a conservative width of 30 μs and was shifted using the delay to open at 5 μs before the neutron burst and switched off at a time of 25 μs after the t_0 trigger. This would inhibit events reaching the MCA associated with induced gamma (and x-ray) activity associated with the initial fast neutron burst and extend the detection period for several ms until the subsequent trigger, increasing the possibility for registering thermal events between neutron pulses.

In reality, this signal collection period is an over-estimation and the actual gate width for future experiments will be a finite window beginning just after the estimated neutron thermalization time and ending before the activated isotopes induced in the surrounding materials have time to decay and distort the spectrum. This width is yet to be concluded, however, and will be touched upon in future work. In terms of increasing the probability of registering the desired signals the gate remained open long for the remainder of the experimentation.

8.3 Calibration of the Kromek K102 USB-MCA

Due to the wide range of energies associated with the signals of interest, between 2.2 MeV and 10.8 MeV, it was necessary to calibrate the MCA to cover this range. The laboratory sources available (with primary photopeak energies) were ^{137}Cs (0.662 keV), ^{60}Co (1.173 MeV & 1.332 MeV), ^{22}Na (0.511 MeV & 1.275 MeV) and ^{133}Ba (0.302 MeV & 0.356 MeV), all of which were relatively low energy gamma-rays covering only a small proportion of the required spectrum.

To cover the region of the 2.22 MeV hydrogen line, the sum peak of the two ^{60}Co gamma-rays (2.505 MeV) could also be used as a higher energy data point as the two gammas are emitted simultaneously with a branching ratio of 100%. The switched attenuator and amplifier coarse gain were adjusted until the 2.505 MeV sum peak of ^{60}Co was

located around channel 820 of 4096, which based upon a linear calibration would give us a dynamic range of approximately 12.5 MeV.

Each of the sources was placed in a clamp at a distance of 10 cm, corresponding to the mid-point of the sample location, for an irradiation time of 10 minutes. Figure 8.5 shows an example of a calibration spectrum (^{60}Co) with the photopeaks, sum peak and corresponding Compton edges and backscatter peaks labelled. A linear calibration of the software was then performed which gave

$$\text{Energy (MeV)} = \frac{(3.1 \times \text{CH}) - 11.3}{1000}. \quad (8.3)$$

where CH is the channel number corresponding to the centroid of the relevant photopeak, 3.1 is the gradient of the line and -11.3 is the y-intercept.

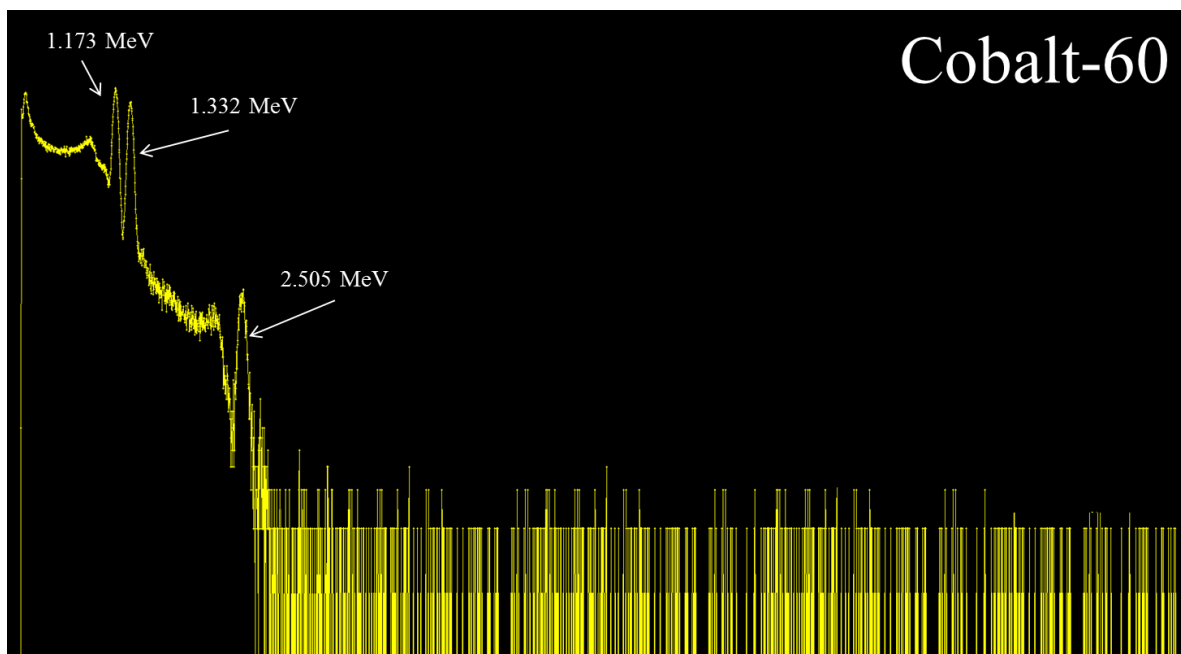


Figure 8.5: *Cobalt-60 spectrum acquired on the Kromek USB-MCA*

The detection efficiency of the NaI(Tl) crystal decreases as the energy of the gammas increases [ref Knoll efficiency curve] and this is also highlighted by a relative pulse height difference of two orders of magnitude between 1.3 MeV and 2.5 MeV. Nonetheless, a linear calibration could still be performed to cover the energy range of interest and allows

confidence to be placed in the detectors ability to determine the 2.2 MeV hydrogen line. As there were no higher energy calibration sources available to us we were unable to assess the quality of the calibration over the full dynamic range of channels; however, after sample irradiation the calibration was deemed satisfactory from the identification of the desired gamma lines.

8.4 Background Contributions to the Spectra

Investigations were made into the level of spectral contamination from both natural background and generator induced background. Identification of gamma-rays associated with the natural radioactivity of the detector, shielding, laboratory construction materials, airborne radioactivity and cosmic radiation (primary and secondary) were all addressed. A spectrum of “generator induced background” was also taken with the generator running but without a sample in situ.

8.4.1 Natural Background

Figure 8.8 shows a spectrum of background contributions taken with a 3” × 3” NaI(Tl) detector inside a massive lead and borated paraffin wax shield. The spectrum is typical of what one would expect from a shielded radiation detector with contributions from two of three naturally occurring decay series, headed by the radionuclides ^{238}U and ^{232}Th , terrestrial, airborne and cosmic radiation. ^{235}U is not abundant in nature and its decay series can be ignored [REF]. Figure 8.7 shows our natural background spectrum acquired over 10800 seconds over the full dynamic range of channels.

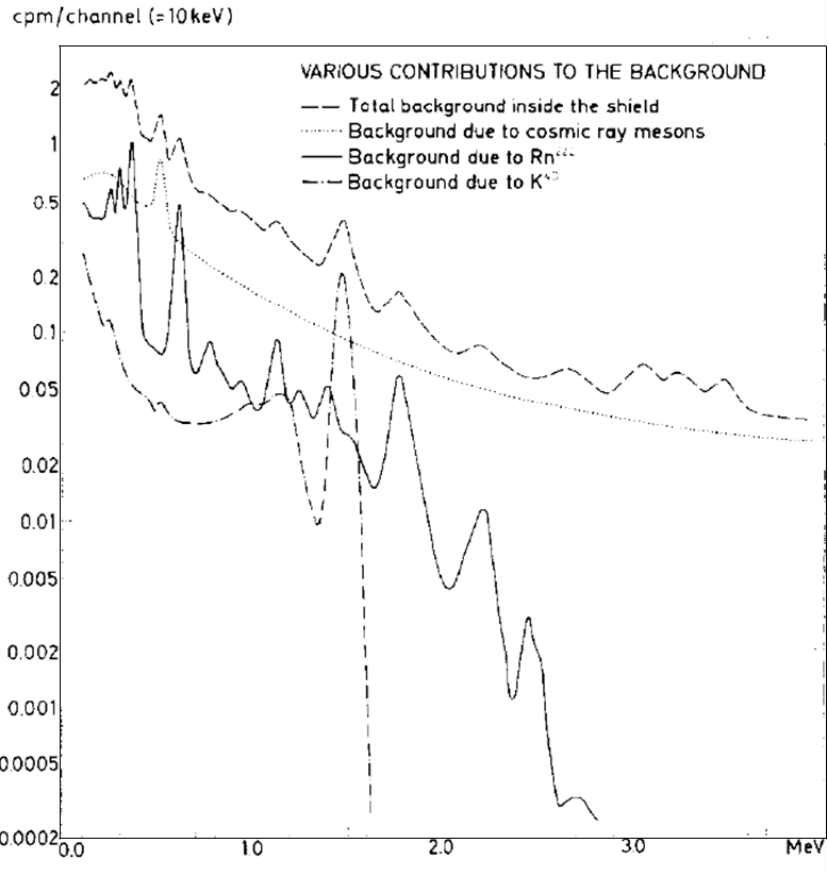


Figure 8.6: Taken from [?]

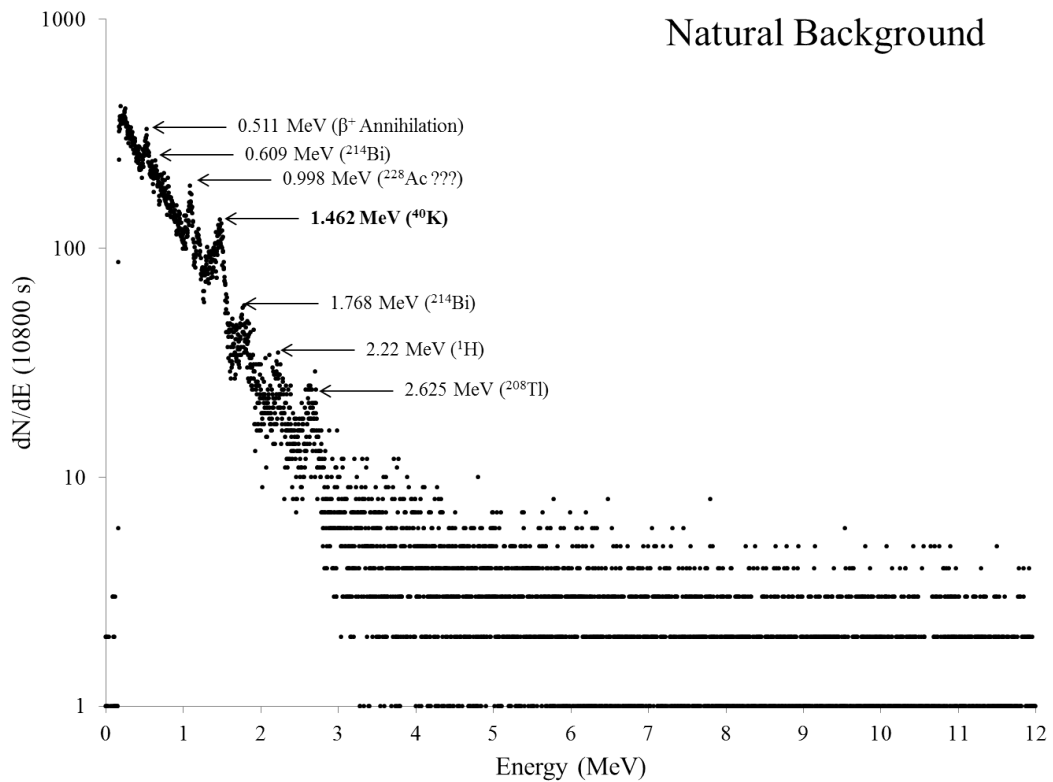


Figure 8.7: Spectrum acquired over 10800 seconds to assess the natural background contribution to the spectra. The main peaks have been labelled

The dominant peak at 1.462 MeV comes from ^{40}K , which is found everywhere from the Earth's crust to all organic material and is a standard peak obtained in almost all detector backgrounds. Of particular note are the ^{214}Bi peaks and the ^{208}Tl peak associated with the decay of ^{222}Rn and ^{220}Rn respectively, and the characteristic hydrogen line at 2.2 MeV is also visible. The 2.2 MeV peak is most likely induced by cosmic ray neutrons which have been moderated and subsequently captured by the hydrogen component of the bulk shield.

Comparing our background with that obtained by Stenberg, we can see that our natural background is dominated by ^{40}K as expected.

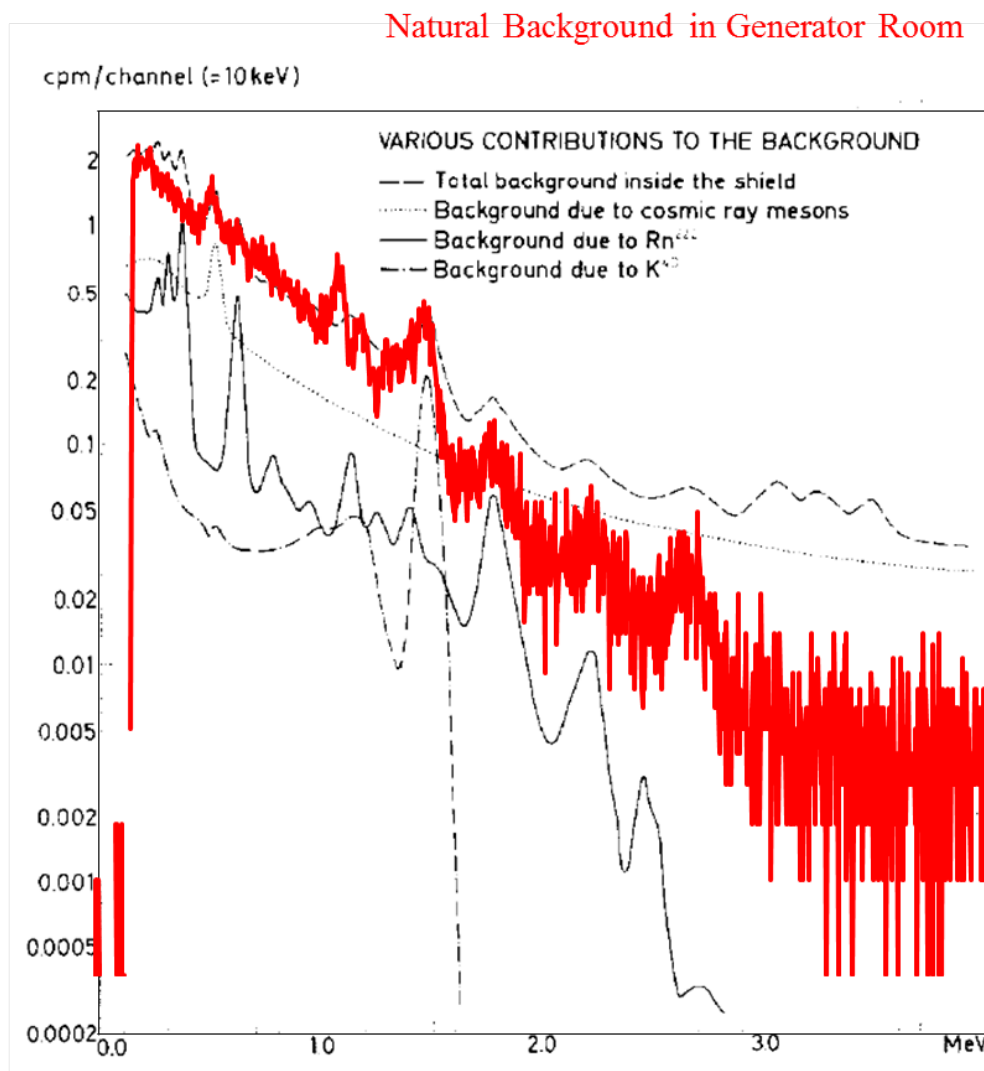


Figure 8.8: Data from our background spectrum over 4 MeV (red) compared to that taken by Stenberg.

8.4.2 Generator Induced Background

A more significant spectrum is that produced by the detector when the neutron generator is running. The nature of the collimation and shielding means that there will be a number of neutron induced reactions from these materials, some of which will be deposited in the detector crystal. Given that the only difference between this scenario and sample irradiation will be the sample itself, performing a subtraction of the generator background from the sample spectrum will provide a much more accurate spectrum for analysis.

Figure 8.9 shows the generator background, again over 4096 channels.

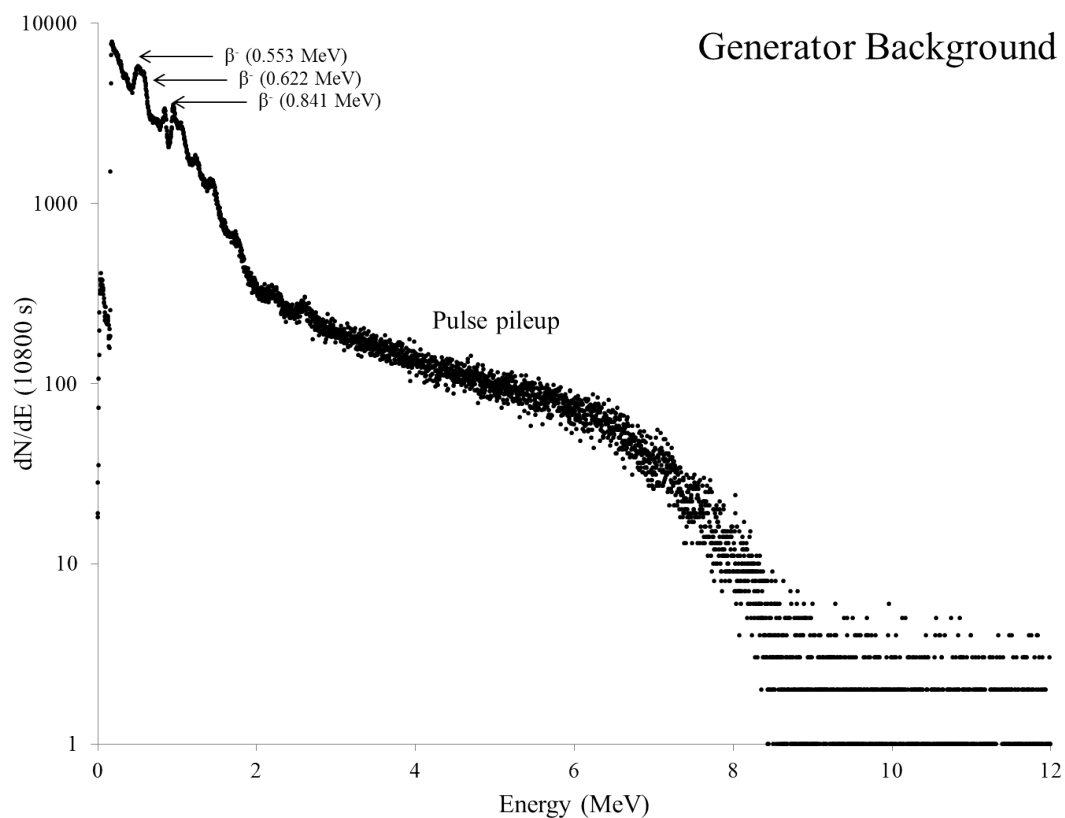


Figure 8.9: *Spectrum acquired over 10800 seconds with the generator running at 500V - 30 Hz - 6.5 μ s*

The peaks labelled as β^- arise from neutron activation of the sodium and iodine components of the detector crystal.

The measured peak at 0.553 MeV comes from full energy deposition from the beta pro-

duced by the β^- decay of ^{24}Na to ^{24}Mg which has a mean energy of 0.554 MeV, an endpoint energy of 1.392 MeV and a branching ratio (BR) of 99.86%. The decay also produces gamma radiation of energy 1.368 MeV and 2.754 MeV which are also observed in the spectrum.

The measured peaks at 0.622 MeV and 0.841 MeV appear from betas associated with the decay of ^{128}I to ^{128}Xe producing mean beta energies of 0.633 MeV (endpoint 1.676 MeV, BR 11.56%) and 0.832 MeV (endpoint 2.119 MeV, BR 80.0%). There are also gamma-rays produced, with the two most intense emissions occurring with energy 0.526 MeV and 0.969 MeV. While the second peak is observed with a measured energy of 0.974 MeV, the lower energy peak cannot be resolved due to the other emissions with similar energy and an annihilation peak at 0.511 MeV.

8.5 Identification of the 2.2 MeV Gamma from the (n, γ) Reaction on Hydrogen

In order to detect the characteristic 2.22 MeV hydrogen line a sample was prepared consisting of 7.7 kg of polypropylene pellets in a cardboard box of dimensions 18 cm \times 18 cm \times 25 cm. The sample was irradiated with neutrons for 10800 seconds and a pulse-height spectrum produced. Figure 8.10 shows the spectrum acquired over the full range of channels in order to highlight the lower energy features.

The generator induced background has been subtracted so the spectrum only shows features associated with the presence of the polypropylene pellet sample.

The main observable feature is the unmistakable line observed at 2.22 MeV originating from the (n, γ) reaction on hydrogen with a single escape peak (labelled SE) at 1.70 MeV. The peak area is 164038 ± 405 counts and the peak-to-total ratio is $4.5 \pm 0.2\%$, a significant result.

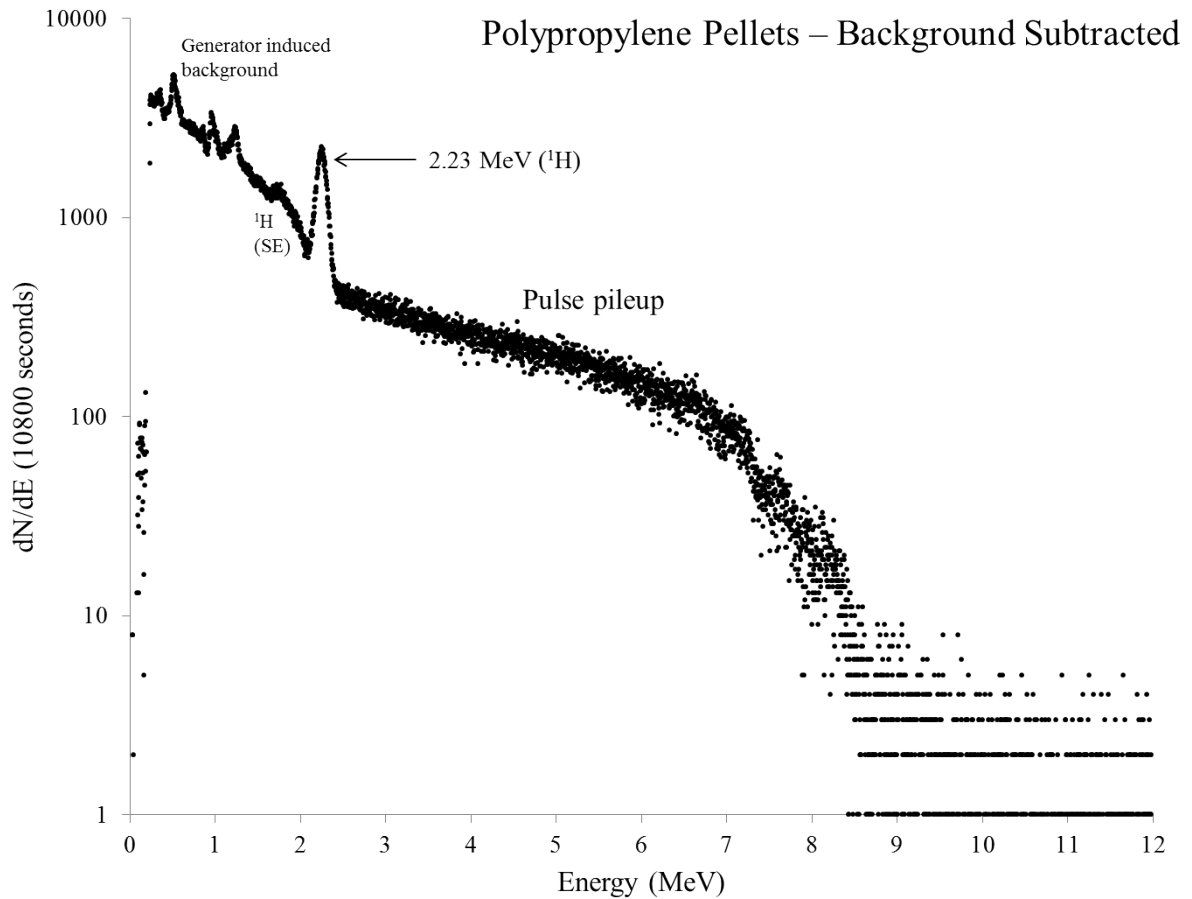


Figure 8.10: *Polypropylene sample*

The features below 3 MeV correspond to the generator induced background as stated previously. Even though the polypropylene spectrum is background stripped, the mass of hydrogenous material in the sample provides a greater amount of moderator to aid with neutron thermalization and as a result there will be an elevated level of thermal neutrons incident on the detector crystal relative to the background. Also, an increase in the Compton continuum from scattered hydrogen gammas would further increase the number of counts over these channels.

Figure 8.11 shows an overlay of the generator induced background compared to the raw data obtained from the polypropylene sample which highlights why the background subtracted spectrum and the sample spectrum show the same features.

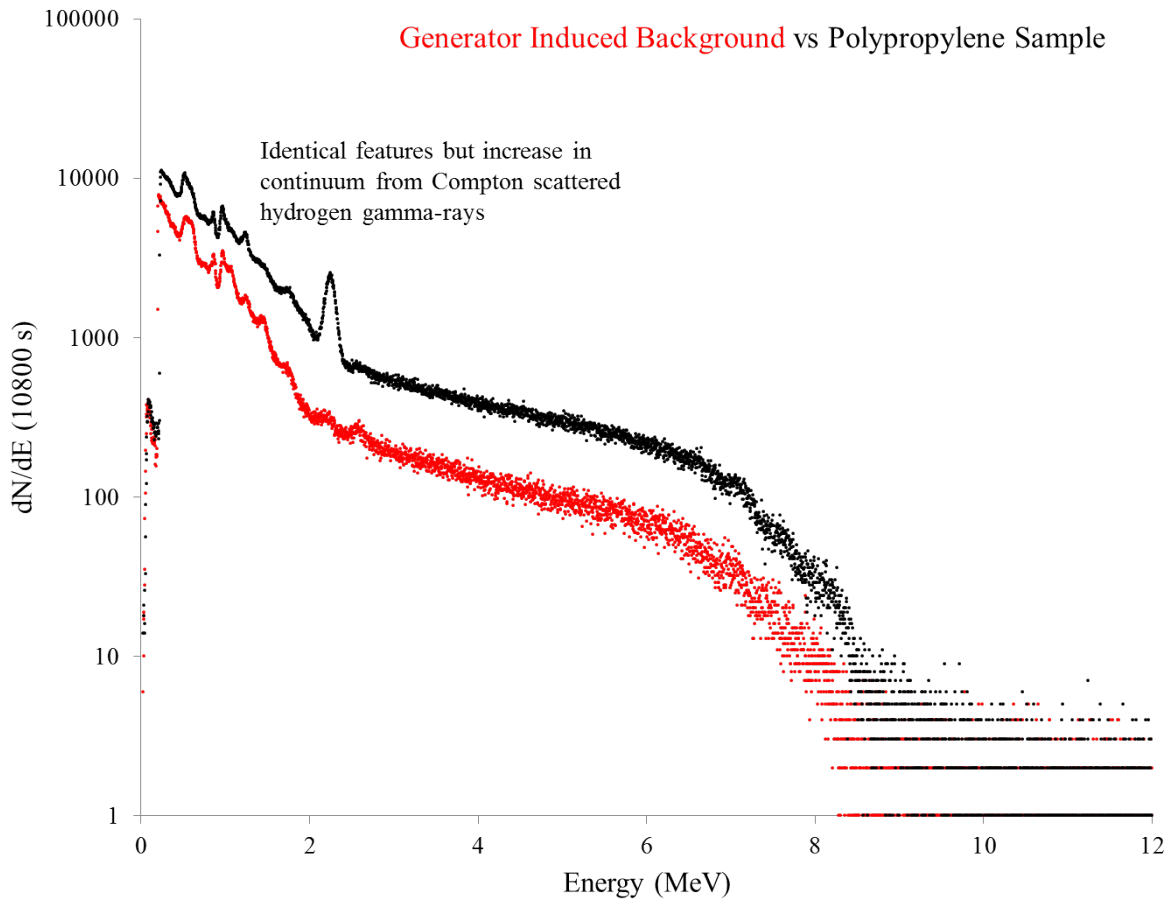


Figure 8.11: Spectra showing identical features at different magnitudes to highlight the effect of increased hydrogen content in the sample.

8.6 Identification of the 10.8 MeV Gamma from the (n, γ) Reaction on Nitrogen

The polypropylene sample was replaced with a urea pellet sample of the same volume corresponding to a mass of 10.5 kg. Figure 8.12 shows a comparison spectrum between the polypropylene pellet sample and the urea sample irradiated over the same time period with the urea spectrum in red. The main difference between the two spectra is the apparent reduction in counts across the full range of channels, which is to be expected owing to the reduced relative hydrogen content of the sample. The presence of hydrogen in the urea is also identified, but the characteristic nitrogen peak at 10.8 MeV does not appear with any significance other than an apparent increase in counts over a region of

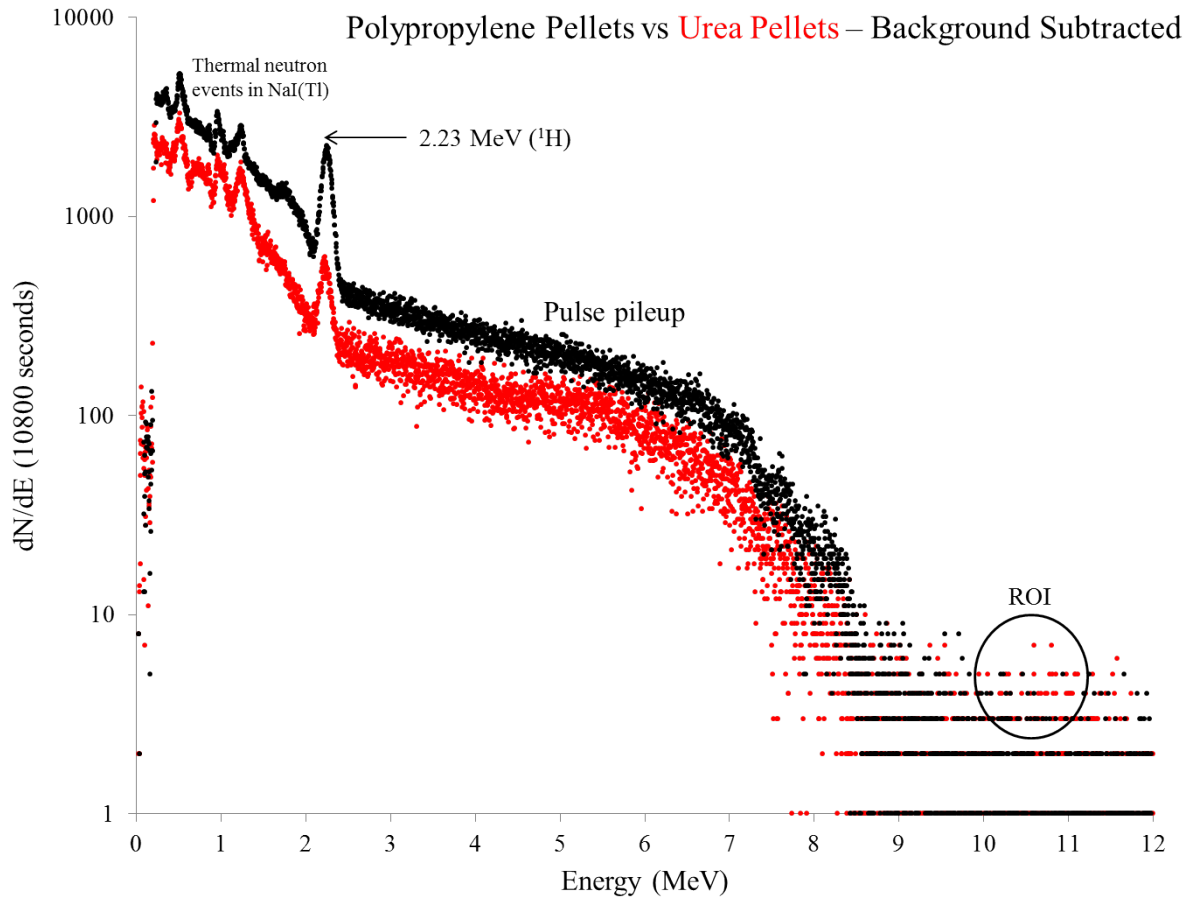


Figure 8.12: Comparison of polypropylene sample and urea sample spectra

interest (ROI) selected between 10 MeV and 12 MeV where this nitrogen peak would be expected.

The level of resolution afforded by the MCA is not warranted in this region and so the data was re-binned over 256 channels in an attempt to highlight this ROI.

Figure 8.13 shows the urea spectrum re-binned over 256 channels and shows the ROI beginning to resemble a peak at the correct energy, with figure 8.14 showing a comparison between the two samples. By integrating the number of counts between 10 MeV and 12 MeV for both samples, an increase of $49.8 \pm 3.8\%$ was observed in the urea sample with a peak-to-total found to be 0.057%.

In order to highlight this ROI further and attempt to obtain a more accurate value for the peak area, the polypropylene spectrum was subtracted from the urea spectrum over

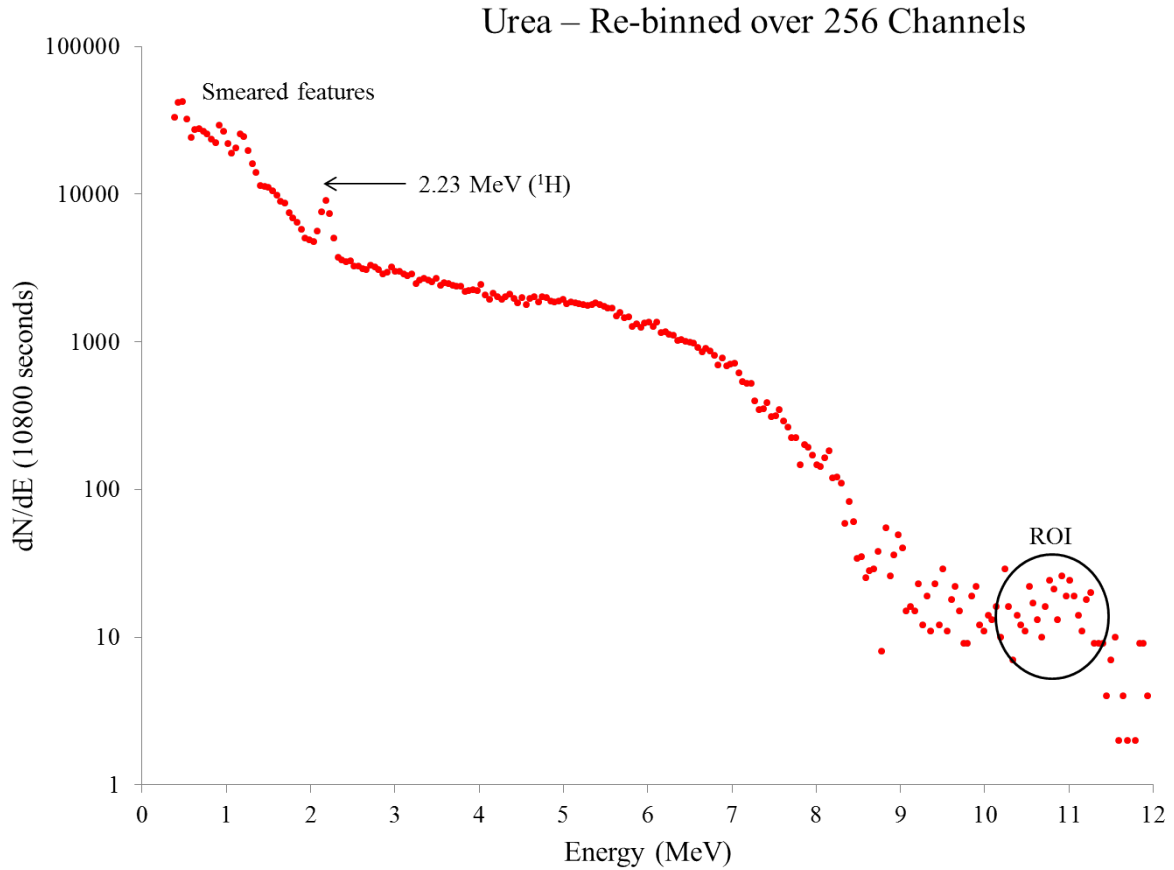


Figure 8.13: *Urea sample spectrum rebinned over 256 channels*

all channels and a bar chart produced. Figure 8.15 shows the result.

The only data remaining after this subtraction is that resembling a peak centred on 10.82 ± 0.42 MeV with a peak area of 514 ± 23 counts which corresponds to the above percentage increase.

Given that the only difference between the two acquisitions is the presence of nitrogen in the urea sample, this acts as confirmation of the detection of nitrogen using TNA from sample moderated fast neutrons emitted by our pulsed-neutron generator.

In terms of using this technique to determine differences in mass concentrations of CHON compounds such as that required in explosives detection, a simple hydrogen mass ratio could be calculated between polypropylene and urea using their molecular weight and compared to that obtained experimentally using our sample spectra.

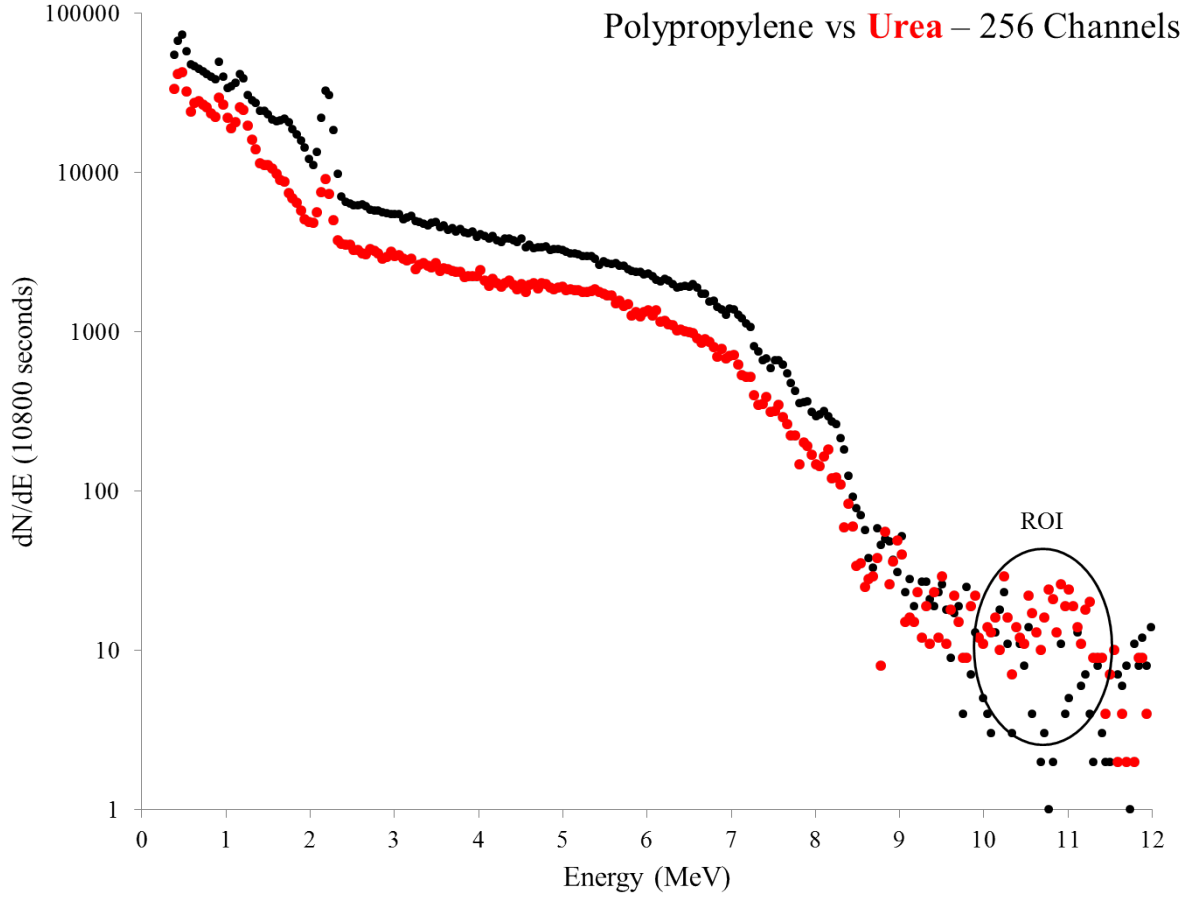


Figure 8.14: Comparison of polypropylene and urea spectra rebinned over 256 channels

The mass ratio of hydrogen in urea compared to that of polypropylene is

$$\frac{M_{\text{H}}(\% \text{Urea}) \times m_{\text{sample}}(\text{g})}{M_{\text{H}}(\% \text{Polypropylene}) \times m_{\text{sample}}(\text{g})} = \frac{0.671 \times 7700}{0.144 \times 10478} = 0.635 \pm 0.058 \quad (8.4)$$

where the hydrogen mass percentages were obtained by the Lenntech molecular weight calculator [ref]

Using the KSpec software to integrate the counts in the peak area of the 2.22 MeV hydrogen line in both the polypropylene and urea sample spectra, we calculate a relative hydrogen ratio of

$$\frac{A_{2.2\text{MeV}}(\text{Urea})}{A_{2.2\text{MeV}}(\text{Poly})} = \frac{95845 \pm 309}{155399 \pm 394} = 0.617 \pm 0.002(1\sigma) \quad (8.5)$$

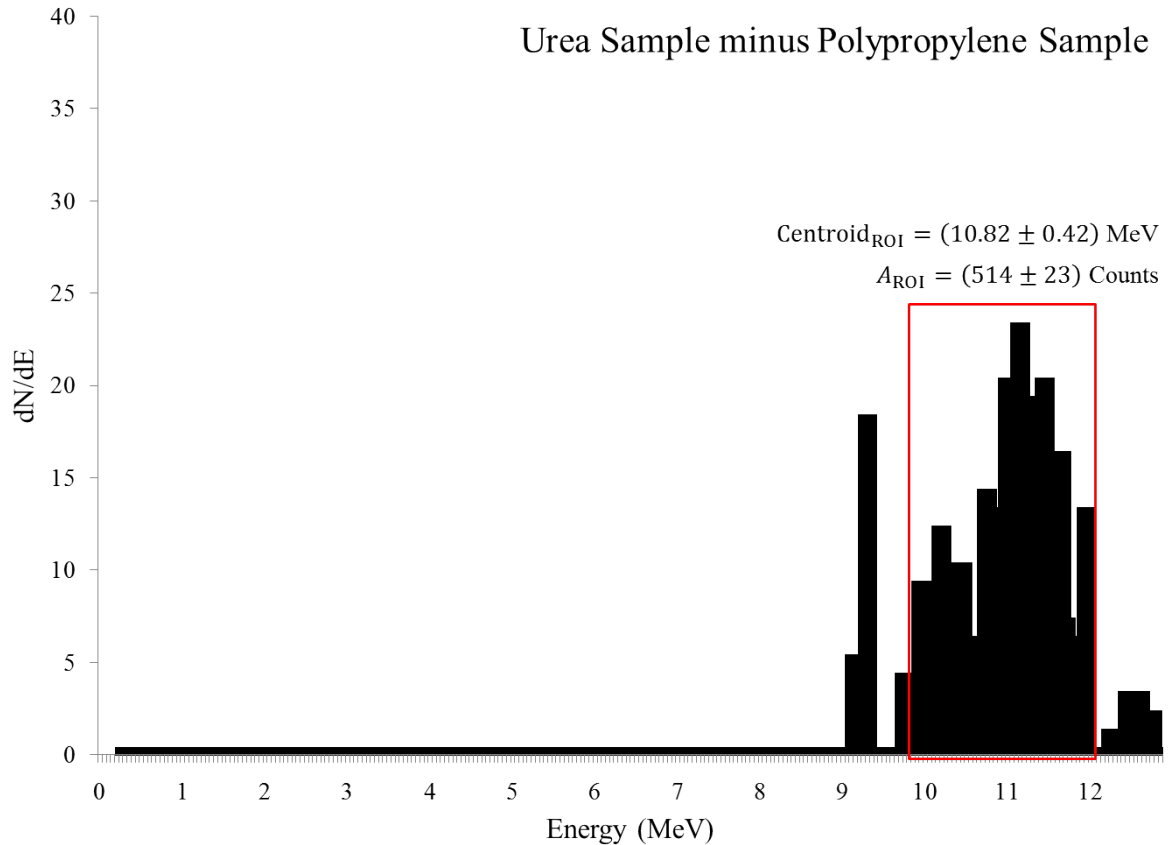


Figure 8.15: *10.8 MeV nitrogen region of interest in the urea spectrum after polypropylene spectrum subtraction*

8.7 Background Reduction

Although the previous result shows evidence of the 10.8 MeV peak in the urea sample spectrum, attempts were made to improve the signal-to-noise ratio. The following section contains details of the work undertaken.

8.7.1 Low-Energy Gamma Filter

The previous spectra were all produced with basic shielding around the NaI(Tl) detector. This was due to time constraints as many months had elapsed before the facility was ready for such an experiment. Other than a basic lead surround and a copper sheath, no further shielding was added to the setup as it was felt that if the 10.8 MeV nitrogen

peak could be detected under these conditions initially, improvements could be made at a later date during the next funding phase of the project.

Fortunately, time permitted two further experiments, undertaken in an attempt to reduce the background continuum and hence improve the peak-to-total ratio of both the hydrogen and nitrogen peaks respectively. The first experiment was to place a lead screen over the front-end window of the crystal with the thought that a few cm of lead may attenuate any low energy x-ray and gamma radiation incident on the detector front-window, induced from neutron activation of the “surroundings” as well as any natural background. The spectrum can be seen in figure 8.16.

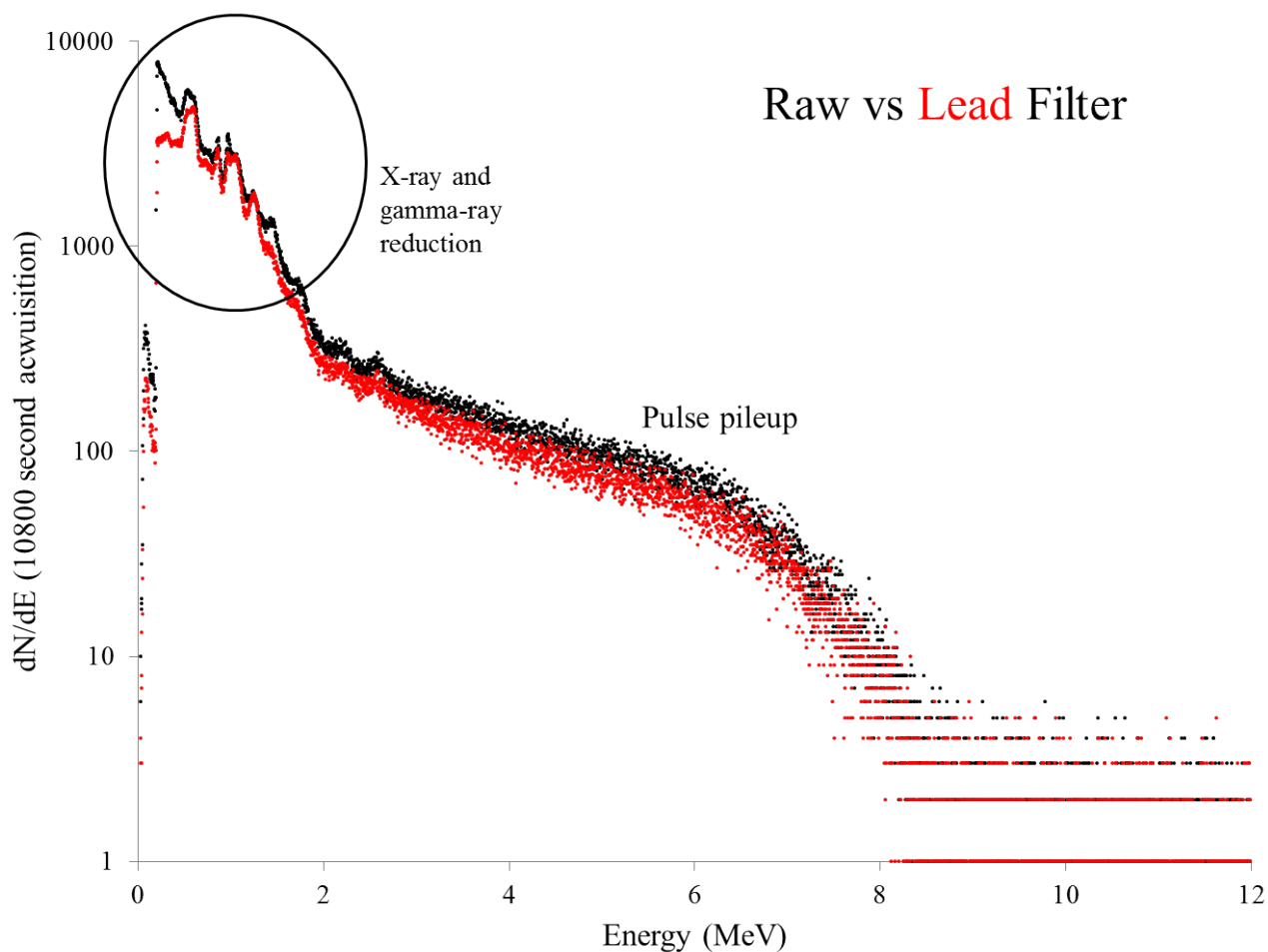


Figure 8.16: Comparison between the generator induced background with and without the lead filter over the face of the NaI(Tl) detector

The was slight reduction in the background continuum around 1 MeV and a reduction at X-ray energies under 250 keV by more than a factor of 2 as the energy decreased. This reduction was due to the lead filter screening the low energy activation of the surrounding materials and the natural background. There was also an observed (although slight) reduction in the pileup region.

In terms of the hydrogen mass ratios and nitrogen peak-to-total ratio, the results were similar to those obtained without the filter; the spectrum is shown in figure 8.17.

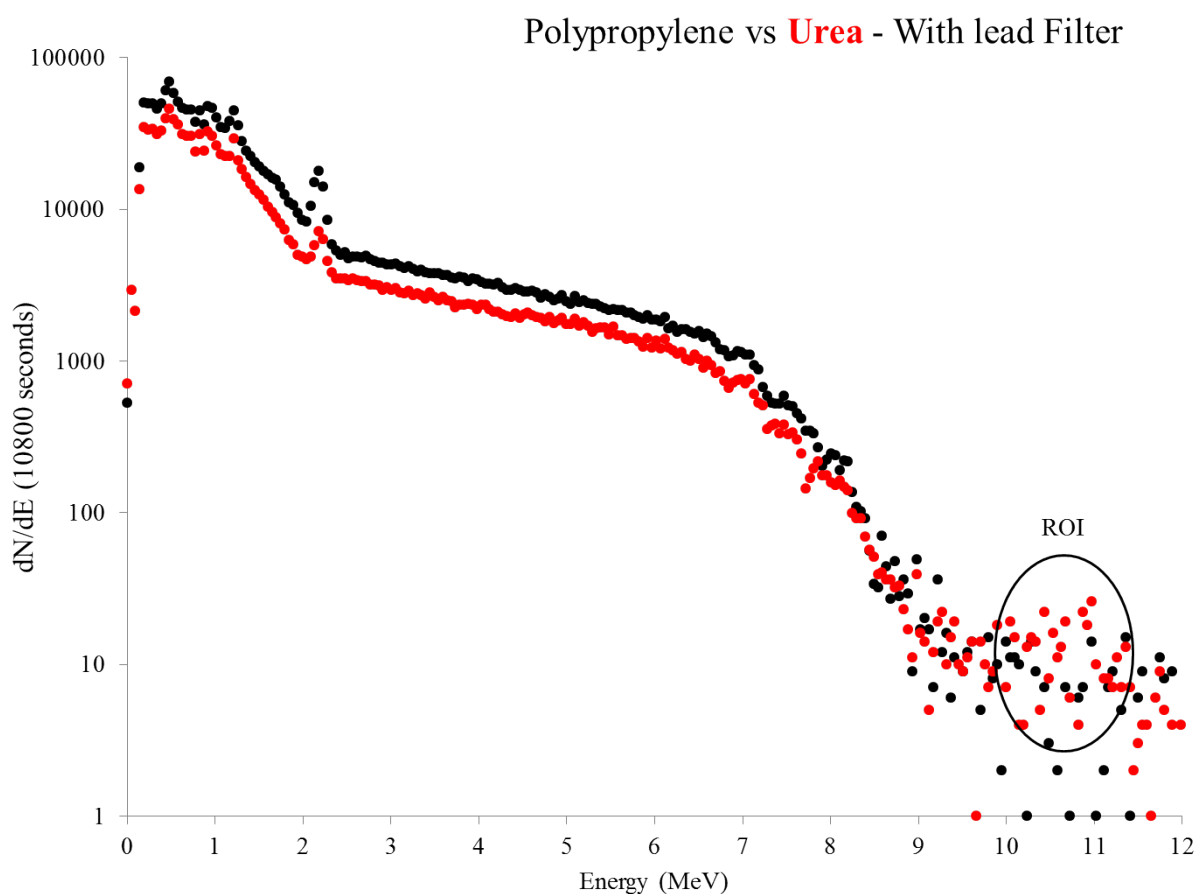


Figure 8.17: *Spectra comparison of polypropylene and urea samples with lead filter introduced*

There was however, a uniformly lower count per channel value across the MCA dynamic range from 1 MeV to 12.5 MeV. This was expected given that the magnitude of the mass attenuation coefficient did not alter between 2 MeV and 12.5 MeV and although it did

not affect the ratios it did have an effect on the associated uncertainty due to the reduced counts in the peak areas. The value of the hydrogen ratio was 0.659 ± 0.005 (1σ) and the peak-to total ratio for hydrogen is 5.1%, an increase of 12% relative to no filter. This is explained by the reduction in the low energy counts corresponding to a reduction in the total counts across the spectrum. For nitrogen, the ROI to total ratio is 0.032%, a decrease of 44%. For this reason, a filter was ruled out when nitrogen detection was the focus but would be considered for future experiments when the 2.22 MeV hydrogen line was the primary signal.

8.7.2 Addition of a Cadmium Foil

The primary source of spectral contamination was felt to be neutron events within the NaI(Tl) crystal. While time constraints meant that nothing could be done at this stage about the neutrons at source (i.e. from the bulk shield and collimator; see chapter 6, section ??) it was decided that a cadmium foil wrapped around the crystal housing would inhibit a proportion of thermal neutrons from interacting in the detector as shown in figure 8.18.



Figure 8.18: *Cadmium foil wrapped around the NaI(Tl) crystal. The geometry of the lead shield and copper collar is unaltered.*

A 1 mm thick foil which was essentially wrapped around the crystal and photomultiplier tube and positioned back inside the lead shield, was added to the detector setup. A new generator induced background spectrum, polypropylene pellet spectrum and urea spectrum were acquired for 10800 seconds and re-analysed using the Kromek KSpect software. A comparison of the generator backgrounds over the full dynamic range is shown in figure 8.19.

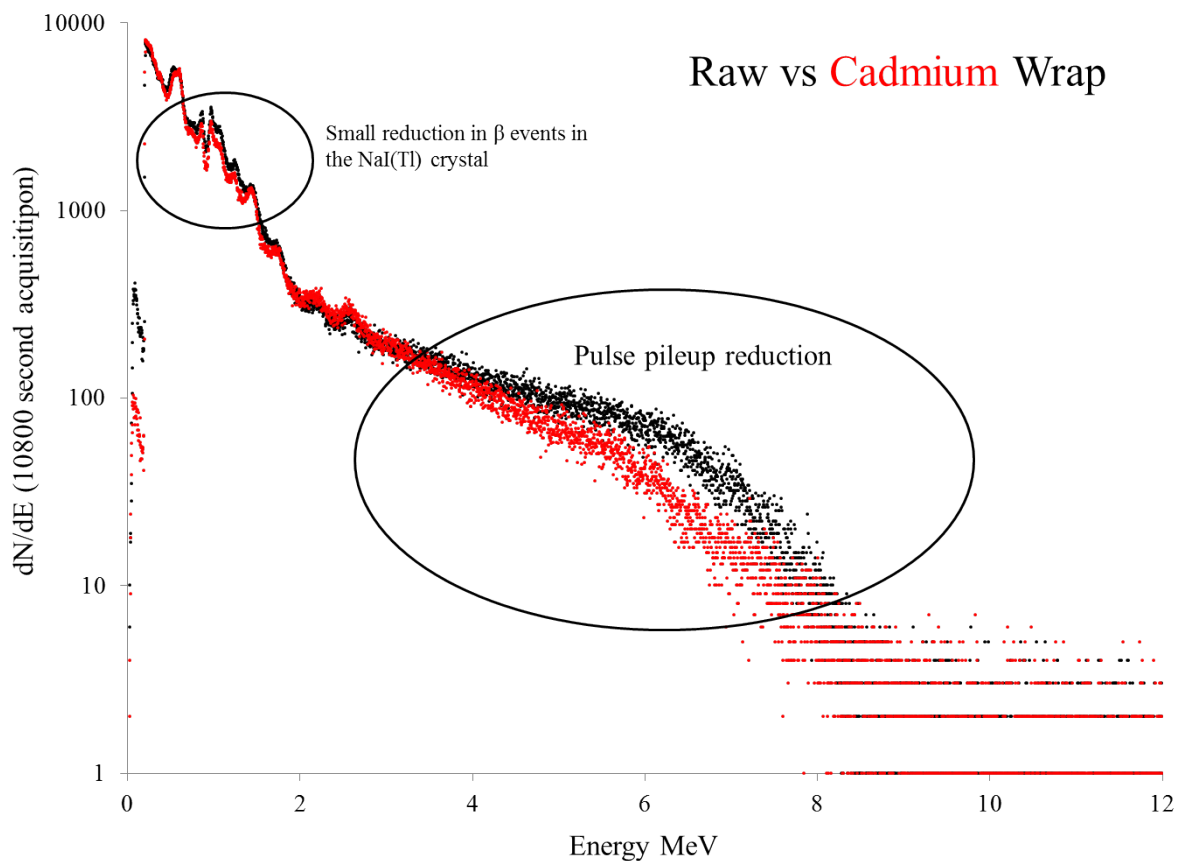


Figure 8.19: Comparison between the generator induced background with and without the cadmium foil over the NaI(Tl) detector

A significant reduction in the pile-up region is observed for both samples and background, as well as a reduction in the events originating from thermal neutron capture on the NaI(Tl) crystal, although this cannot be observed in any great detail from the re-binned spectrum over 256 channels. Figure 8.20 shows the background subtracted spectra over

256 channels for both samples and the reduction of the pileup region can be clearly seen.

Using the data, the hydrogen mass ratio from the 2.2 MeV peaks was calculated to be 0.626 ± 0.002 (1σ), which is consistent with the previous analysis, and the figure also shows a significant relative increase in the ROI region highlighted.

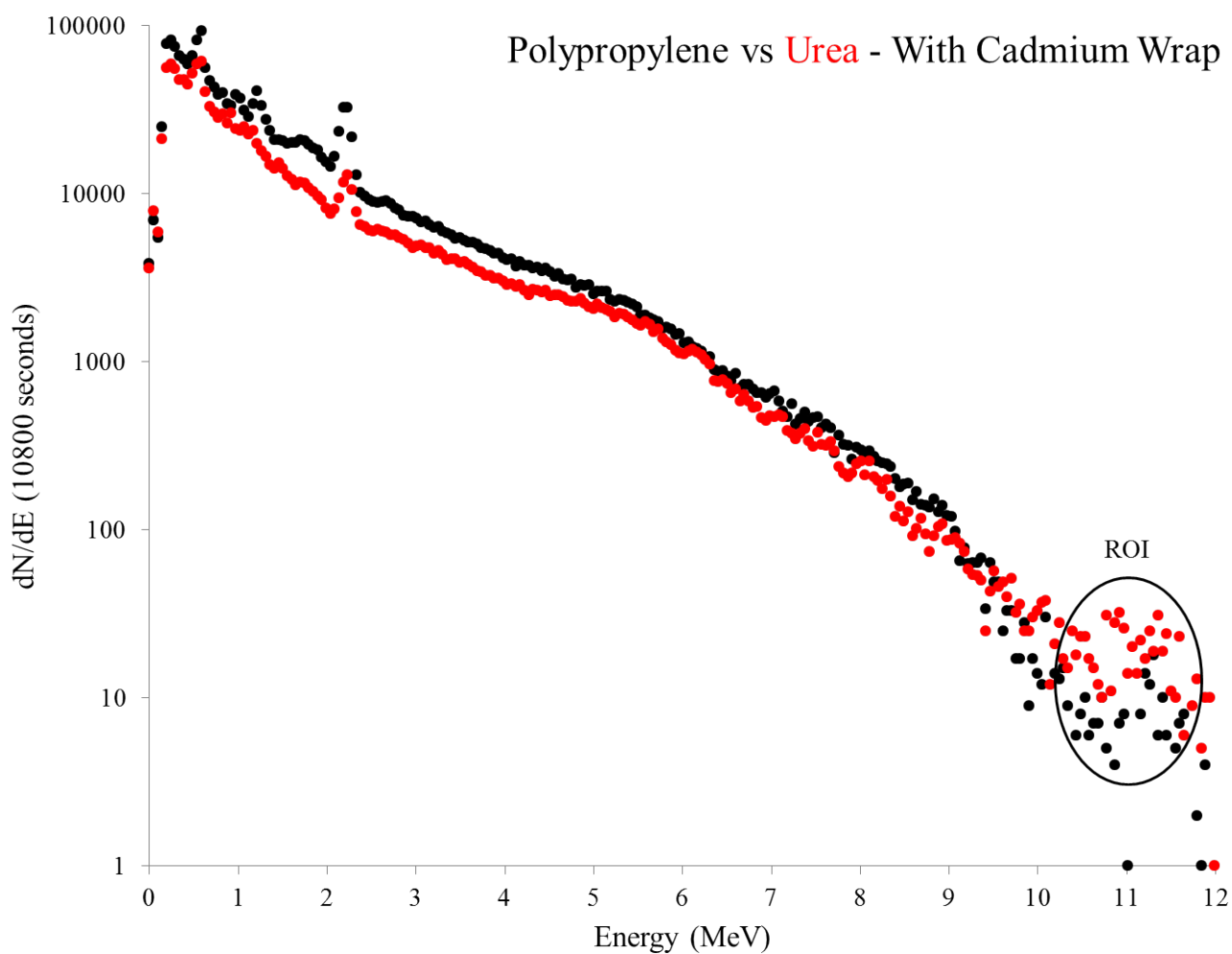


Figure 8.20: *Spectra comparison of polypropylene and urea samples with cadmium foil around the detector crystal*

This is further confirmed by the subtraction of the polypropylene from the urea spectrum as shown in figure 8.21. The ROI-to-total ratio for nitrogen detection has increased to 0.069%, an increase of 18% from the unshielded face detector.

The elevation in the number of counts in the 10.8 MeV peak was $(65 \pm 7)\%$ relative to

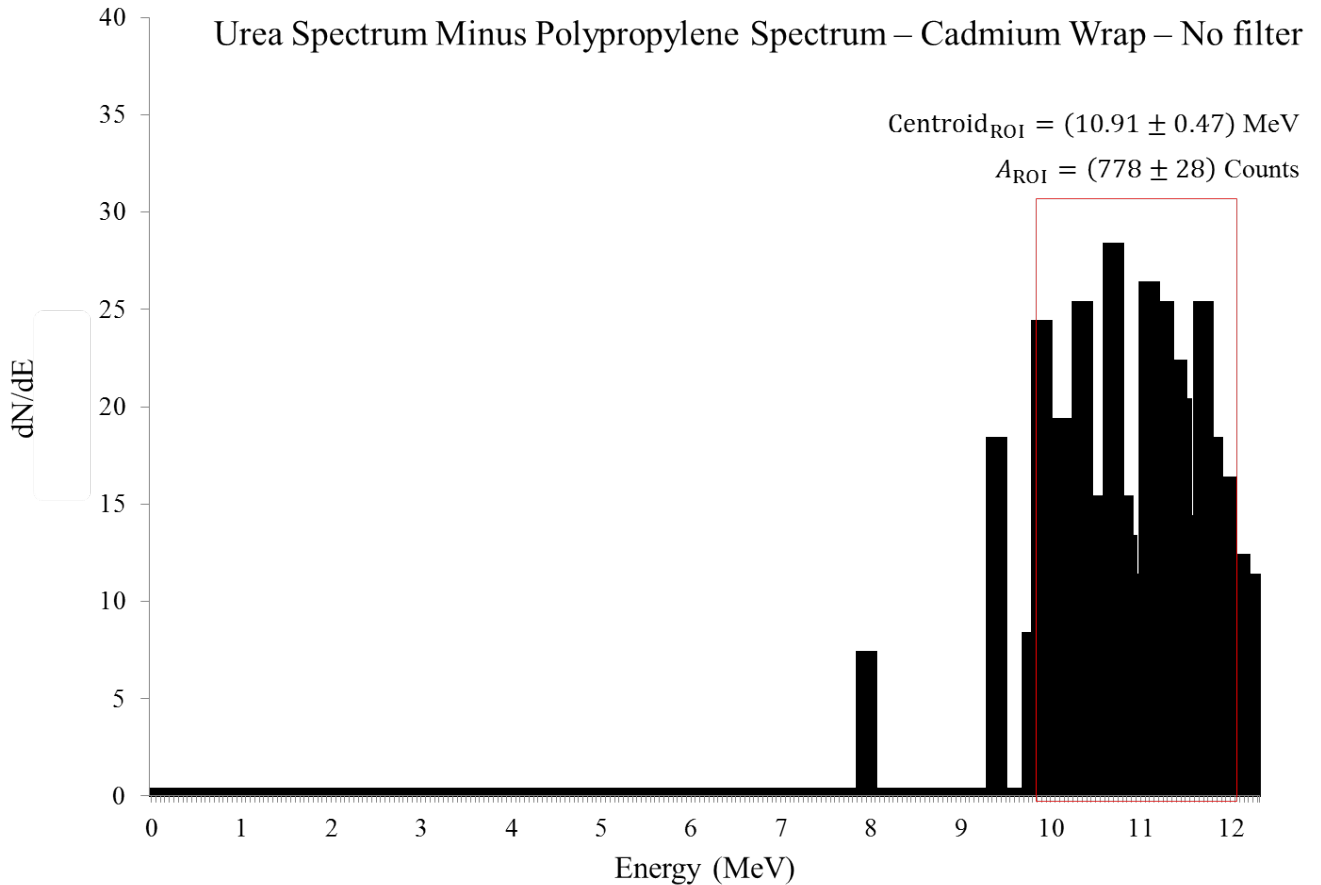


Figure 8.21: 10.8 MeV nitrogen region of interest in the urea spectrum after polypropylene spectrum subtraction

the polypropylene data. Thus, by incorporating a simple cadmium foil into the detector shield, it was possible not only to accurately calculate the hydrogen ratio, but also increase the significance of the excess once the polypropylene data has been subtracted. This is most likely due to the reduction of pulse pileup allowing more signals to be processed by the detector electronics.

8.8 Conclusions

The experiment shows that our generator system is capable of performing pulsed fast-thermal neutron activation analysis. In terms of explosives detection, the results obtained

thus far indicate that the use of PFTNAA is feasible on the basis that a simple experimental setup can be used to detect the key 10.8 MeV nitrogen gamma and the 2.2 MeV hydrogen gamma in bulk samples.

The signal processing electronics and single NaI(Tl) crystal have been configured around the detection of the above thermal neutron induced signals which have provided a positive result for activation of selected materials. The electronics configuration is adaptable to the detection of prompt inelastic scattering with a simple inversion and narrowing of the blanking pulse, and the single NaI(Tl) detector is of sufficient dimensions to detect the key carbon and oxygen lines due to the detection of 10.8 MeV gamma-rays which is the highest energy signal we will encounter.

Comparision to other work mentioned in chapter 4 [to do]

Chapter 9

Scope for Future Work at the University of Sheffield Pulsed-Neutron Facility

UNSURE WHAT WILL BE IN HERE YET AS IT RELIES ON THE DATA TAKEN FROM NOW UNTIL SUBMISSION (EITHER BEFORE THE DEADLINE OR DURING THE EXTENSION)

9.1 Prompt Signals - Inelastic Scattering

After successful determination of both hydrogen and nitrogen via thermal neutron capture reactions, explosive compounds can only be determined by combining these results with the detection of carbon and oxygen.

Everything is in place for the facility to be used to detect these other elements using the existing setup but the time constraints encountered have meant that this part of the experiment will have to be undertaken at a later date, however, the theory and steps needed to carry this work out will be explained thoroughly in Chapter 9. [I can expand

on this after we discuss what I should include in future work section]

Chapter 10

Conclusions

Chapter 11

Appendix

Because all angles of scattering are possible, the energy transferred to the electron can vary from zero (when $\theta = 0$), to a large fraction of the gamma-ray energy (when $\theta = 180^\circ$). This is shown in figure 11.1 for $\theta = 180^\circ$.

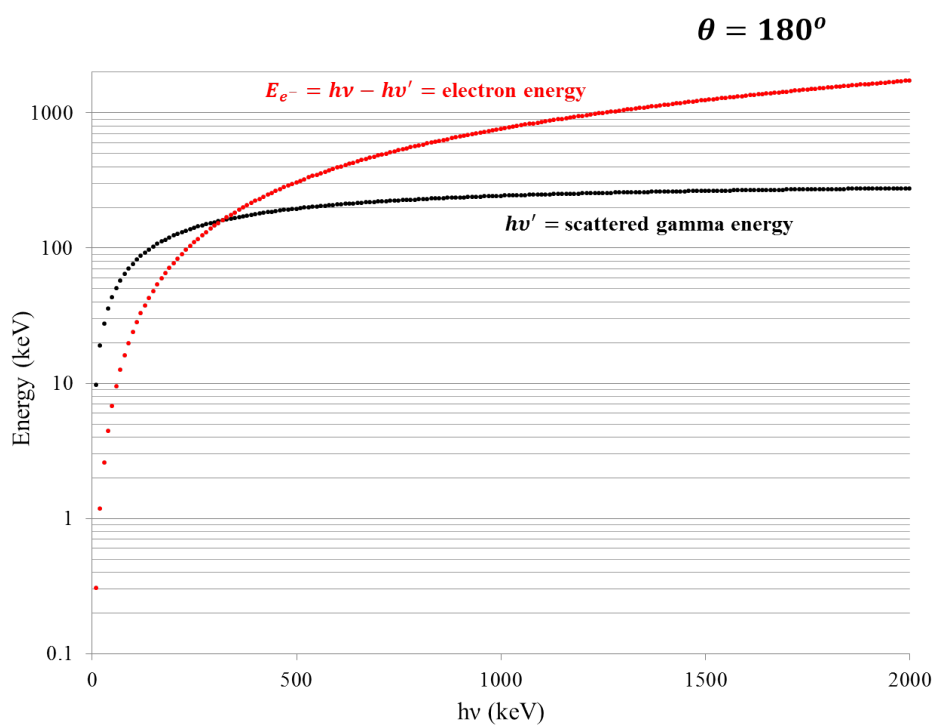


Figure 11.1: Reduction in energy of incident gamma rays and energy transfer to atomic electrons for gamma energies of 2 MeV

The black line represents the energy of the scattered gamma ray $h\nu'$ and it is clear that for gamma energies greater than around 1 MeV

11.0.1 Lateral Projection

Due to the way in which the protons lose energy in the medium there will be some deviation from a straight line. The magnitude of this deviation is known as the *lateral projection* and figure 11.2 shows this deviation as a function of incident neutron energy.

The figure shows that as the proton's range increases, the likelihood of a large angle

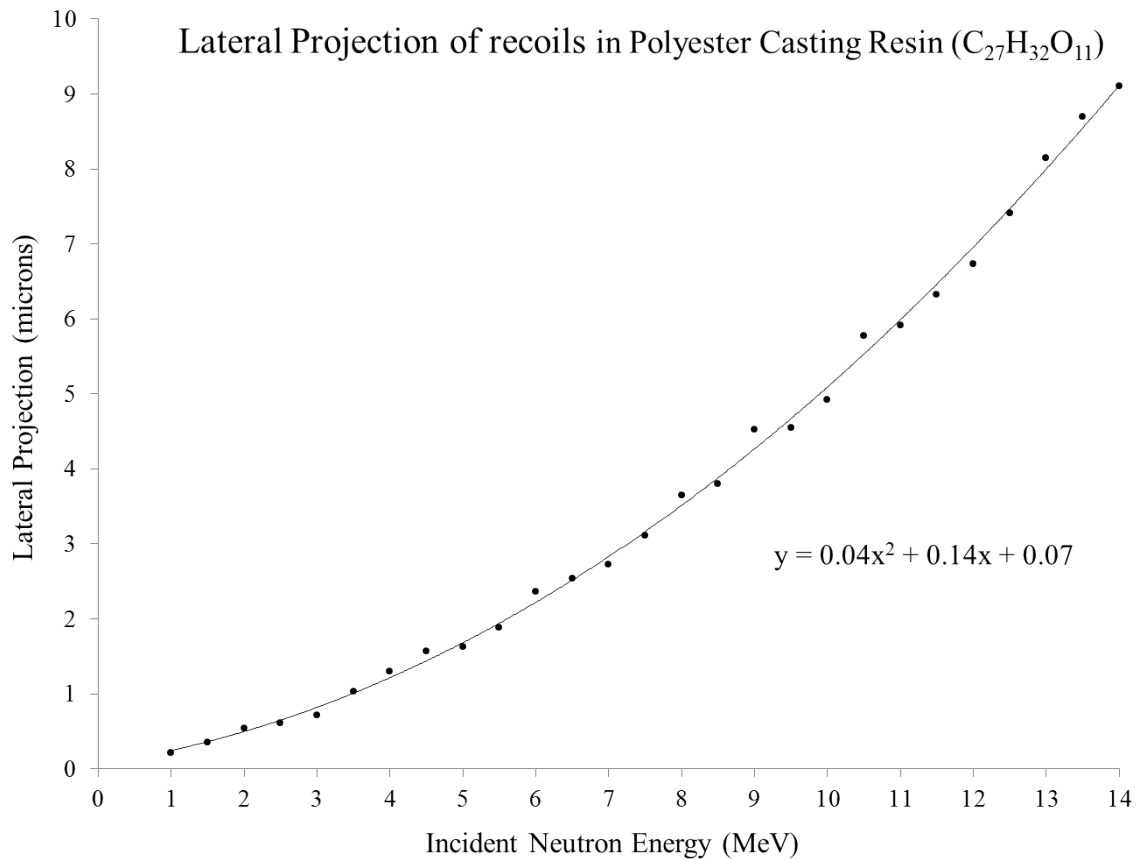


Figure 11.2: *Diagram*

scatter also increases resulting in a greater lateral projection. [The shape of the curve is almost identical to the recoil range - IS THAT RELEVANT? IS THIS OVERKILL.....?]

The first irradiation was that of liquid nitrogen (LN2). LN2 was chosen as it is a pure

source of nitrogen and would allow the performance of the system to be assessed in terms of the primary signal of interest. Once positive identification of nitrogen could be ascertained using a pure sample, it would be possible to use the spectral features when looking for similarities in more complex spectra produced by different samples for which nitrogen may, or may not, be present. A cylindrical polystyrene dewar of volume ADD THIS FIGURE cm^3 was filled with LN2 and placed at the midpoint of the aperture with the centre of the sample a distance ADD THIS FIGURE cm away from the NaI(Tl) face. No moderating material was added to the setup in order to encourage fast neutron thermalization around the sample. The flux was solely limited to the natural thermal background generated by neutron moderation from the bulk shielding and collimator. Figure ?? shows the sample in position



Figure 11.3: *IMAGE OF LN2 DEWAR NEXT TO DETECTOR OVER APERTURE*

The sample was irradiated for 2 hours (7200 s) and a spectrum acquired. The LN2 was then removed from the flask and placed back in the same location before being

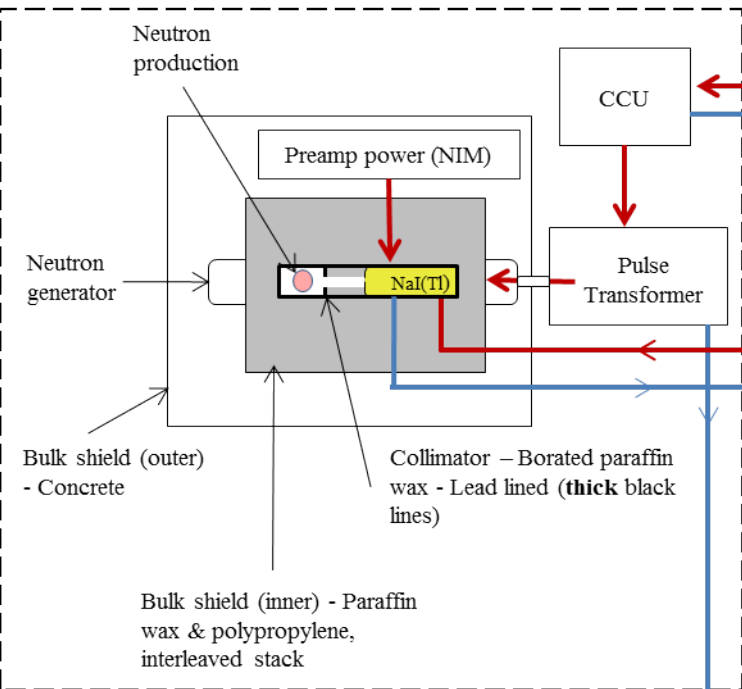
re-irradiated for a further 2 hours. Image ?? shows the two spectra



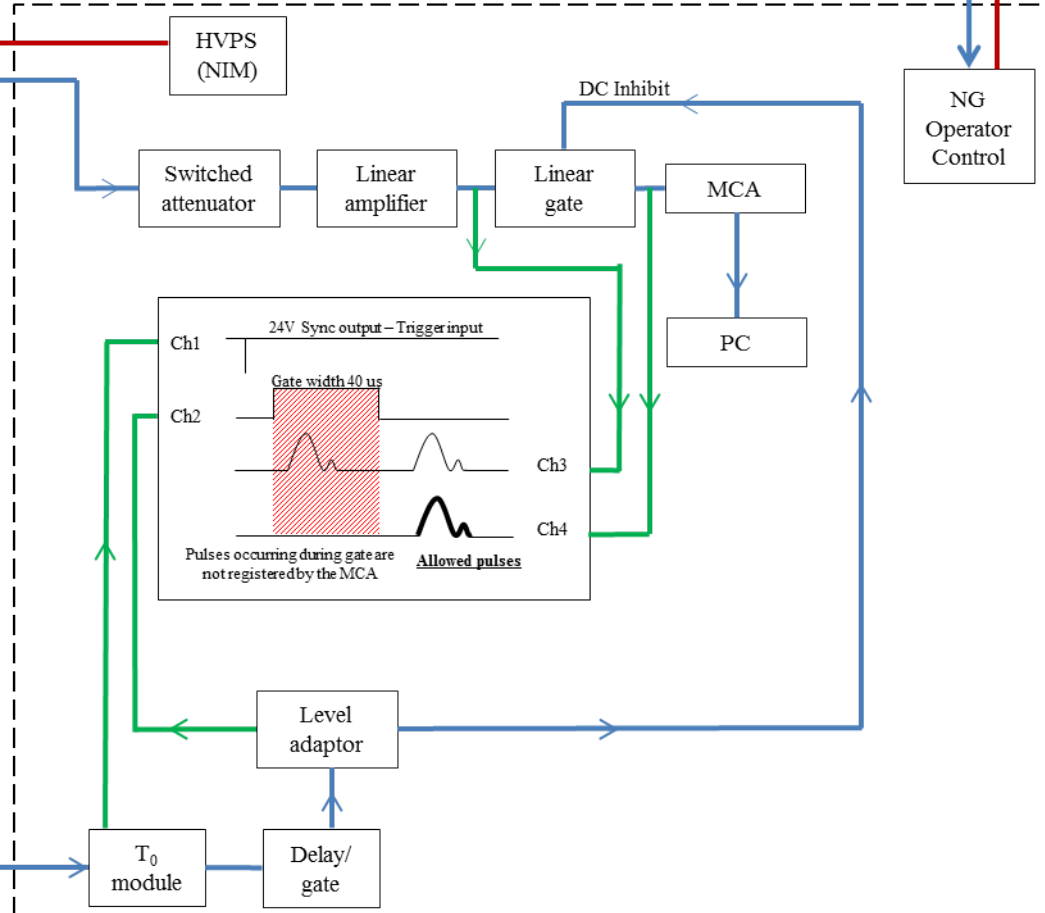
Figure 11.4: *IMAGE OF the two spectra of LN2 and NO LN2*

GENERATOR ROOM (DOWNSTAIRS)

↓ Power IN ↓ Signal OUT ↓ Monitor Signal



CONTROL ROOM (UPSTAIRS)



Words

11.0.2 Low-energy gamma filter

A simple experiment was performed in an attempt to attenuate some of the hydrogen gamma rays before entering the detector whilst allowing the higher energy nitrogen gammas through unperturbed. This was done by placing a lead screen of thickness 1 cm in front of the NaI(Tl) detector window. The mass attenuation coefficient of lead for gamma energies of 2.2 MeV and 10.8 MeV is almost identical meaning that the filter (if it did block some gamma rays) would in theory attenuate both the H and N gammas equally. The figure below shows the spectral data.

11.0.3 The $^{56}\text{Fe}(n, p)^{56}\text{Mn}$ Reaction

[TO FOLLOW AFTER IRRADIATION - HAVE INFO]

11.0.4 The $^{115}\text{In}(n, n\gamma)^{115\text{m}}\text{In}$ Reaction

[TO FOLLOW AFTER IRRADIATION - HAVE INFO]

[8]

By normalizing the data to the true mean of all data points a distribution is observed which strengthens the result that the neutron production region is less than 5 cm in length. Figure ?? shows this distribution.

Words -keep?

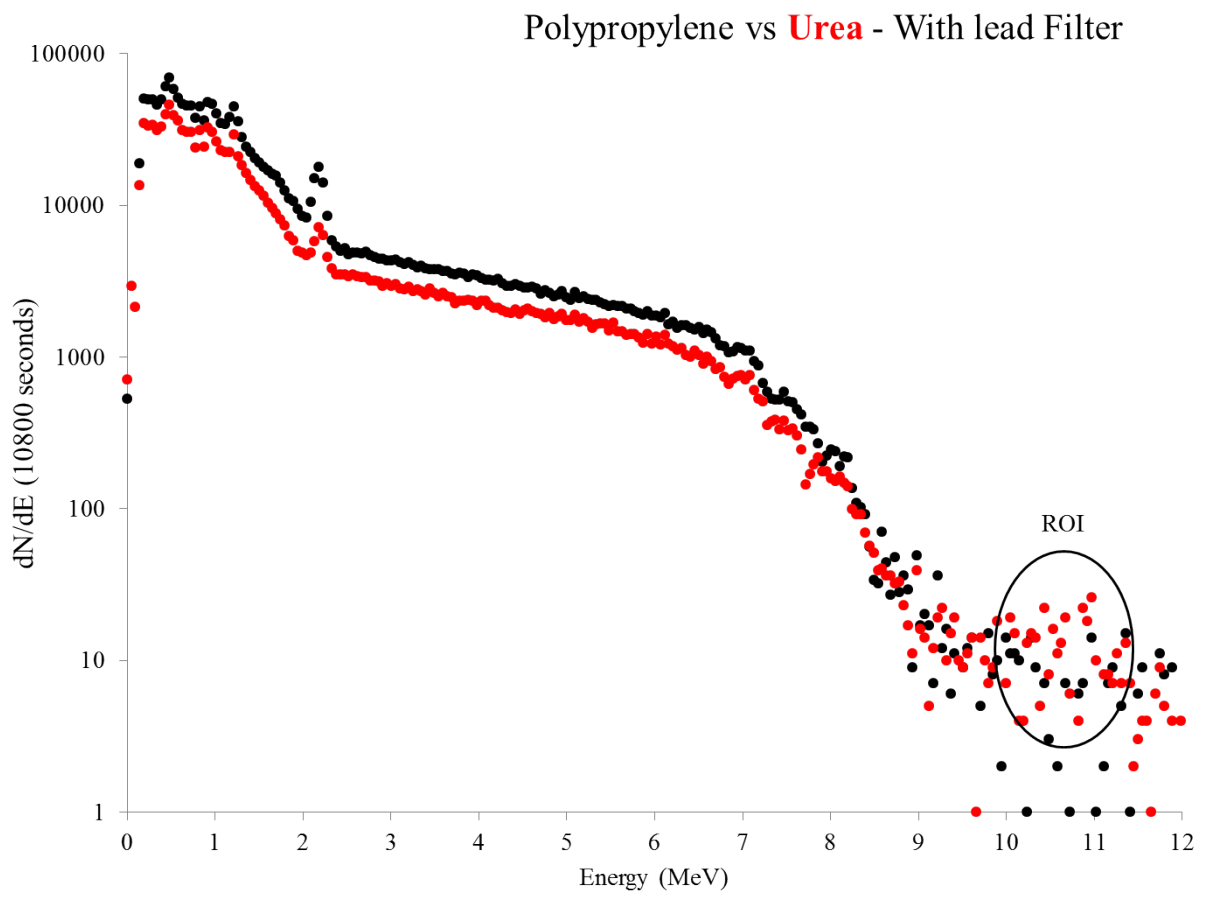


Figure 11.5: *ADD CAPTION*

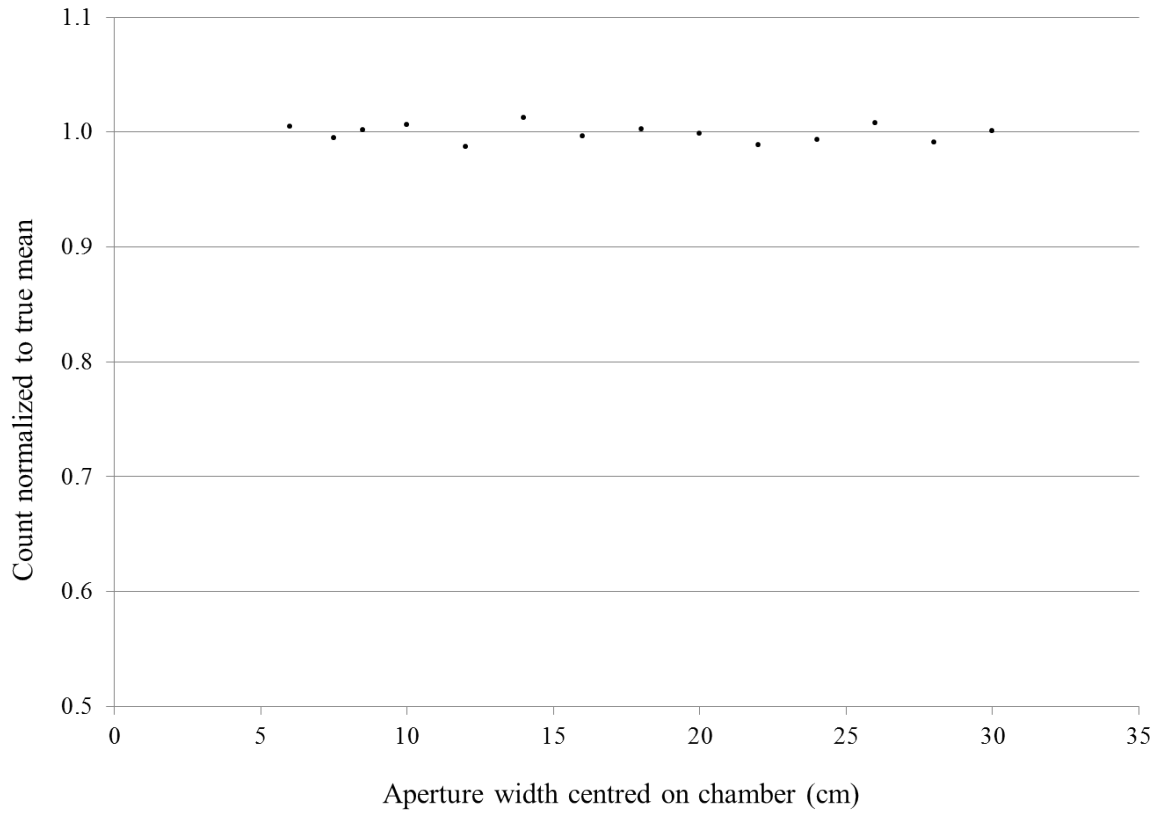


Figure 11.6: *CAPTION*

#	A	B	C	D	E	F	G	H	I	J	K	L	M	N
	Collision	Energy (eV)	Energy (J)	Velocity (m/s)	Time of flight (s)	Time of flight (μs)	Time of flight (μs)	Energy (eV)	Energy (J)	Velocity (m/s)	ToF (microsec)	Time of flight (μs)	Distance (scaled to XS)	
					(EXTREMES)	(EXTREMES)	(0.5cm)					(scaled cm)		
1	0	1400000.000	2.24E-12	51794157	2.31686E-09	0.002	0.0010	2300000	3.68E-13	20993298.05	0.006	0.0057	0.12000	
2	1	700000.000	1.12E-12	36624000	3.27654E-09	0.003	0.0014	1150000	1.84E-13	14844503.41	0.008	0.0073	0.10800	
3	2	350000.000	5.60E-13	25897079	4.63373E-09	0.005	0.0019	575000	9.2E-14	10496649.02	0.011	0.0093	0.09720	
4	3	175000.000	2.80E-13	18312000	6.55308E-09	0.007	0.0027	287500	4.6E-14	7422251.704	0.016	0.0118	0.08748	
5	4	87500.000	1.40E-13	12948539	9.26745E-09	0.009	0.0039	143750	2.3E-14	5248324.512	0.023	0.0150	0.07873	
6	5	43750.000	7.00E-14	9156000	1.31062E-08	0.013	0.0055	71875	1.15E-14	3711125.852	0.032	0.0191	0.07086	
7	6	21875.000	3.50E-14	6474270	1.85349E-08	0.019	0.0077	35937.5	5.75E-15	2624162.256	0.046	0.0243	0.06377	
8	7	10937.500	1.75E-14	4578000	2.62123E-08	0.026	0.0109	17968.75	2.875E-15	1855562.926	0.065	0.0309	0.05740	
9	8	5468.750	8.75E-15	3237135	3.70698E-08	0.037	0.0154	8984.375	1.4375E-15	1312081.128	0.091	0.0394	0.05166	
10	9	2734.375	4.38E-15	2289000	5.24246E-08	0.052	0.0218	4492.1875	7.1875E-16	927781.463	0.129	0.0501	0.04649	
11	10	1367.1875	2.19E-15	1618567	7.41396E-08	0.074	0.0309	2246.09375	3.59375E-16	656040.564	0.183	0.0638	0.04184	
12	11	683.5938	1.09E-15	1144500	1.04849E-07	0.105	0.0437	1123.046875	1.79688E-16	463890.7315	0.259	0.0812	0.03766	
13	12	341.7969	5.47E-16	809284	1.48279E-07	0.148	0.0618	561.5234375	8.98438E-17	328020.282	0.366	0.1033	0.03389	
14	13	170.8984	2.73E-16	572250	2.09699E-07	0.210	0.0874	280.7617188	4.49219E-17	231945.3658	0.517	0.1315	0.03050	
15	14	85.4492	1.37E-16	404642	2.96559E-07	0.297	0.1236	140.3808594	2.24609E-17	164010.141	0.732	0.1674	0.02745	
16	15	42.7246	6.84E-17	286125	4.19397E-07	0.419	0.1747	70.19042969	1.12305E-17	115972.6829	1.035	0.2130	0.02471	
17	16	21.3623	3.42E-17	202321	5.93117E-07	0.593	0.02471	35.09521484	5.61523E-18	82005.07049	1.463	0.2712	0.02224	
18	17	10.6812	1.71E-17	143062	8.38794E-07	0.839	0.03495	17.54760742	2.80762E-18	57986.34144	2.069	0.3451	0.02001	
19	18	5.3406	8.54E-18	101160	1.18623E-06	1.186	0.04943	8.773803711	1.40381E-18	41002.53525	2.927	0.4393	0.01801	
20	19	2.6703	4.27E-18	71531	1.67759E-06	1.678	0.06990	4.386901855	7.01904E-19	28993.17072	4.139	0.5591	0.01621	
21	20	1.3351	2.14E-18	50580	2.37247E-06	2.372	0.09885	2.193450928	3.50952E-19	20501.26762	5.853	0.7116	0.01459	
22	21	0.6676	1.07E-18	35766	3.35518E-06	3.355	0.13980	1.096725464	1.75476E-19	14496.58536	8.278	0.9057	0.01313	
23	22	0.3338	5.34E-19	25290	4.74494E-06	4.745	0.19771	0.548362732	8.7738E-20	10250.63381	11.707	1.1528	0.01182	
24	23	0.1669	2.67E-19	17883	6.71035E-06	6.710	0.27960	0.27481366	4.3869E-20	7248.29268	16.556	1.4673	0.01064	
25	24	0.834	1.34E-19	12645	9.48987E-06	9.490	0.39541	0.137090683	2.19345E-20	5125.316906	23.413	1.8676	0.00957	
26	25	0.417	6.68E-20	8941	1.34207E-05	13.421	0.55920	0.068545341	1.09673E-20	3624.14634	33.111	2.3770	0.00861	
27	26	0.209	3.34E-20	6323	1.89797E-05	18.980	0.79082	0.034272671	5.48363E-21	2562.658453	46.826	3.0255	0.00775	
28	27	0.104	1.67E-20	4471	2.68414E-05	26.841	1.11839	0.017136335	2.74181E-21	1812.07317				
29	28	0.052	8.34E-21	3161	3.79595E-05	37.959	1.58165							
30	29	0.026	4.17E-21	2235	5.36828E-05	53.683	2.23678							
31														
32														
33														
34							183	7.6			159.861	14.095		
35											us	us		
36		Distance travelled (m)	0.12											
37		Distance travelled (m)	0.005											
38		Mass of neutron (kg)	1.67E-27											
39		1 eV (J)	1.6E-19											
40														
41														
42														

$$v(\text{ms}^{-1}) = \sqrt{\frac{2E(\text{Joules})}{m(\text{kg})}}$$

Figure 11.7: *CAPTION*

Bibliography

- [1] Buffler A. Contraband detection with fast neutrons. *Radiat. Phys. Chem.*, 71:853–861, 2004.
- [2] Hussein Esam. M. A. *Handbook on Radiation Probing, Gauging, Imaging and Analysis*. Kluwer Academic Publishers, Dordrecht, Netherlands, 2004.
- [3] Bruschini C. Commercial systems for the direct detection of explosives (for explosive ordnance disposal tasks). Technical Report ExploStudy, Final Report: contract No. 155368, cole Polytechnique Fdrale de Lausanne (EPFL) & Vrije Universiteit Brussel (VUB), 2001.
- [4] Womble P. C et al. *Recent Advances in Multidisciplinary Applied Physics: Unexploded Ordnance Discrimination Using Neutrons*. Elsevier Ltd, The Boulevard, Langford Lane, Kidlington, Oxford, UK, 2005.
- [5] Evens R. D. *The Atomic Nucleus*. TATA McGraw-Hill Publishing Co. Ltd, Bombay, 1955.
- [6] Soete D et al. *Neutron Activation Analysis*. John Wiley & Sons, New York, 1972.
- [7] Sowerby B. D. et al. Recent developments in fast neutron radiography for the interrogation of air cargo containers. *IAEA Conference, Vienna*, 2009.
- [8] Donovan D. Detection of nitrogen based explosives using the uw iec device. Technical Report US-Japan Exchange, The University of Wisconsin, 2007.

- [9] Eljen Technology. EJ-410 Fast Neutron Detector Datasheet. Eljen Technology, 1300 W. Broadway, Sweetwater, Texas 79556, United States, 2006.
- [10] Elliot M. The Shoe Bomber's World. TIME Online. Retrieved August 02, 2014.
- [11] Hornyak W F. A fast neutron detector. *Rev. Sci. Instrum.*, 23:264, 1952.
- [12] Vourvopolous G. A pulsed fast-thermal neutron system for the detection of hidden explosives. *Nucl. Instrum. Meth. B*, pages 585–588, 1993.
- [13] Hemmingway J Gilmore G. *Practical Gamma-Ray Spectrometry*. John Wiley & Sons, New York, 1995.
- [14] Gozani T. A Review of NEUTRON BASED NON-INTRUSIVE INSPECTION TECHNIQUES. Ancore Corporation, Santa Clara, CA, USA.
- [15] Kaye G. W. C & Laby T. H. *Tables of Physical and Chemical Constants and Some Mathematical Functions*. Nabu Press, 2010.
- [16] Harwell Campus, Oxfordshire, United Kingdom. AEA Tvechnology Ltd. High Tech Sources - Californium-252 Spontaneous Fission Neutron Source Data Sheet.
- [17] Hirayama H. Lecture note on photon interactions and cross sections. Technical Report KEK Internal 2000-10, High Energy Accelerator Research Organization (KEK), 2000.
- [18] HORIBA Scientific. NanoLED. 2 Dalston Gardens, Stanmore, Middlesex, HA7 1BQ, United Kingdom.
- [19] Marshall M. Oxley J. *Aspects of Explosives Detection*. Elsevier, 2009.
- [20] Yinon J. *Forensic and Environmental Detection of Explosives*. John Wiley & Sons. Chichester, UK, 1999.
- [21] R.G. Jaeger et al. *Engineering Compendium on Radiation Shielding: Volume 2: Shielding Materials*. Springer Verlag, New York, 1975.

- [22] Glenn F Knoll. *Radiation Detection and Measurement: Third Edition*. John Wiley & Sons, Inc, Oxford, 1999.
- [23] Molnar Gabor. L. *Handbook of Prompt Gamma Activation Analysis (with Neutron Beams)*. Kluwer Academic Publishers, P.O. Box 17, 3300 AA Dordrecht, The Netherlands, 2004.
- [24] Larry Greenemeier. Exposing the Weakest Link: As Airline Passenger Security Tightens, Bombers Target Cargo Holds. *Scientific American*, November 2 2010. Retrieved August 12, 2014.
- [25] Leppard D. Terrorists Package a new Punch. *The Australian*. Retrieved September 13, 2014.
- [26] Mazzetti M, Worth Robert. F. U.S. Sees Complexity of Bombs as Link to Al Qaeda. *The New York Times*, October 30 2010. Retrieved August 12, 2014.
- [27] Megahid R. M and others. Neutron based techniques for detection of illicit materials and explosives. Technical Report Research contract 13497, Laboratories for Detection of Landmines and Illicit Materials, Nuclear Research Centre, Atomic Energy Authority, Cairo, Egypt, 2008.
- [28] Ahmed S. N. *Physics and Engineering of Radiation Detectors*. Elsevier, 2007.
- [29] Didenko A. N. et al. Generation of nanosecond neutron pulses in vacuum accelerating tubes. *Technical Physics*, 59:904–910, 2014.
- [30] National Institute of Standards and Technology (NIST), 100 Bureau Dr, Gaithersburg, MD 20899, United States. Physics Reference Data - Xray Mass Coefficients - Element Z=82. Website - United States Department of Commerce - NIST.
- [31] Nave. C. R. *The Neutron*. Department of Physics and Astronomy, Georgia State University, United States.

- [32] ORGANISATION FOR THE PROHIBITION OF CHEMICAL WEAPONS. About ChemicalWweapons. Johan de Wittlaan 32 2517 JR - The Hague The Netherlands.
- [33] Pezzullo John C. Nonlinear Least Squares Regression (Curve Fitter). Available: <http://statpages.org/nonlin.html>. Last accessed 31st July 2014.
- [34] Leo W. R. *Techniques For Nuclear And Particle Physics Experiments*. Springer-Verlag, Berlin Heidelberg, 1987.
- [35] Speller R. Radiation-based security. *Radiat. Phys. Chem.*, 61:293–300, 2001.
- [36] Ragheb M. Nuclear power engineering, part vii, lecture 3 (neutron cross sections), semester 1. Technical Report NPRE402, University of Illinois at Urbana-Champaign, 2014.
- [37] Ragheb M. Nuclear power engineering, part vii, lecture 6 (neutron diffusion in nonmultiplying media), semester 1. Technical Report NPRE402, University of Illinois at Urbana-Champaign, 2014.
- [38] Rinard P. Neutron Interactions with Matter. Website - Federation of American Scientists (FAS) Publications.
- [39] Anderson Ian. S. *Neutron Imaging and Applications (A Reference Guide for the Imaging Community)*. Springer Science + Business Media, 2009.
- [40] Krane K. S. *Introductory Nuclear Physics*. John Wiley & Sons, New York, 1998.
- [41] Stergiopoulos S. *Advanced Signal Processing Handbook: Theory and Implementation for Radar, Sonar, and Medical Imaging Real-Time Systems*. CRC Press LLC, Florida 33431, United States, 2001.
- [42] Singh Maneesha Singh Sameer. Explosives detection systems (eds) for aviation security. *Signal Process*, 83:31–55, 2002.
- [43] The United States Nuclear Regulatory Commission and Duke University. Regulatory and Radiation Protection Issues in Radionuclide Therapy: Interactions of Neutrons

with Matter. Website - Duke University Occupational & Environmental Safety Office; Radiation safety Division.

- [44] Pujala U. Analysis of neutron streaming through the trenches at linac based neutron generator facility, igcar. *Radiation Protection & Environment (India)*, 34:262–266, 2011.
- [45] United Nations Office on Drugs and Crime. Drug Trafficking. Vienna International Centre , Wagramer Strasse 5 A 1400 Vienna, Austria.
- [46] U.S. Department of Homeland Security. Introduction to Explosives. Technical Resource for Incident Prevention (TRIPwire). Retrieved July 7, 2014 .
- [47] U.S. Federal Government. Improvised munitions handbook (improvised explosive devices or ieds). Technical Report TM 31-210, Headquarters, Department of the Army, 1969.